Master's thesis

NTNU
Norwegian University of Science and Technology
Faculty of Natural Sciences
Department of Physics

Rasmus Hoholm

Electronic and Optical Properties of TiO2, and the Potential of Doped TiO2 for the Use in Intermediate Band Solar Cells

A DFT Study

Master's thesis in Nanotechnology (MTNANO)
Supervisor: Jon Andreas Støvneng
Co-supervisor: Turid Reenaas
August 2023

NTNU
Norwegian University of
Science and Technology

Rasmus Hoholm

Electronic and Optical Properties of TiO2, and the Potential of Doped TiO2 for the Use in Intermediate Band Solar Cells

A DFT Study

Master's thesis in Nanotechnology (MTNANO)
Supervisor: Jon Andreas Støvneng
Co-supervisor: Turid Reenaas
August 2023

Norwegian University of Science and Technology
Faculty of Natural Sciences
Department of Physics

NTNU
Norwegian University of
Science and Technology

Abstract

Titanium dioxide (TiO_2), with its distinctive properties and cost-effective, non-toxic, and stable nature, is widely utilized in various sectors including advanced energy technologies like photovoltaic devices. One such example is the recently emerged interest in doped TiO_2 as a potential intermediate band material for intermediate band solar cells (IBSCs). This thesis explores the electronic and optical properties of rutile and anatase, two polymorphs of TiO_2, using various methods such as generalized gradient approximation (GGA) based density functional theory (DFT), an adapted version of the PHS method for improved optical predictions, and DFT+U. Lastly, doped configurations of TiO_2 are investigated to evaluate their potential use in IBSCs. Our standard DFT calculations revealed a vast band gap underestimation, highlighting the need for refined methods and the potential utility of the hybrid Heyd–Scuseria–Ernzerhof (HSE06) functional. The optical data, produced by our semi-empirical modification of the PHS method, largely corroborated existing literature. However, certain discrepancies, particularly on a detailed level, underscored the need for methodological enhancement. Our imaginary dielectric functions exhibited a greater number of critical points (CPs) than have previously been reported in experimental research. In an attempt to address a gap in the literature, an effort was made to connect the critical points to interband transitions. We identified regions in the band structure with significant numbers of possible optical transitions, and made comparisons with the CP energies. Our analysis identified likely contributing transitions to a majority of the CPs, but lacked optical matrix elements as well as comparative literature to verify our findings. Our explorations into doped TiO_2 yielded promising results. Two configurations, rutile doped with 25% and 12.5% CrN, formed an intermediate band between the valence and conduction bands. Although the band gap prediction limitations inherent in GGA-based calculations introduced uncertainties into our results for doped TiO_2, the discovery of these intermediate bands paves an exciting route for future research.

Sammendrag

Titandioksid (TiO_2), med sine særegne egenskaper og kostnadseffektive, ikke-giftige, og stabile natur, er mye brukt i ulike sektorer, inkludert avanserte energiteknologier som fotovoltaiske enheter. Et eksempel på sistnevnte er den nyoppståtte interessen for dopet TiO_2 som et potensielt mellombåndmateriale for mellombåndsolceller. Denne oppgaven utforsker de elektroniske og optiske egenskapene til rutil og anatase, to polymorfer av TiO_2, ved hjelp av ulike metoder som generalized gradient approximation (GGA) basert density functional theory (DFT), en tilpasset versjon av PHS-metoden for forbedrede optiske prediksjoner, og DFT+U. Våre standard DFT-beregninger avdekket en stor underestimering av båndgapet, noe som fremhever behovet for forbedrede metoder og den potensielle nytten av den hybride Heyd–Scuseria–Ernzerhof (HSE06)-funksjonalen. De optiske dataene, produsert av vår semi-empiriske modifikasjon av PHS-metoden, bekreftet i stor grad eksisterende litteratur. Imidlertid understreket visse avvik, spesielt på et detaljert nivå, behovet for metodologisk forbedring. Våre imaginære dielektriske funksjoner viste et større antall kritiske punkter enn hva som tidligere har blitt rapportert i eksperimentell forskning. Med hensikt om å adressere en mangel i litteraturen, ble det gjort et forsøk på å koble de kritiske punktene til overganger i båndstrukturen. Vi identifiserte områder i båndstrukturen med et betydelig antall mulige optiske overganger, og gjorde sammenligninger med energiene til de kritiske punktene. Vår analyse identifiserte sannsynlige bidragende overganger til flertallet av de kritiske punktene, men manglet optiske matriseelementer i tillegg til sammenlignende litteratur for å bekrefte våre funn. Våre undersøkelser av dopet TiO_2 ga lovende resultater. To konfigurasjoner, rutil dopet med 25% og 12.5% CrN, dannet et mellombånd mellom valensbåndet og ledningsbåndet. Selv om svakhetene i båndgapsprediksjon iboende i GGA-baserte beregninger introduserte usikkerheter i resultatene våre for dopet TiO_2, baner oppdagelsen av disse mellombåndene vei for spennende ruter for fremtidig forskning.

Preface

This thesis was written during my final semester at the 5-year master's program in Nanotechnology at the Norwegian University of Science and Technology (NTNU). I would like to especially thank my supervisor, Assoc. Prof. Jon Andreas Støvneng, whose support and insightful guidance have been invaluable throughout the course of this project. In addition, I thank my co-supervisor Prof. Turid Reenaas, along with Prof. Morten Kildemo and Thomas Vågenes Brakstad, for their academic insights into the matters of materials and optics. Lastly, I am grateful for the developers of Talon, an open-source speech-to-text program. Talon proved vital for the thesis' completion during a long-lasting bout of tendinitis that rendered keyboards a fierce adversary.

Contents

Acronyms

BZ Brillouin zone. 13, 15, 22, 23, 52, 54

CB conduction band. 19, 22, 23, 25, 26, 30, 37, 40, 56, 60, 61, 64, 68

CP critical point. iii, 22, 23, 29–31, 41, 46–54, 77, 78

DFT density functional theory. iii, iv, 1–4, 7, 9, 17, 18, 23, 27, 29, 31, 32, 34, 37, 45, 50, 58, 75, 77, 78

DOS density of states. 20, 28, 32, 36, 37, 39, 40, 45, 54–56, 58, 61–64, 67–72, 75, 76

GGA generalized gradient approximation. iii, iv, 1, 10, 11, 23, 29, 35, 37, 45, 50, 75, 77, 78

HF Hartree–Fock. 6, 9

HSE06 Heyd–Scuseria–Ernzerhof. iii, iv, 11, 29, 34, 35, 46, 75, 77, 78

IB intermediate band. 25, 26, 60, 61, 64, 68, 69

IBSC intermediate band solar cell. iii, 1, 24, 25, 32, 60, 61, 77, 78

LDA local density approximation. 1, 10, 11, 29, 34, 35, 37

NC norm-conserving. 17, 28, 29, 34–44, 47, 48, 57, 59, 62, 63, 65–67, 70–74, 76

NSCF non-self-consistent field. 28, 32, 50

PAW projector augmented-wave. 17, 29, 31, 32, 34, 35, 55, 57, 58

PBE Perdew–Burke–Ernzerhof. 10, 11, 23, 28, 29, 34–44, 47, 48, 57, 62, 63, 65–67, 70–74, 76

PBEsol Perdew–Burke–Ernzerhof for solids. 11, 29, 31, 32, 34–36, 55–59

PHS PBE+HSE06+Sum rule. iii, iv, vii, 1, 23, 29, 40–48, 77

PP pseudopotential. 28, 29, 34–37

PZ Perdew–Zunger. 29, 34, 35

QE Quantum ESPRESSO. 27, 28

SCF self-consistent field. 6, 9, 27, 28, 32

SQ Shockley–Queisser. 24

VB valence band. 19, 22, 23, 25, 26, 30, 37, 40, 56, 60, 61, 64, 68

XC exchange-correlation functional. 28, 29, 34–37

Chapter 1

Introduction

Titanium dioxide (TiO_2) stands as a material of prime importance across a variety of commercial and industrial applications, thanks to its unique properties, such as its wide band gap, high refractive index, and impressive photocatalytic behavior [1, p. 6]. Moreover, the extraordinary stability, non-toxicity, and cost-effectiveness of TiO_2 have marked it as a desired component in diverse sectors, from traditional applications such as paints, sunscreens, and catalysts to the forefront of cutting-edge technologies.

The advent of TiO_2 in the field of advanced energy technologies, notably in photovoltaic devices, has garnered considerable attention. The recent surge of interest in doped TiO_2 as a potential material for intermediate band solar cells (IBSC) offers exciting possibilities [2–5]. IBSCs possess theoretical efficiencies that surpass the limitations of traditional single-junction solar cells by introducing a band of electronic states within the band gap. This paper focuses on exploring the doping of TiO_2 as a promising avenue for creating such an intermediate band. The study presents a meticulous investigation of several doped configurations of the two most common TiO2 polymorphs - rutile and anatase, employing chromium (Cr) and nitrogen (N) co-doping or molybdenum (Mo), chosen due to their abundance, environmental friendliness, and human tolerance [6, 7].

Before we explore these modified structures, an in-depth analysis of the pure forms of rutile and anatase was conducted. This study deployed a variety of density functional theory (DFT) approaches, such as the standard generalized gradient approximation and local density approximation based calculations. Given the constraints of conventional DFT computations, such as the significant underestimation of the band gap – a deficiency apparent in TiO_2 [1, p. 68] – we also sought out alternative strategies. These included the use of a hybrid exchange-correlation functional, the DFT+U method, and the recently proposed PHS method, designed for more accurate optical calculations [8].

In our endeavor to comprehensively understand the properties of TiO_2, we identified a notable gap in the existing literature pertaining to critical point analyses. More specifically, studies identifying the interband transitions in k-space, which are responsible for critical points of the imaginary dielectric function. These interband transitions carry significant weight as they directly influence the material's optical and electronic properties, consequently impacting its efficiency and application potential in various fields [9, 10, p. 267]. To address this, we undertook an analysis of the possible optical transitions within the band structure and compared the results with critical point energies. Our objective in doing so is to unearth deeper insights that could pave the way for more effective optimization of TiO2 in advanced technological applications.

In Chapter 2, the principles of density functional theory are discussed, as well as the physical concepts integral to this research. Subsequently, in Chapter 3, we provide an in-depth description of the computational techniques utilized in our study. Chapter 4 presents and discusses our findings, before a conclusion in Chapter 5.

Chapter 2

Density Functional Theory & Solid State Physics

Note: Chapter 2, with the exception of Sects. 2.12, 2.17, 2.18, 2.19, and parts of 2.5 and 2.16, are adapted from the author's project thesis, titled "Electronic and Optical Properties of TiO_2" (2022).

The quantum mechanical study of molecules and materials often involves multiple atoms that make up a many-body problem. To calculate the properties of these systems one must therefore solve the many-body Schrödinger equation, to which finding an exact solution is virtually impossible. Numerous approximate methods have been developed over the years, that balance the numerical accuracy with the computational cost, but few have been more successful than density functional theory (DFT).

The foundations of DFT were laid by Hohenberg, Kohn, and Sham in the mid-1960s, when they discovered an alternate way of solving the Schrödinger equation. The popularity of the method exploded in the 1990s, when approximation improvements led to significantly higher accuracy of results [11]. These days, DFT is widely used in a number of fields, including physics, chemistry, materials science, chemical engineering, and geology. In this chapter, we will lay out the main principles behind DFT and discuss the theory behind properties computed in this project. Unless otherwise stated, the contents of this chapter are based on chapters 1, 3, and 8 of [12].

2.1 The Many-Body Schrödinger Equation

The goal of DFT is often to find the ground state energy of a given system, meaning its lowest energy configuration, a property that is independent

of time. Thus, it is the time-independent Schrödinger equation that is of relevance, which in its simplest form, discounting relativistic effects, reads

$$\hat{H}\psi = E\psi. \tag{2.1}$$

This is an eigenvalue equation, where $\hat{H}$ is the energy operator, called the Hamiltonian, ψ is the set of eigenstates of $\hat{H}$, and E is a set of eigenvalues associated with each solution ψ.

In a many-body problem, the Hamiltonian must describe the interaction of many nuclei with even more electrons. A common simplification to the problem is the *Born–Oppenheimer approximation*, where the wave functions of the nuclei and the electrons are treated separately [13]. This is made possible by the electron mass being several orders of magnitude smaller than the nuclei mass, while experiencing similar forces. As a result, one can then first solve for the electrons, with the nuclei positions fixed. In such a system, the equation takes the form

$$\left[-\frac{\hbar^2}{2m}\sum_{i=1}^{N}\nabla_i^2 + \sum_{i=1}^{N}V(\mathbf{r}_i) + \sum_{i=1}^{N}\sum_{j<i}U(\mathbf{r}_i,\mathbf{r}_j)\right]\psi = E\psi, \tag{2.2}$$

where m is the electron mass, N is the number of electrons, and ψ is the many-body wave function for the N electrons. ∇^2 is the Laplacian operator and relates to the kinetic energy term for each electron. $V(\mathbf{r}_i)$ is the interaction energy between electron i and the set of nuclei and $U(\mathbf{r}_i,\mathbf{r}_j)$ describes the interaction energy between electron i and j.

2.2 The Hartree and Hartree–Fock Methods

2.2.1 The Hartree Method

In the 1920s, a computational method for solving the many-body Schrödinger equation was developed, called the Hartree method. This method is somewhat of a precursor to DFT and is therefore useful to understand before moving forward. If one assumes that the electrons in the system have no interaction effects, then the total Hamiltonian can be expressed as a sum of the individual energy operators of the system's N electrons,

$$\hat{H} = \sum_{i=1}^{N}\hat{h}_i. \tag{2.3}$$

The corresponding Schrödinger equation for a single electron would then be

$$\hat{h}\chi = E\chi, \tag{2.4}$$

where each χ is a spin orbital, to which there are multiple per single-electron equation. The j-th spin orbital will be denoted $\chi_j(\mathbf{x}_i)$, where $\mathbf{x}_i$ defines the position and spin state of electron i. As a consequence of Eq. (2.3), the eigenfunctions of $\hat{H}$ can be expressed as products of the single-electron spin orbitals, called the Hartree product,

$$\psi(\mathbf{x}_1, ..., \mathbf{x}_N) = \chi_1(\mathbf{x}_1)\chi_2(\mathbf{x}_2)\cdots\chi_N(\mathbf{x}_N) = \prod_{i=1}^{N}\chi_i(\mathbf{x}_i). \tag{2.5}$$

The Hartree method uses a fixed nuclei approach and attempts to calculate the wave function of an N-electron system. The Schrödinger equation for a single electron is then

$$\left[-\frac{\hbar^2}{2m}\nabla^2 + V(\mathbf{r}) + V_{\mathrm{H}}(\mathbf{r})\right]\chi_j(\mathbf{x}) = E_j\chi_j(\mathbf{x}). \tag{2.6}$$

Here, $V_{\mathrm{H}}(\mathbf{r})$ is the Hartree potential, which describes the Coulomb repulsion from other electrons as an average and not as a potential between each pair of charges,

$$V_{\mathrm{H}}(\mathbf{r}) = e^2\int\frac{n(\mathbf{r}')}{|\mathbf{r}-\mathbf{r}'|}d^3r'. \tag{2.7}$$

The electron density $n(\mathbf{r})$ is expressed as

$$n(\mathbf{r}) = 2\sum_{i=1}^{N}\psi_i^*(\mathbf{r})\psi_i(\mathbf{r}), \tag{2.8}$$

where the factor 2 accounts for the spin degeneracy of the orbitals.

As the Hartree method is computational, the continuous wave function must be represented by a linear combination of a finite set of functions called the basis set, $\phi_1(\mathbf{x}), \phi_2(\mathbf{x}), \ldots, \phi_K(\mathbf{x})$. The approximate single-electron wave function may then be expressed as

$$\chi_j(\mathbf{x}) = \sum_{i=1}^{K}\alpha_{j,i}\phi_i(\mathbf{x}). \tag{2.9}$$

Thus, one merely has to find the expansion coefficient $\alpha_{j,i}$ for all j and i to determine the spin orbitals. Using a larger basis set will increase the accuracy of the wave functions, but also increases the computational cost. Therefore, one has to strike a balance between these two considerations when performing the calculations.

We now have the fundamentals to solve the many-body Schrödinger equation in iterations. One must first create an ansatz for the spin orbitals χ_j by choosing expansion coefficients $\alpha_{j,i}$, and then calculate the electron density $n(\mathbf{r}')$. The electron density can then be used to solve Eq. (2.6) for the spin orbitals. If the resulting wave functions are consistent with the initial ansatz, satisfying a specified convergence criterion, then the solution is found. If not, a new ansatz is constructed and the process reiterates until the convergence criterion is fulfilled. This type of iterative approach is termed a self-consistent field (SCF) method, and the iteration scheme is visualized in Fig. 2.1.

2.2.2 The Hartree–Fock Method

The Hartree approach to solving the many-body Schrödinger equation is not in agreement with the anti-symmetry principle, which states that fermions' wave functions are anti-symmetric, i.e. the wave function must change sign when the particles interchange [14, p. 201]. This is not the case for the Hartree product, since swapping one electron for another leaves the sign of the product unchanged.

A correction to this violation is presented in the Hartree–Fock (HF) method, where the use of a Slater determinant combines the single-electron wave functions while still adhering to the anti-symmetry principle. The N-electron wave function is expressed as the determinant of a single-electron wave function matrix,

$$\psi(\mathbf{x}_1, \ldots, \mathbf{x}_N) = \frac{1}{\sqrt{N!}} \begin{vmatrix} \chi_1(\mathbf{x}_1) & \chi_2(\mathbf{x}_1) & \cdots & \chi_N(\mathbf{x}_1) \\ \chi_1(\mathbf{x}_2) & \chi_2(\mathbf{x}_2) & \cdots & \chi_N(\mathbf{x}_2) \\ \vdots & \vdots & \ddots & \vdots \\ \chi_1(\mathbf{x}_N) & \chi_2(\mathbf{x}_N) & \cdots & \chi_N(\mathbf{x}_N) \end{vmatrix}, \tag{2.10}$$

where the determinant coefficient is a normalization factor. In addition to obeying the anti-symmetry principle, the HF method also satisfies the Pauli exclusion principle, which states that no two fermions can occupy the same quantum state simultaneously [15]. This is true for the Slater determinant, as two electrons with identical coordinates or identical wave functions would cause the total wave function to vanish.

In addition to the Hartree method's energy terms of Eq. (2.6), the HF method includes an exchange potential V_{X}, which accounts for the antisymmetry of the total wave function. The following single-electron Schrödinger equations are then solved iteratively in a similar self-consistent fashion as in the Hartree method,

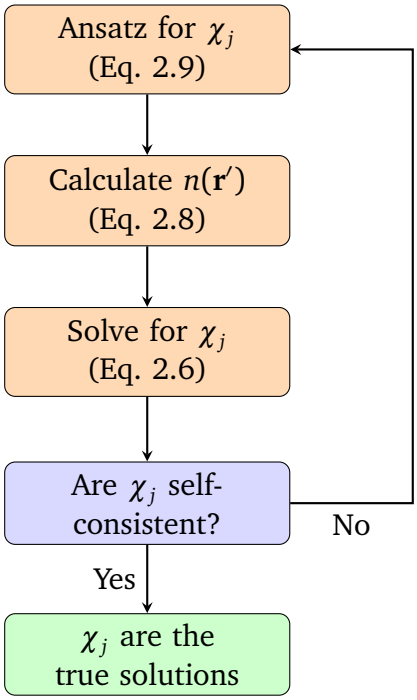

Figure 2.1: The Hartree iterative procedure.

$$\left[-\frac{\hbar^2}{2m}\nabla^2 + V(\mathbf{r}) + V_{\mathrm{H}}(\mathbf{r}) + V_{\mathrm{X}}(\mathbf{r})\right]\chi_j(\mathbf{x}) = E_j\chi_j(\mathbf{x}). \tag{2.11}$$

2.3 The Hohenberg–Kohn Theorems

The bedrock on which DFT rests consists of two mathematical theorems proved by Hohenberg and Kohn in 1964 [16], and a set of equations derived by Kohn and Sham in 1965 [17]. The first Hohenberg–Kohn theorem reads:

Theorem 1. *The ground state energy from Schrödinger's equation is a unique functional of the electron density.*

Every ground state electron density can be mapped to exactly one ground state wave function and thus produce a unique ground state energy. A functional is simply a function that takes in another function as a variable and generates an output. In other words, the theorem states that there exists an ground state energy functional of the ground state electron density $E[n(\mathbf{r})]$.

This theorem carries immense implications. We now merely have to compute the three-dimensional electron density to uniquely determine the

properties of the ground state, instead of solving for the $3N$-dimensional wave function directly. Thus, the computational cost is drastically reduced.

While Hohenberg and Kohn's first theorem proves that such a functional exists, their second theorem describes how to find it:

Theorem 2. *The electron density that minimizes the energy of the overall functional is the true electron density corresponding to the full solution of the Schrödinger equation.*

That is, if one knows the form of the energy functional, one can use the variational principle to determine the true ground state energy, i.e. varying the electron density until the energy is minimized.

2.4 The Kohn–Sham Equations

So, now that the fundamental theorems are in place, we need to know which energy functionals to include in the Schrödinger equation. Recall from Eq. (2.8) that the electron density is defined by the single-electron orbitals ψ_i, so we can write the energy as a functional of ψ_i,

$$E[\{\psi_i\}] = E_{\text{known}}[\{\psi_i\}] + E_{\text{XC}}[\{\psi_i\}], \tag{2.12}$$

where $E_{\text{known}}[\{\psi_i\}]$ is the collection of all analytically known energy terms and $E_{\text{XC}}[\{\psi_i\}]$ is the remaining energy contribution, called the exchange-correlation functional. The known energy terms are

$$\begin{aligned} E_{\text{known}}[\{\psi_i\}] = -\frac{\hbar^2}{m}\sum_i \int \psi_i^* \nabla^2 \psi_i \, d^3r + \int V(\mathbf{r}) n(\mathbf{r}) d^3r \\ + \frac{e^2}{2}\int\int \frac{n(\mathbf{r}) n(\mathbf{r}')}{|\mathbf{r}-\mathbf{r}'|} d^3r \, d^3r' + E_{\text{ion}}, \end{aligned} \tag{2.13}$$

i.e. the electron kinetic energy, the Coulomb interactions between the electrons and the collective nuclei, the electron-electron pair Coulomb interactions, and the nuclei-nuclei pair Coulomb interactions, respectively.

Kohn and Sham proved that the task of actually minimizing the total energy functional could be accomplished by solving a set of single-electron equations, later termed the Kohn–Sham equations,

$$\left[-\frac{\hbar^2}{2m}\nabla^2 + V(\mathbf{r}) + V_{\text{H}}(\mathbf{r}) + V_{\text{XC}}(\mathbf{r}) \right] \psi_i(\mathbf{r}) = \epsilon_i \psi_i(\mathbf{r}). \tag{2.14}$$

The Kohn–Sham equations are somewhat similar to the many-body Schrödinger equation, Eq. (2.2), except that they involve only one electron and are solved for a single-electron wave function instead of the $3N$-dimensional total wave function. The first three energy terms are the same as the those introduced in the HF method (Eq. (2.6)), i.e. the kinetic energy term, the electrostatic interaction between the electron and the collection of nuclei, and the Hartree potential, defined in Eq. (2.7). The final term, the exchange-correlation functional, is mathematically defined as

$$V_{\text{XC}}(\mathbf{r}) = \frac{\delta E_{\text{XC}}(\mathbf{r})}{\delta n(\mathbf{r})}, \tag{2.15}$$

that is, the functional derivative of the exchange-correlation energy with respect to the electron density.

As was the case for the HF method, the process of solving the Kohn–Sham equations is circular and must be done in iterations. An initial ansatz for the electron density is defined and used to solve the Kohn–Sham equations for the single-electron wave functions. The wave functions are then used to calculate the electron density, which is compared to the trial density. If the difference between the two is smaller than the specified convergence criterion, then it is the ground state electron density and is used to calculate the ground state energy of the system. If not, a new electron density trial function is created and the cycle is repeated until convergence. This iterative procedure, like the Hartree method, is a self-consistent field method and is illustrated in the flowchart of Fig. 2.2.

2.5 Exchange-Correlation Functionals

The Hohenberg–Kohn theorems and the Kohn–Sham equations provide the foundation of DFT, but there is still one essential piece missing. As we saw in Eq. (2.14), the exchange-correlation functional is necessary to solve the Kohn–Sham equations, but it is unknown in all but one instance. In a uniform electron gas, the electron density $n(\mathbf{r})$ is constant in space and the exchange-correlation functional $V_{\text{XC}}^{\text{electron gas}}$ can be exactly defined. This result can be used to solve the Kohn–Sham equations for a specific system by setting the exchange-correlation functional at position $\mathbf{r}$ to be the uniform electron gas exchange-correlation functional of the electron density at the given position. That is,

$$V_{\text{XC}}^{\text{LDA}}(\mathbf{r}) = V_{\text{XC}}^{\text{electron gas}}[n(\mathbf{r})]. \tag{2.16}$$

As this method uses the local electron density to approximate the

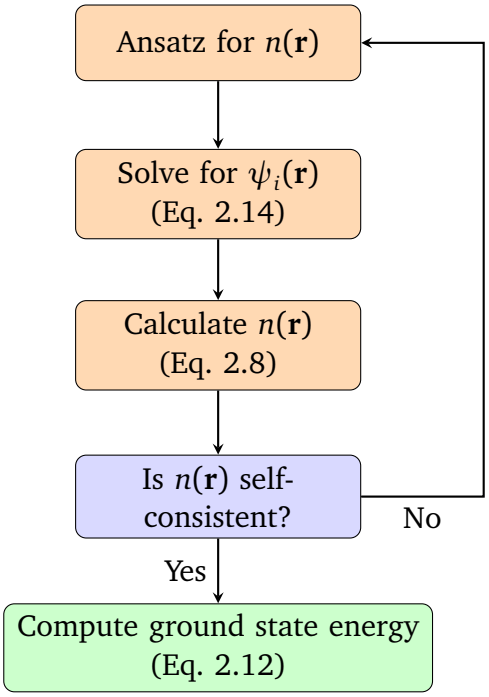

Figure 2.2: The iterative procedure of the Kohn–Sham equations.

exchange-correlation functional, it is called the local density approximation (LDA).

In real materials, LDA is of limited use, since the variation of the electron density is a vital part of how materials' properties differ. However, the LDA is important in the construction of more elaborate functionals, such as the approach called the generalized gradient approximation (GGA). GGA functionals combine the local electron density with the local gradient in the electron density in their approximation,

$$V_{\mathrm{XC}}^{\mathrm{GGA}}(\mathbf{r}) = V_{\mathrm{XC}}[n(\mathbf{r}), \nabla n(\mathbf{r})]. \tag{2.17}$$

When the electron density is constant, the non-empirical GGA functionals converge to the exact energy of the uniform electron gas. Thus, they satisfy the uniform density limit. Since the GGA functionals include more physical information in their approximations, they provide a more accurate result for most systems, with a few exceptions.

The approach as to how the density gradient is included into the functional can vary a great deal, and there exists a multitude of different GGA functionals. One such functional is the Perdew–Burke–Ernzerhof (PBE) functional, developed by the three authors in 1996 [18]. The PBE functional is non-empirical and widely applicable for many different systems.

Although it is not always the most accurate GGA, its universality has made it one of the most extensively used functionals to date.

A revised version of the PBE functional was introduced in 2008, called the Perdew–Burke–Ernzerhof for solids (PBEsol), which aimed to improve equilibrium properties of bulk solids and their surfaces [19]. PBEsol provides more accurate predictions of lattice constants than PBE, which often overestimates these quantities [20].

Another branch of exchange-correlation functionals are the hybrid functionals, which integrate parts of the exact exchange from Hartree–Fock theory [12, p. 218]. Hybrid functionals may provide more accurate estimates of several properties in solid state physics, including the band gap and structural properties, but carry a markedly higher computational cost than GGA- or LDA-based functionals [21]. One of the most widely used hybrid functionals for solid state systems is the Heyd–Scuseria–Ernzerhof (HSE06) functional [22, 23], which is based on the PBE functional with the incorporation of exact exchange into the short-range interaction [12, p. 219].

2.6 Crystal Structures

A *crystal* is made up of atoms or ions arranged in a periodic fashion in three dimensions [24, p. 3]. The smallest group of atoms that is repeated in the crystal, called the *basis*, is attached to a set of points in space, referred to as the *lattice*. Any point in the lattice can be described by an integer combination of the three translation vectors $\mathbf{a}_1$, $\mathbf{a}_2$, and $\mathbf{a}_3$,

$$\mathbf{r} = n_1\mathbf{a}_1 + n_2\mathbf{a}_2 + n_3\mathbf{a}_3. \tag{2.18}$$

All lattice points are equivalent, meaning their properties are invariant to any translation by the lattice vectors.

The *primitive lattice* is defined by the *primitive lattice vectors*, which constitute the smallest volume that can be used to generate the crystal structure. A special type of primitive unit cell is the *Wigner–Seitz cell*, illustrated in Fig. 2.3. The Wigner–Seitz cell is constructed by Voronoi decomposition, i.e. separating the lattice volume into regions around each lattice point such that every position in one region is closer to the corresponding lattice point than any other lattice point [24, p. 6].

The 14 distinct types of three-dimensional lattice structures are called *Bravais lattices*. Rutile and anatase, the two most common polymorphs of titanium dioxide [1, p. 13], and the subjects of this report, are both part of the tetragonal lattice system. Tetragonal lattices are rectangular prisms

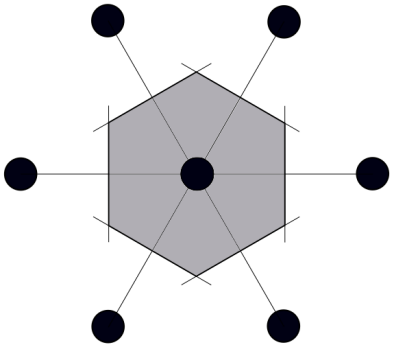

Figure 2.3: Wigner–Seitz cell, highlighted in gray.

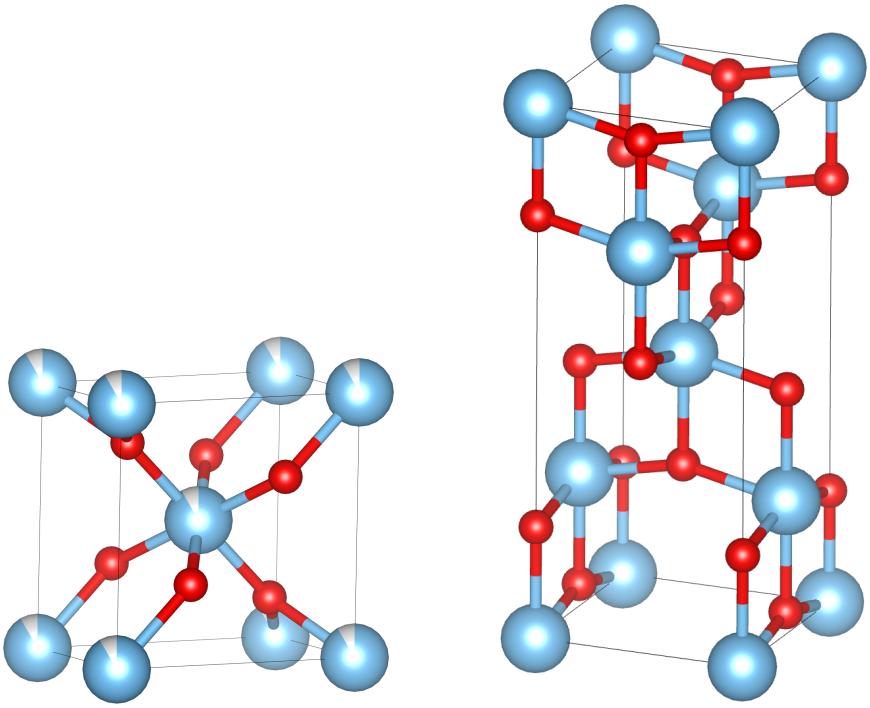

(a) Rutile **(b)** Anatase

Figure 2.4: Conventional unit cells of rutile and anatase TiO_2, created in VESTA [25]. The larger, blue balls are titanium atoms and the smaller, red balls are oxygen atoms.

in which one side length is different from the other two. The Bravais lattices of rutile and anatase are the primitive tetragonal lattice and the body-centered tetragonal lattice, respectively [26]. The conventional unit cells of both polymorphs are shown in Fig. 2.4.

2.7 Reciprocal Space

For mathematical convenience, DFT predominantly utilizes the Fourier transform of the real, three-dimensional space, called the *reciprocal space* or *k-space*. The latter term comes from the fact that the reciprocal space is spanned by the infinite set of wave vectors $\mathbf{k}$, whereas real space is spanned by the position vector $\mathbf{r}$. Analogous to the translation vectors in real space, we have three axis vectors of the reciprocal lattice describing positions in k-space, defined by

$$\begin{aligned}\mathbf{b}_1 &= 2\pi \frac{\mathbf{a}_2 \times \mathbf{a}_3}{\mathbf{a}_1 \cdot (\mathbf{a}_2 \times \mathbf{a}_3)},\\ \mathbf{b}_2 &= 2\pi \frac{\mathbf{a}_3 \times \mathbf{a}_1}{\mathbf{a}_1 \cdot (\mathbf{a}_2 \times \mathbf{a}_3)},\\ \mathbf{b}_3 &= 2\pi \frac{\mathbf{a}_1 \times \mathbf{a}_2}{\mathbf{a}_1 \cdot (\mathbf{a}_2 \times \mathbf{a}_3)}.\end{aligned} \tag{2.19}$$

Each axis vector $\mathbf{b}_i$ is orthogonal to two of the lattice vectors, i.e.

$$\mathbf{b}_i \cdot \mathbf{a}_i = 2\pi\delta_{ij}. \tag{2.20}$$

Any point in the reciprocal lattice can be expressed by a linear combination of the three vectors defined by Eq. (2.19),

$$\mathbf{G} = m_1\mathbf{b}_1 + m_2\mathbf{b}_2 + m_3\mathbf{b}_3, \tag{2.21}$$

where $\mathbf{G}$ is called a *reciprocal lattice vector* [24, p. 31].

Lengths in reciprocal space are inversely related to the lengths in real space. For example, a tetragonal unit cell with two long side lengths and one short one, like rutile, will have two short side lengths and one long one in k-space. This attribute is of relevance when sampling k-points (see Sect. 2.9).

The reciprocal space equivalent to the Wigner–Seitz cell is the *first Brillouin zone*, usually referred to simply as the Brillouin zone (BZ). Some points in the Brillouin zone are of high symmetry and are given letter names, such as Γ where $\mathbf{k} = 0$. The Brillouin zone of rutile and anatase, with selected k-points, is shown in Fig. 2.5.

2.8 Bloch's Theorem

For the study of systems with a periodic potential, such as a crystal lattice, the solutions of the Schrödinger equation must satisfy Bloch's theorem [24,

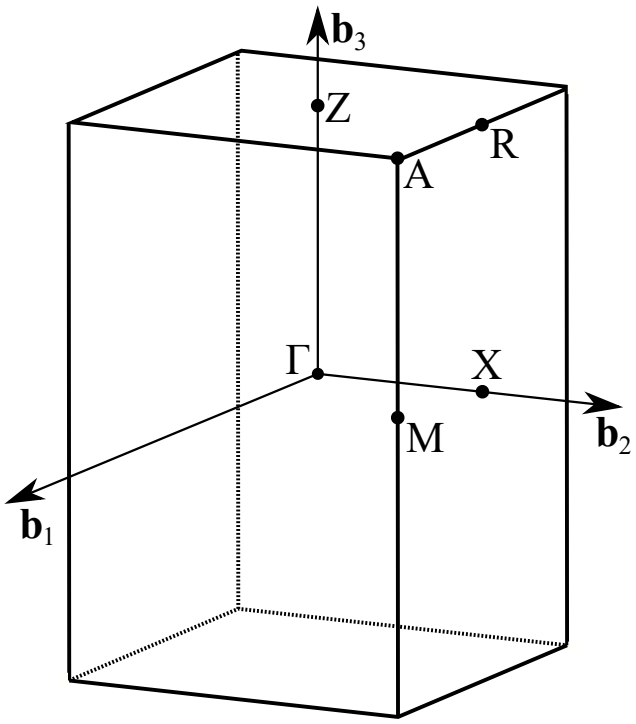

(a) Rutile

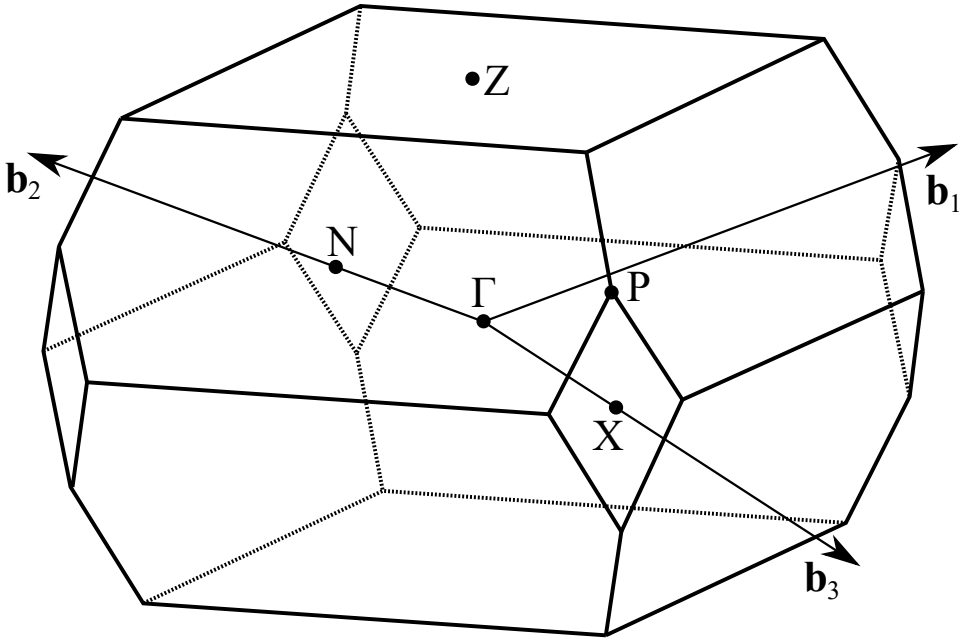

(b) Anatase

Figure 2.5: The first Brillouin zone of rutile and anatase TiO_2. Marked are the high symmetry *k*-points used in the computations.

p. 169]. This theorem states that the solutions take the form

$$\psi_{\mathbf{k}}(\mathbf{r}) = u_{\mathbf{k}}(\mathbf{r})e^{i\mathbf{k}\cdot\mathbf{r}}, \tag{2.22}$$

where $u_{\mathbf{k}}(\mathbf{r})$ carries the same periodicity as the crystal lattice, i.e. $u_{\mathbf{k}}(\mathbf{r}) = u_{\mathbf{k}}(\mathbf{r}+n_1\mathbf{a}_1+n_2\mathbf{a}_2+n_3\mathbf{a}_3)$ for all integers n_1, n_2, and n_3. In other words, the wave functions are a product of some periodic function $u_{\mathbf{k}}(\mathbf{r})$ and a plane wave $e^{i\mathbf{k}\cdot\mathbf{r}}$. Thus, these types of calculations are commonly referred to as plane-wave calculations.

A Bloch function with a wave vector $\mathbf{k}'$ outside the first Brillouin zone can always be modified with a reciprocal lattice vector $\mathbf{G}$, such that the new wave vector $\mathbf{k} = \mathbf{k}' + \mathbf{G}$ is located within the first Brillouin zone [24, p. 225]. Mathematically,

$$\begin{aligned}\psi_{\mathbf{k}'}(\mathbf{r}) &= e^{i\mathbf{k}'\cdot\mathbf{r}}u_{\mathbf{k}'}(\mathbf{r}) = e^{i\mathbf{k}\cdot\mathbf{r}}(e^{-i\mathbf{G}\cdot\mathbf{r}}u_{\mathbf{k}'}(\mathbf{r})) \\ &= e^{i\mathbf{k}\cdot\mathbf{r}}u_{\mathbf{k}}(\mathbf{r}) = \psi_{\mathbf{k}}(\mathbf{r}).\end{aligned} \tag{2.23}$$

Since both $e^{-i\mathbf{G}\cdot\mathbf{r}}$ and $u_{\mathbf{k}'}(\mathbf{r})$ have the periodicity of the crystal, so too does $u_{\mathbf{k}}(\mathbf{r}) = e^{-i\mathbf{G}\cdot\mathbf{r}}u_{\mathbf{k}'}(\mathbf{r})$, and $\psi_{\mathbf{k}}$ is thus also a Bloch function. In other words, because of periodicity, each Bloch function $\psi_{\mathbf{k}}$ is only unique within the first Brillouin zone, and we can restrict the calculations to this area without loss of generality.

2.9 *k*-Space Sampling

The Brillouin zone is an essential concept in DFT because a large portion of the calculations take the form

$$\bar{g} = \frac{V_{\text{cell}}}{(2\pi)^3}\int_{\text{BZ}} g(\mathbf{k})d\mathbf{k}, \tag{2.24}$$

where some function $g(\mathbf{k})$ is integrated over all k in the first Brillouin zone. Such integrals are approximated numerically by summing the function values at discrete points multiplied with a corresponding weight. These discrete k-points are chosen within the bounds of the integral, i.e. within the first BZ.

A number of different approaches to selecting the k-points used for the BZ integration have been developed. None have been as widely used as the method devised by Monkhorst and Pack in 1976 [27]. For this method, the user only has to specify the number of k-points to be sampled in each direction in reciprocal space. It is generally reasonable to select these numbers

to be proportional to the lengths of the respective reciprocal lattice vectors. If all three lattice vectors in real space are of equal length, so too will the reciprocal lattice vectors be, and the standard choice would be an $M \times M \times M$ Monkhorst–Pack grid. If two of the lattice vectors $\mathbf{a}_1$ and $\mathbf{a}_2$ are of equal length and the third one is smaller, $a_3 < a_{1,2}$, then the opposite relation would be true in reciprocal space, i.e. $b_3 > b_{1,2}$. Thus, the natural choice of k-points would be an $M \times M \times N$ grid, where $N > M$.

A denser set of k-points results in a more accurate energy approximation, but also a higher computational cost. It is therefore necessary to perform a convergence test of the given system to determine how many points are needed to get a well-converged result without using an unnecessary amount of computational resources.

2.10 Energy Cutoffs

As discussed in Sect. 2.8 and Eq. (2.22), the solutions we are seeking for periodic structures include a function $u_\mathbf{k}(\mathbf{r})$ which has equal periodicity to the crystal lattice. As a result of this periodicity, $u_\mathbf{k}(\mathbf{r})$ can be expanded by a set of plane waves,

$$u_\mathbf{k}(\mathbf{r}) = \sum_\mathbf{G} c_\mathbf{G} e^{i\mathbf{G}\cdot\mathbf{r}}, \tag{2.25}$$

where the reciprocal lattice vector $\mathbf{G}$ is defined by Eq. (2.21). Inserting Eq. (2.25) into Eq. (2.22) gives an updated expression for the Bloch function,

$$\psi_\mathbf{k}(\mathbf{r}) = \sum_\mathbf{G} c_{\mathbf{k}+\mathbf{G}} e^{i(\mathbf{k}+\mathbf{G})\mathbf{r}}. \tag{2.26}$$

Using this Bloch function exactly would mean summing up an infinite amount of points in k-space defined by $\mathbf{G}$, which for obvious reasons is impractical for a calculation following the laws of time and space. However, these Bloch functions are solutions to the Schrödinger equation, with kinetic energy

$$E_\mathrm{k} = \frac{\hbar^2}{2m}|\mathbf{k}+\mathbf{G}|^2. \tag{2.27}$$

Only kinetic energies up to some limit are of physical importance, as high-energy states are unlikely to be occupied. Therefore, the infinite sum of Eq. (2.26) can be limited by a value determined by the kinetic energy cutoff,

$$E_\mathrm{cut} = \frac{\hbar^2}{2m}G_\mathrm{cut}^2. \tag{2.28}$$

The Bloch function can then be expressed as

$$\psi_{\mathbf{k}}(\mathbf{r}) = \sum_{|\mathbf{G}+\mathbf{k}|<G_{\text{cut}}} c_{\mathbf{k}+\mathbf{G}} e^{i(\mathbf{k}+\mathbf{G})\mathbf{r}}. \tag{2.29}$$

The kinetic energy cutoff must be provided in the input of DFT calculations and should be tested for convergence.

2.11 Pseudopotentials

To not exclude the plane waves of core electrons one would have to select a large kinetic energy cutoff, since core electrons oscillate at a faster rate and have high kinetic energies. As discussed, it is computationally beneficial to select lower E_{cut}, but ignoring these inner electrons altogether would produce incorrect results. However, these tightly bound electrons need not be as precisely described as the loosely bound valence electrons, as it is the latter that are most critical in determining the properties of the system. Therefore, methods to approximate the properties of core electrons have been developed to reduce the computational cost of the calculations, the most common of which are pseudopotentials.

Pseudopotentials aim to approximate the electron density of a chosen set of core electrons, attempting to satisfy physical and mathematical characteristics of the true ion core. The ion core is then most commonly assumed to be fixed for all calculations, which is called the *frozen core approximation*. Pseudopotentials have a transferability, which is the property that they can be applied to the element in any system without needing to amend the pseudopotential.

A natural consequence of our discussion above, regarding core electrons and high kinetic energies, is that the choice of pseudopotential will have an effect on the minimum choice of E_{cut}. Pseudopotentials requiring a high E_{cut} are referred to as hard, while those requiring lower E_{cut} are called soft. Several different types of pseudopotentials have been constructed over the years, with ultrasoft pseudopotentials (USPP), the projector augmented-wave (PAW) method, and norm-conserving (NC) pseudopotentials being some of the most common.

2.12 DFT+U

While standard DFT shows acceptable accuracy in structural and cohesive properties, it is not as impressive in the prediction of electronic and optical properties [28]. For instance, it is well known that DFT systematically

underestimates the band gap of semiconductors and insulators, an error which has significant implications for the resulting electronic and optical data [12, p. 28]. These limitations arise due to the electron self-interaction in the Hartree potential of the Kohn–Sham equations – namely the unphysical electron repulsion of itself [12, p. 227]. A lack of perfectly accurate exchange-correlation functionals, which would cancel out this effect, has led to the development of correction methodologies.

One such correction method is DFT+U. The "+U" refers to the inclusion of an additional Hubbard U term in the DFT Hamiltonian. The standard DFT total energy functional can be extended in the DFT+U method as [29]

$$E_{\mathrm{DFT+U}}[n] = E_{\mathrm{DFT}}[n] + E_{\mathrm{U}}[n] - E_{\mathrm{DC}}[n]. \tag{2.30}$$

Here, $E_{\mathrm{DFT}}[n]$ is the standard DFT energy, $E_{\mathrm{U}}[n]$ is the Hubbard U term that takes into account the on-site Coulomb interaction, and $E_{\mathrm{DC}}[n]$ is the double counting correction term. $E_{\mathrm{U}}[n]$ represents the energy penalty of localizing electrons in the same atomic orbital, thus capturing the physics missed by standard DFT for strongly correlated electron systems. However, as the selection of an appropriate U value is typically system-dependent, this parameter is commonly adjusted to fit some known property of the system, such as the band gap or the lattice constant. Thus, DFT+U is usually of semiempirical nature [28].

2.13 The Fermi–Dirac Distribution

At absolute zero temperature, an N-electron system has no kinetic energy. The electrons then only fill the lowest energy orbitals while obeying the Pauli exclusion principle. The highest filled energy level of this ground state system is defined as the *Fermi energy* [24, p. 137].

As the temperature increases, the electron distribution will shift so that some former unoccupied orbitals will be occupied, and some occupied orbitals will be unoccupied. The *Fermi–Dirac distribution* provides the probability that an electron orbital with energy E is occupied under thermal equilibrium [24, p. 138],

$$f(E) = \frac{1}{e^{(E-\mu)/(k_B T)} + 1}. \tag{2.31}$$

Here, k_B is the Boltzmann constant, T is the temperature, and μ is the *chemical potential*, commonly referred to as the *Fermi level*. The Fermi level E_{F} is temperature dependent and is equal to the Fermi energy at absolute zero, as the electron distribution then becomes a step function, where

$f(E < E_F) = 1$ and $f(E > E_F) = 0$. $f(\mu) = \frac{1}{2}$ for all temperatures, meaning that the probability of an electron state with energy equal to the Fermi level being occupied is always 50%.

2.14 Energy Bands & Band Gap

Electrons bound to atoms are allowed to exist in quantized energy levels, but for solids these discrete levels are broadened into energy bands [30, p. 51]. The bands are quasi-continuous, in reality consisting of a multitude of discrete levels in close proximity, requiring only tiny amounts of energy to excite an electron from one state in the band to the next. The energy bands in the solids are separated by gaps of forbidden regions.

The band structure of a solid can be separated into two main phenomena, the first being that the highest occupied band is only partially filled. The second is that, at 0 K, the highest occupied energy band is completely filled with electrons, with an energy *band gap* (E_g) separating it from the next, completely unoccupied band. In the first case, electrons are able to flow freely under application of an electric field, and the material is said to be a metal. In the second case, the solid cannot conduct electricity at zero temperature, since there are no available states for electrons to move. These materials are called semiconductors or insulators, where the former has a lower band gap than the latter. The highest occupied bands are called the *valence bands* (VB), while the lowest unoccupied bands are called the *conduction bands* (CB).

The exact band gap value distinguishing semiconductors from insulators is somewhat arbitrary, but it is generally said that materials with a band gap greater than ~3 eV are insulators. Due to the band gap being of a lesser size in semiconductors, they have more excited electrons at nonzero temperatures, allowing for some conductivity. Semiconductors also have a better capability of absorbing photons and excite valence band electrons into the conduction band, an important characteristic for solar cells and other optoelectronic devices.

Different states in a band structure are not only characterized by their energies, but also by their wave vector $\mathbf{k}$. If the highest energy state in the VB and the lowest energy state in the CB have a different k-vector, the semiconductor is said to have an *indirect* band gap, whereas it is *direct* if they are equal.

2.15 Electronic Density of States

While the Fermi–Dirac function reveals the probability distribution of electrons in a system, it does not take into account the states available to the electrons. For that, we need the *density of states (DOS)*, which describes the number of electron states per unit energy range [24, p. 142]. The density of occupied electron states is then the product of these two functions, $f(E)D(E)$.

Density functional theory is able to estimate the DOS by integrating the electron density in k-space. Due to the k-space integration, there is a need for a greater number of k-points than in normal ground state energy calculations in order to get accurate results.

One can characterize the type of material in study by looking at the DOS at the Fermi level. The material is a metal if it has a nonzero number of states at the Fermi level, while it is a semiconductor or an insulator if the Fermi level is located within the band gap between the valence and conduction bands. The band gap can then be estimated by calculating the energy difference between the lowest state in the conduction band and the highest state in the valence band.

The DOS is an important characteristic of a semiconductor. The density around the conduction band edge, together with the Fermi–Dirac function, determines the charge carrier concentration, which at thermal equilibrium is equal to

$$n = \int_{E_c}^{\infty} f(E)D(E)dE, \tag{2.32}$$

where E_c is the conduction band edge energy [31, p. 92]. In turn, the charge carrier concentration defines the material's electrical conductivity σ,

$$\sigma = en\mu_n, \tag{2.33}$$

where e is the elementary charge and μ_n is the electron mobility [31, p. 103].

2.16 Dielectric Function and Absorption Coefficient

From Maxwell's equations, we have that the wave equation for the electric field in a medium can be expressed as [30, p. 349]

$$\nabla^2 \mathbf{E} = \varepsilon_A \mu_0 \frac{\partial^2 \mathbf{E}}{\partial t^2} + \sigma \mu_0 \frac{\partial \mathbf{E}}{\partial t}. \tag{2.34}$$

Here, we have assumed that the magnetic permeability μ is equal to μ_0. ε_A is the absolute dielectric constant and σ is the electrical conductivity. This wave propagates with dissipation and has a solution of the form

$$\mathbf{E} = \mathbf{E}_0 e^{i(\mathbf{k}\cdot\mathbf{r} - \omega t)}, \tag{2.35}$$

which, inserted into Eq. (2.34), gives

$$-k^2 = -\varepsilon_A \mu_0 \omega^2 - \sigma \mu_0 i\omega. \tag{2.36}$$

Expressed in terms of the vacuum speed of light c, this becomes

$$k = \frac{\omega}{c} \sqrt{\varepsilon + \frac{\sigma i}{\varepsilon_0 \omega}}, \tag{2.37}$$

where $c = 1/\sqrt{\mu_0 \varepsilon_0}$ and ε is the relative dielectric constant. The square root term is the complex refractive index,

$$n_r = \sqrt{\varepsilon + \frac{\sigma i}{\varepsilon_0 \omega}}, \tag{2.38}$$

which can be written as a combination of its real and imaginary parts,

$$n_r = n_r' + i n_r''. \tag{2.39}$$

The wavenumber k can then be expressed as

$$k = \frac{n_r' \omega}{c} + i n_r'' \frac{\omega}{c}, \tag{2.40}$$

which in turn can be inserted into the electric field wave Eq. (2.35), which, assuming propagation in the $+z$ direction, becomes

$$\mathbf{E} = \mathbf{E}_0 \exp\left\{ i\omega \left(\frac{n_r' z}{c} - t \right) \right\} \exp\left\{ \frac{-n_r'' \omega z}{c} \right\}. \tag{2.41}$$

The electric field wave thus experiences a damping effect, which is related to the medium's absorption of electromagnetic energy. The absorption coefficient is determined by the damping of the field wave's intensity, i.e. the square of Eq. (2.41), and is given by

$$\alpha(\omega) = \frac{2 n_r'' \omega}{c}. \tag{2.42}$$

The complex relative dielectric constant can be expressed in terms of its real and imaginary parts,

$$\varepsilon = \varepsilon_1 + i\varepsilon_2. \tag{2.43}$$

These bear the following relation to the complex refractive index:

$$\begin{aligned} \varepsilon_1 &= n_r'^2 - n_r''^2 \\ \varepsilon_2 &= 2n_r' n_r'' \end{aligned} \tag{2.44}$$

Solving Eq. (2.44) for n_r'' and inserting into Eq. (2.42) gives the absorption coefficient in terms of the relative dielectric constant

$$\alpha(\omega) = \frac{2\omega}{c}\sqrt{\frac{-\varepsilon_1 + \sqrt{\varepsilon_1^2 + \varepsilon_2^2}}{2}}, \tag{2.45}$$

which, upon exchanging the angular frequency with energy, becomes

$$\alpha(E) = \frac{2E}{\hbar c}\sqrt{\frac{-\varepsilon_1 + \sqrt{\varepsilon_1^2 + \varepsilon_2^2}}{2}}. \tag{2.46}$$

Thus, one can determine the absorption coefficient if the energy and the real and imaginary parts of the complex relative dielectric constant are known.

2.17 Critical Points

The band structure dictates the curve of the imaginary relative dielectric function [9, p. 262]. The absorption of a photon with energy $\hbar\omega$ can take place at any point within the Brillouin zone, as long as the energy is conserved [24, p. 434],

$$\hbar\omega = E_c(\mathbf{k}) - E_v(\mathbf{k}), \tag{2.47}$$

where c is a conduction band and v is a valence band. Primarily, the imaginary relative dielectric function is dominated by direct interband transitions. Although indirect optical transitions can occur with phonon assistance, their contributions are several orders of magnitude smaller than direct transitions [9, p. 265].

Spectral structures in the ε_2 spectrum, that is, peaks and "shoulders" [9, p. 253], are referred to as critical points (CPs) and signify the presence of a substantial number of possible direct VB to CB transitions at a specific

energy level [9, p. 262]. In the band structure, this is illustrated by valence bands and conduction bands exhibiting vertical translation, i.e. having the same line shape but shifted along the energy axis, for a given interval in k-space. In other words, points in the BZ where the energy difference between a CB and a VB remains unchanged [24, p. 435],

$$\nabla_{\mathbf{k}}[E_c(\mathbf{k}) - E_v(\mathbf{k})] = 0. \tag{2.48}$$

At these energies, $E_c(\mathbf{k}) - E_v(\mathbf{k})$, transitions accumulate and cause spectral structures in $\varepsilon_2(E)$. The critical points are, however, not solely determined by the quantity of the potential VB to CB transitions, but also by their respective transition probabilities [9, p. 260].

2.18 The PHS Method

Optical properties of materials can be computed using DFT methods. However, the precision of these calculations has demonstrated considerable variation [32–34]. Results have been shown to be highly dependent on the choice of exchange-correlation functional, injecting a level of unreliability and a necessity to compare with experimental data.

A solution to this was proposed by Nishiwaki and Fujiwara [8], and entails calculating ε_2 with a GGA functional (PBE) and a high density k-grid, before shifting the energy axis to fit the band gap determined by a hybrid functional (HSE06 [22, 23]) calculation. Finally, the spectrum amplitudes are corrected using a sum rule. This approach is referred to as the PHS (PBE+HSE06+Sum rule) method, and was shown by authors to produce optical data that closely match the experimental spectra for typical solar cell materials.

The first step of the PHS method is, as mentioned, calculating ε_2 using a GGA–PBE exchange-correlation functional and a highly dense k-mesh. To compensate for the DFT band gap underestimation [12, p. 28], the ε_2 spectrum is shifted to match the band gap of a calculation based on the hybrid functional HSE06.

$$\Delta E_g = E_{g,\mathrm{HSE}} - E_{g,\mathrm{PBE}} \tag{2.49}$$

Here, $E_{g,\mathrm{HSE}}$ and $E_{g,\mathrm{PBE}}$ are the band gaps computed with HSE06 and PBE, respectively. $E_{g,\mathrm{HSE}}$ is a suitable reference value because the HSE06 functional is among the most accurate for estimating the band gap [35].

When shifting the spectrum, one has to make sure that the sum rule is satisfied [36, p. 622]:

$$\int E\varepsilon_2(E)dE = \text{const.} \tag{2.50}$$

With an energy correction value of ΔE_g, it follows that

$$\int E\varepsilon_{2,\text{PBE}}(E)dE = \int (E+\Delta E_g)\varepsilon_{2,\text{shift}}(E+\Delta E_g)dE, \tag{2.51}$$

where $\varepsilon_{2,\text{shift}}$ is the shifted imaginary relative dielectric function. Assuming the coefficients E and ΔE_g are constant, we derive

$$\int \varepsilon_{2,\text{shift}}(E+\Delta E_g)dE = f\int \varepsilon_{2,\text{PBE}}(E)dE, \tag{2.52}$$

where $f = E/(E+\Delta E_g)$. Thus, it follows that $\varepsilon_{2,\text{shift}}(E+\Delta E_g) = f\,\varepsilon_{2,\text{PBE}}(E)$. Redefining the E axis so that $E+\Delta E_g \to E$, and setting $\varepsilon_{2,\text{PHS}}(E) = \varepsilon_{2,\text{shift}}(E)$, we get the final expression of the imaginary relative dielectric function:

$$\varepsilon_{2,\text{PHS}}(E) = \frac{E-\Delta E_g}{E}\varepsilon_{2,\text{PBE}}(E-\Delta E_g). \tag{2.53}$$

The real relative dielectric function can then be derived by Kramers–Kronig integration [36, p. 620]:

$$\varepsilon_{1,\text{PHS}}(E) = 1 + \frac{2}{\pi}\mathcal{P}\int_0^\infty \frac{E'\varepsilon_{2,\text{PHS}}(E')}{E'^2-E^2}dE', \tag{2.54}$$

where $\mathcal{P}$ signifies the principal part of the integral.

To determine the absorption coefficient $\alpha_{\text{PHS}}(E)$, one merely has to insert $\varepsilon_{1,\text{PHS}}$ and $\varepsilon_{2,\text{PHS}}$ into Eq. (2.46).

2.19 Intermediate Band Solar Cells

Although conventional solar cells have vastly improved the last couple of decades, they are restricted by the Shockley–Queisser (SQ) limit, which states that the absolute efficiency for a single-gap solar cell is 40.8% under maximum sunlight illumination [37, 38]. As the efficiencies of these conventional solar cells are approaching their theoretical limit, the interest in third-generation solar cells, introducing novel designs in order to exceed the SQ limit, has increased markedly [39–42]. One such design is the intermediate band solar cell (IBSC), which has an ideal efficiency limit of 63.2% under maximum sunlight concentration [43]. Whereas traditional solar cells employ a standard semiconductor as the absorbing material, the

IBSC is based on a material uniquely defined by the presence of an isolated electronic band, known as the intermediate band (IB), positioned between the VB and CB.

A fundamental limitation of conventional solar cells is their utilization of only a portion of the solar spectrum [44]. Exciting electrons from the VB to the CB requires a photon energy equal to or greater than the band gap. Photons with a smaller energy will not be absorbed, while photons with a greater energy will result in a thermalization process – an electron excited to a state above the conduction band edge, almost instantaneously relaxed back to the edge while releasing heat. The IBSC reduces this problem by introducing two more optical transitions, thus allowing a wider range of electromagnetic radiation to be absorbed and reducing energy loss.

As shown in Fig. 2.6, the introduction of an intermediate band splits the band gap (E_g) into two sub-band gaps, the lowest one (E_L) and the highest one (E_H). In the case of a non-infinitesimal intermediate bandwidth, the IB has a width of ΔE_{IB}, with a distance to the CB and the VB of $E_{C,I}$ and $E_{I,V}$, respectively. At thermal equilibrium, the Fermi level is located inside the IB [44]. This means that there exist two main mechanisms for creating an electron-hole pair: a direct transition from the VB to the CB (labeled 1 in Fig. 2.6) and a two-step excitation process from the VB to the IB (2a) and then to the CB (2b).

To maximize absorption of the electromagnetic spectrum, the IB should ideally not be positioned in the middle of the band gap, since that would result in only two distinct band gap energies (E_g and $E_L = E_H$). Whether the IB exists above or below the middle of the band gap, however, is insignificant.

The optimal theoretical efficiency limit of 63.2% assumes an infinitesimally small bandwidth of the intermediate band, which in practice is not realistic. Therefore, Levy and Honsberg conducted an analysis in 2008 that examined the contrasting impacts of a finite band width: its beneficial effect, in that it can prevent recombination through the intermediate band, and its negative effect, as it reduces optical absorption [45]. They determined that the optimal width for the intermediate band is less than or approximately equal to 825 meV, which yields a theoretical efficiency of 57.9%. When this condition is fulfilled, the highest efficiencies are achieved when the smallest band gap ($E_{C,I}$ or $E_{I,V}$) is roughly 100 meV lower and the second smallest band gap ($E_{I,V}$ or $E_{C,I}$) is roughly $400 - 500$ meV higher than 825 meV.

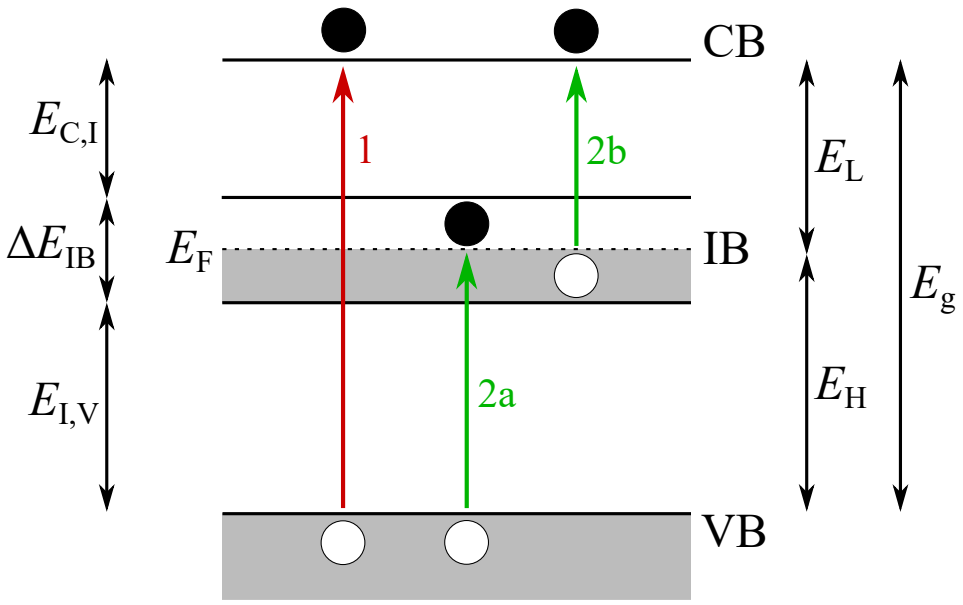

Figure 2.6: Sketch of the band diagram of an IB material, with the Fermi level E_F. The colored arrows illustrate the three optical transitions, 1 representing the direct transition from the VB to the CB, whereas 2a and 2b show the transitions facilitated by the IB. For an infinitesimally narrow IB, the band gap E_g is divided into two sub-band gaps, E_L and E_H, determined by the position of the IB. In the case of a finite length, the IB has a width of ΔE_{IB}, with a distance to the CB and the VB of $E_{C,I}$ and $E_{I,V}$, respectively.

Chapter 3

Computational Methods

3.1 Software & Infrastructure

The open-source software Quantum ESPRESSO (QE), versions 6.7 and 7.1, was utilized for the computations in this thesis [46]. QE, which is built upon the principles of DFT, employs plane wave basis sets and pseudopotentials. The calculations were carried out in parallel across 32 CPU cores on the Idun and the Hemmer clusters, both high-performance computing infrastructures housed at NTNU [47].

3.2 General Computational Procedure

Unless stated otherwise, the following methodology was consistently applied for all structures discussed in this thesis.

The total energy of the systems was computed using the SCF method detailed in Sect. 2.4, using the *pw.x* program in QE. The *k*-meshes, constructed on the basis of the Monkhorst-Pack method, were tested for convergence, alongside the kinetic energy cutoff values. The *k*-points in each direction were selected proportional to the lengths of the respective reciprocal lattice vectors, in order to attain equal *k*-point density in all directions. The number of electronic states (*nbnd*) was set to 30 more than the number of occupied states at zero temperature, in order to compute states in the conduction bands in addition to the valence bands.

For each unique structure, geometry optimization was carried out with the aim of identifying the most stable configuration with the lowest possible ground state energy. This was achieved through a *vc-relax* calculation in the *pw.x* program, optimizing both the atomic positions and the lattice parameters.

To approximate the band structure, an initial SCF calculation was executed prior to running a *bands* calculation in *pw.x*. High-symmetry k-points required for the *bands* calculations were identified using XCrySDen [48]. Appropriate k-point weights were selected to provide a detailed resolution of the band diagrams. Finally, the post-processing tool *bands.x* was executed before plotting the resulting band structures.

Density of states calculations were preceded by an SCF calculation employing the same parameters as above, with the exception of using Blöchl's tetrahedron method [49] for interpolation in k-space, securing a more accurate integration [12, p. 182]. Since DOS calculations involve integrating the electron density in k-space, a denser grid was necessary for precise results. Consequently, a non-self-consistent field (NSCF) calculation was executed post the SCF run, with a k-point grid of $30 \times 30 \times 30$. The DOS was then determined using the *dos.x* program. It is worth noting that QE's unit for DOS is states per energy (eV) per unit cell volume. Thus, it is generally the case that calculations with larger units cells result in higher DOS.

For dielectric function calculations, an initial SCF run was conducted, followed by an NSCF computation – this time setting the parameters *nosym* and *noinv* to *.true.*. This was due to *epsilon.x* not allowing a reduction of the k-point grid. Similar to the DOS calculations, a grid configuration of $30 \times 30 \times 30$ was utilized. The complex dielectric function was computed with the *epsilon.x* program, setting the calculation to *eps* and utilizing Gaussian smearing with 0.20 eV as the broadening parameter for the interband contribution. The absorption coefficient was then calculated by inserting the real and imaginary parts of the relative dielectric function into Eq. (2.46).

3.3 Pseudopotential & Exchange-Correlation Functional

Different exchange-correlation functionals (XC) paired with pseudopotentials (PP), listed in Table 3.1, were trialed on rutile and anatase TiO_2. The lattice parameters and band gaps of the two TiO_2 polymorphs were calculated and compared to known values from experimental literature, in order to choose the most accurate pair for further calculations. Additionally, the DOS was computed to see a more detailed electronic comparison. The norm-conserving pseudopotential with the PBE functional were chosen for subsequent computations. The converged k-point grid and kinetic energy cutoff E_{cut} with all PP–XC pairs were $7 \times 7 \times 11$ and $E_{\text{cut}} = 400$ Ry for rutile and $8 \times 8 \times 8$ and $E_{\text{cut}} = 450$ Ry for anatase.

Table 3.1: Overview of the different pseudopotential (PP) files with attached exchange-correlation functionals (XCs) used in this thesis.

PP	Method	XC	Reference
PAW	LDA	PZ	[50]
PAW	GGA	PBE	[18]
PAW	GGA	PBEsol	[19]
NC	GGA	PBE	[18]
NC	Hybrid	HSE06	[22, 23]

3.4 The PHS Method

After performing standard DFT calculations, the optical data of rutile and anatase were processed according to the PHS method, detailed in Sect. 2.18. Due to memory requirements beyond our resources, the HSE06 band gap $E_{\mathrm{g,HSE}}$ in Eq. (2.49) was replaced with experimentally measured band gaps from existing literature. These values were 3.03 eV for rutile and 3.20 eV for anatase [51]. The semi-empirical nature of this substitution made the approach unsuitable for the other configurations of this thesis, as experimental data were lacking. The integral of Eq. (2.54) was calculated numerically using Simpson's method [52, p. 223].

3.5 Critical Point Analysis

3.5.1 Second Derivative Analysis

The dielectric functions obtained from the PHS method were used as a basis for detecting critical points, as the energies will match experimental data more closely. The PHS post-processing should not significantly affect the CPs, aside from the energy shift and a slight amplitude adjustment.

Not all critical points of the imaginary relative dielectric function are in the form of local maxima, but may also manifest as a "shoulder" [9, p. 253]. Therefore, merely finding the roots of the first derivative is insufficient to detect all critical points. As such, a second derivative analysis was conducted to identify the CPs of rutile and anatase, based on the PHS data. This was done to confirm the change in concavity associated with an observed spectral structure in a dielectric function, denoting a CP. A peak or a shoulder CP will occur around the points where the second derivative experiences a local minimum below zero.

The derivatives, $d\varepsilon_2/dE$ and $d^2\varepsilon_2/dE^2$, were calculated numerically, after smoothing out the function with a Savitzky–Golay filter [53]. The convolution coefficients, set to a cubic polynomial and a window size of 25, were chosen to smooth out digital noise while maintaining minimal distortion of the line shape.

The exact placements of the shoulder critical points were then determined visually by the use of plotting tools, while for the peak critical points, the exact energy was found by calculating the roots of the first derivative.

3.5.2 Vertical Translation Analysis

To locate the transitions in k-space responsible for the CPs, a Python script was developed to analyze the band structures of rutile and anatase. This script compares each valence band to each conduction band and identifies regions in k-space where the two bands are vertical translations of each other, meaning they have the same line shape but are shifted along the energy axis. Typically, but not exclusively, this means that the bands are parallel.

The script is based on Eq. (2.48). To identify vertical translation, the code analyzes the transition energies, $E_t(\mathbf{k}) = E_c(\mathbf{k}) - E_v(\mathbf{k})$, between each VB to each CB. If the transition energy between two bands remains unchanged for a stretch in k-space longer than *kinterval*, then they are are considered vertical translates at that particular k-vector. *kinterval* is set to 0.15 Å^{-1}, a length visualized in Fig. 3.1.

If the energy difference between two E_t within a k-space interval exceeds the parameter *dEt*, then the two bands are not considered vertical translates at that interval. In other words, *dEt* defines the maximum allowed difference between the highest and the lowest E_t of a vertical translation point. *dEt* is set to 0.02 eV, a relatively strict requirement that was tested to ensure exclusion of transitions that are clearly not vertical translates.

To differentiate the contributions of different transitions, a weighting coefficient is assigned to each transition. This coefficient is proportionally based on the extent of their vertical translation intervals. For instance, in the case of two linear bands, the weighting coefficient would be determined by the distance in k-space over which the bands are parallel.

Finally, the critical points from the vertical translation analysis were compared to those from the second derivative analysis, after readjusting the latter's energies back (see Eq. (2.49) of Sect. 2.18). The CPs from the vertical translation analysis that matched those from the second derivative analysis, within an interval of ±0.04 eV, were visualized in the band

structure as optical transitions. This interval was selected based on the uncertainty of visual accuracy when determining the precise location of the CP shoulders, and potential discrepancies between the electronic and optical DFT calculations. The main functions of the vertical translation analysis code is provided in the appendix 5.

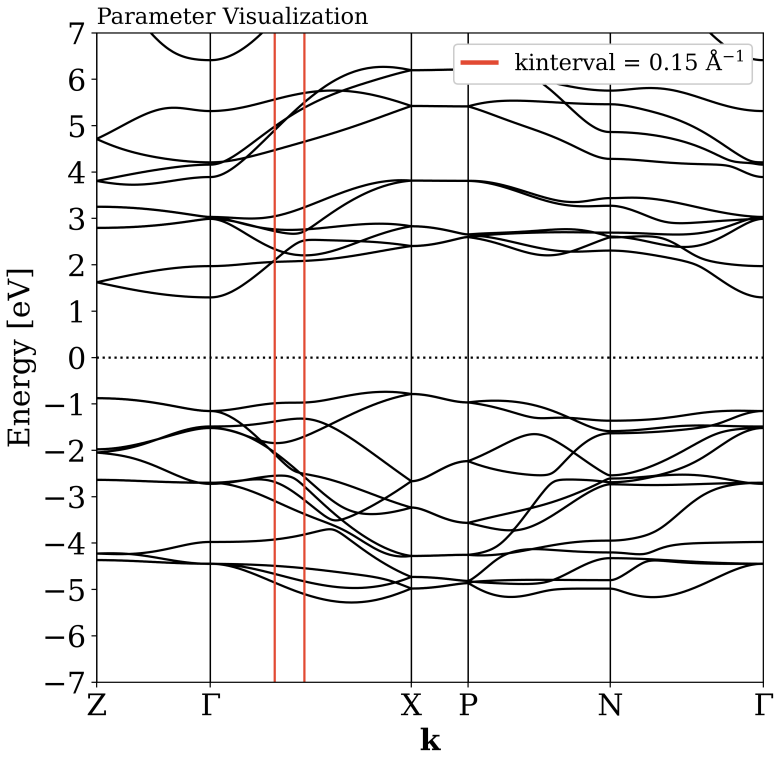

Figure 3.1: Example band diagram illustrating the *kinterval* parameter of the vertical translation analysis code, visualized as the distance between the two vertical orange lines.

3.6 DFT+U

In an effort to obtain more precise electronic and optical properties of rutile and anatase, the DFT+U method was employed. The only pseudopotential file available that allowed calculations with this method was the projector augmented-wave pseudopotential with the PBEsol functional, and was thus selected for these calculations.

The Hubbard parameter was applied to the atomic orbitals dominant around the band gap, that is, close to the valence band maximum and

the conduction band minimum. To identify these orbitals, the projected density of states was computed for both rutile and anatase with the PAW pseudopotential and PBEsol functional. Initial SCF and NSCF calculations were carried out in the same manner as the DOS calculations, described in Sect. 3.2, prior to the execution of the *projwfc.x* program.

The Hubbard parameter was calibrated so that the resulting band gaps closely matched empirical data, i.e. 3.03 eV for rutile and 3.20 eV for anatase, with a precision up to two decimal points. Due to the influence of the U parameter on geometrical properties, geometry optimization was conducted prior to each SCF calculation that determined the band gaps.

Following the parameter tests, the DOS and the band structure of the two polymorphs were computed. However, technical constraints prevented optical calculations using the DFT+U method, thus precluding its use in further calculations. A DOS calculation using the PBEsol functional and identical parameters as the DFT+U calculations was conducted for both polymorphs, in order to study the effects of the Hubbard parameter.

3.7 Modified TiO_2 Configurations

Electronic and optical properties of various doped configurations of TiO_2 were computed following the procedure outlined in Sect. 3.2, in order to investigate their usefulness in IBSC technology. The configurations investigated included both rutile and anatase co-doped with CrN, as well as rutile doped with Mo, as listed in Table 3.2. When doped with CrN, the supercells underwent substitution where one Ti atom and one O atom were respectively replaced with Cr and N atoms bound together. In the case of the supercell doped with Mo, a single Ti atom was substituted with a Mo atom.

The main objective of computing the properties of doped TiO_2 structures was to assess their potential applicability in IBSC technology. Primarily, that includes investigating whether an intermediate band appears between the valence and conduction band, as well as studying the materials' response to an external electromagnetic field.

In addition to the doped structures, properties of an anatase structure with a 3.1% oxygen vacancy were computed, to study the effects of such a point defect. For this, an anatase $2 \times 2 \times 2$ supercell was utilized, with a removal of 1/32 of the O atoms.

Table 3.2: Overview of the different doping configurations investigated, including the kinetic energy cutoff value E_{cut} and the k-mesh used.

Polymorph	Dopant	Doping [%]	Supercell	E_{cut} [Ry]	k-mesh
Rutile	CrN	50	$1 \times 1 \times 1$	150	$5 \times 5 \times 8$
	CrN	25	$2 \times 1 \times 1$	150	$3 \times 6 \times 9$
	CrN	12.5	$2 \times 2 \times 1$	200	$2 \times 2 \times 6$
	Mo	25	$2 \times 1 \times 1$	300	$3 \times 6 \times 9$
Anatase	CrN	50	$1 \times 1 \times 1$	200	$6 \times 6 \times 6$
	CrN	25	$2 \times 1 \times 1$	300	$8 \times 8 \times 3$
	O vacancy	3.1	$2 \times 2 \times 2$	300	$4 \times 4 \times 3$

Chapter 4

Results & Discussion

4.1 Pseudopotential & Exchange-Correlation Functional Tests

The results of the lattice parameters and band gaps of rutile and anatase, based on the different pseudopotential and exchange-correlation functional pairs, are listed in Table 4.1. Due to insufficient computer memory resources, computations with the HSE06 functional were not possible at an acceptable precision level.

All PP–XC pairs showed decent ability in predicting structural properties of titania, as is generally the case with DFT calculations [12, p. 222]. PBE consistently overestimates the lattice parameters of both polymorphs. This is an expected phenomenon, as discussed in Sect. 2.5, and is to some degree corrected in the PBEsol functional, which was the most accurate functional for predicting the structural properties.

While there was little difference between the two PBE pseudopotentials (PAW and NC), the PZ functional consistently underestimated the lattice parameters and exhibited the greatest deviations from experimental data. This is not unexpected, since this functional was the only one based on the LDA method, and thus does not take the electron density gradient into account. Even so, all PP–XC pairs predicted the lattice parameters within -1.4% to $+2.3\%$ of the empirical equivalents.

The band gaps, however, were markedly underestimated by all functionals, with relative errors between 30.9% and 39.3%. As mentioned, conventional DFT methods systematically undervalue the band gap, our calculations being no exception. Similar DFT calculations on TiO_2 have yielded similar band gaps. For instance, the PBE functional has been reported to yield band gaps of 2.08 [54], 2.19 [55], 2.20 [56], and 2.36 eV [54], while ours were determined 2.14 eV (PAW) and 2.21 eV (NC).

Table 4.1: Lattice parameters (a, c) and band gaps (E_g) of rutile and anatase, derived from the combinations of pseudopotentials (PPs) and exchange-correlation functionals (XC), compared to their respective experimental values (a_{exp}, c_{exp}, $E_{\text{g,exp}}$). Experimental values for rutile are $a_{\text{exp}} = 4.59$ Å, $c_{\text{exp}} = 2.96$ Å, and $E_{\text{g,exp}} = 3.03$ eV, while for anatase, they are $a_{\text{exp}} = 3.78$ Å, $c_{\text{exp}} = 9.51$ Å, and $E_{\text{g,exp}} = 3.20$ eV [1, p. 15] [51].

Polymorph	PP	XC	a [Å]	a/a_{exp}[%]	c [Å]	c/c_{exp}[%]	E_{g} [eV]	$E_{\text{g}}/E_{\text{g,exp}}$ [%]
Rutile	PAW	LDA–PZ	4.56	99.3	2.92	98.6	1.84	60.7
	PAW	GGA–PBE	4.65	101.3	2.97	100.3	1.84	60.7
	PAW	GGA–PBEsol	4.60	100.2	2.95	99.7	1.85	61.1
	NC	GGA–PBE	4.64	101.1	2.97	100.3	1.90	62.7
	NC	Hybrid–HSE06	-	-	-	-	-	-
Anatase	PAW	LDA–PZ	3.75	99.2	9.49	99.8	2.11	65.9
	PAW	GGA–PBE	3.80	100.5	9.73	102.3	2.14	66.9
	PAW	GGA–PBEsol	3.77	99.7	9.58	100.7	2.13	66.6
	NC	GGA–PBE	3.80	100.5	9.71	102.1	2.21	69.1
	NC	Hybrid–HSE06	-	-	-	-	-	-

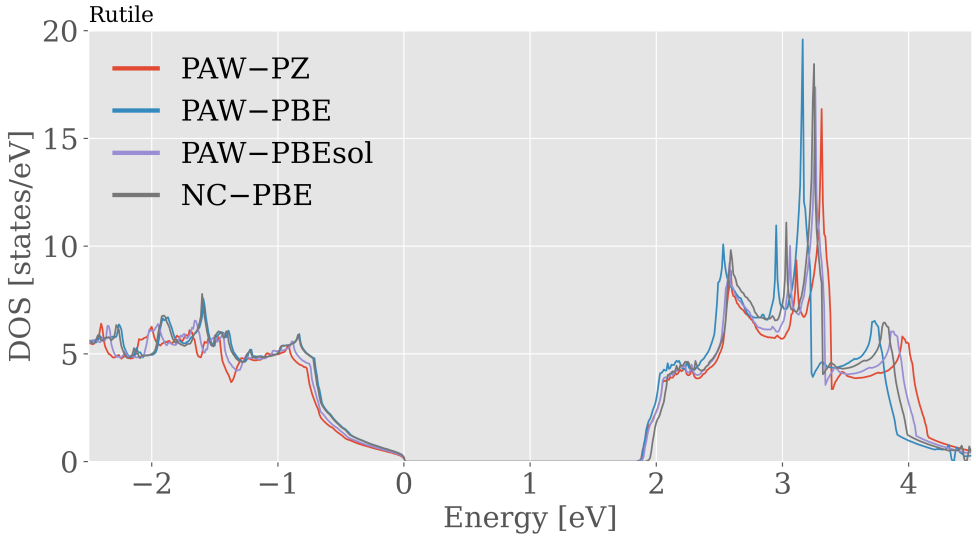

(a)

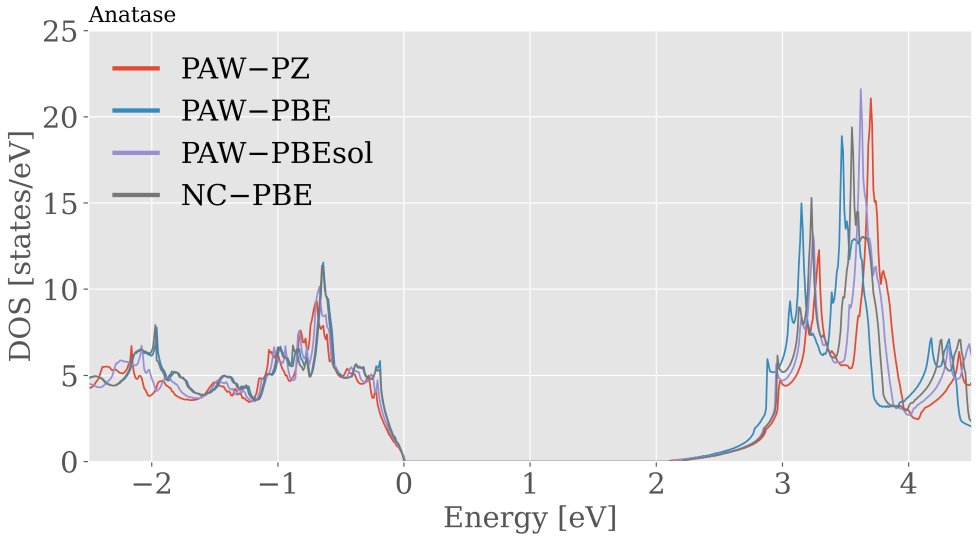

(b)

Figure 4.1: The DOS of (a) rutile and (b) anatase, as calculated by the different pseudopotential–exchange-correlation functional pairs. The energy axis is calibrated so that each valence band maximum aligns at $E = 0$ eV.

Although none were optimal, the most precise PP–XC pair for determining the band gap was the NC pseudopotential with the PBE functional. Even though the PBEsol functional gave the best structural predictions, the electronic properties were more important for the purposes of this thesis, and so the NC–PBE file was selected for further calculations, unless other-

wise stated.

Fig. 4.1 shows a comparison of the DOS computed by the different PP–XC pairs. The energy axis is adjusted so that each valence band maxima is located at $E = 0$ eV – a more practical zero point for comparison than the Fermi energies. The different spectra exhibit the same trends and share all major structures, though they are increasingly shifted further from the VB maximum. If anything, these results illustrate that there are only minimal electronic differences separating these conventional DFT methods, even in the case of the LDA functional.

4.2 Electronic Properties of TiO_2

4.2.1 Band Structure

The band structures of rutile and anatase, computed with the NC pseudopotential and the PBE functional, are displayed in Fig. 4.2. Both polymorphs have the Fermi energy positioned inside a band gap, which correctly implies that they are semiconductors. Rutile has a direct band gap, with the highest state in the valence band and the lowest state in the conduction band both situated at the Γ point. However, several points within the CB possess energy levels just about 4% greater than the Γ point, particularly at M, between M and Γ, and at R. Prior literature has highlighted this phenomenon, suggesting that rutile may have a direct band gap or a nearly equivalent indirect band gap [57].

In contrast, the band gap nature of anatase is more readily interpretable and exhibits an indirect gap. The peak state in the VB is close to the X point, along the line between Γ and X, while the CB minimum is at the Γ point. This indirect band gap has previously been reported in other GGA-based first-principles studies [58–60]. Some references calculate the band structure using symmetry points appropriate for a simple tetragonal lattice, which makes direct comparison challenging [55, 61].

4.2.2 Density of States

The NC–PBE-based DOS plots from Fig. 4.1 are also presented in Fig. 4.3, to better distinguish its features and show a wider energy range. As with the band structures, the Fermi energy, now equated to $E = 0$ eV, resides within a band gap, confirming the semiconducting nature of both polymorphs.

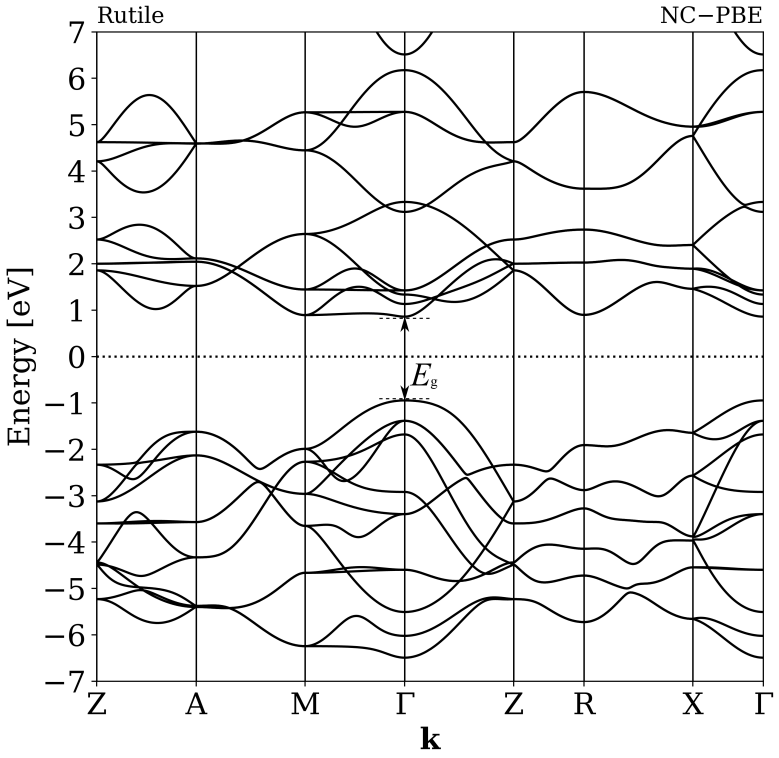

(a)

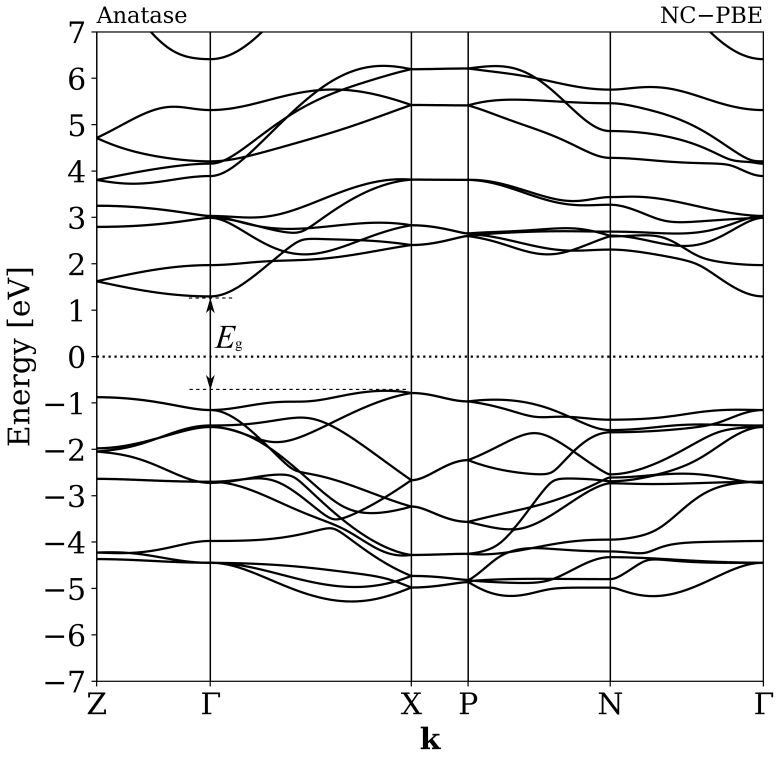

(b)

Figure 4.2: Band structure of (a) rutile and (b) anatase, computed with the NC pseudopotential and the PBE functional, with the Fermi energy set to $E = 0$ eV.

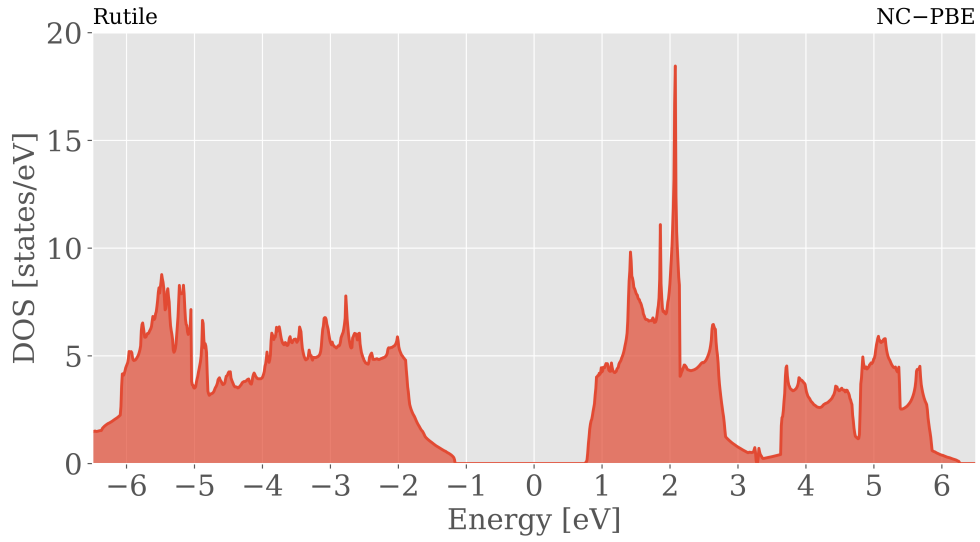

(a)

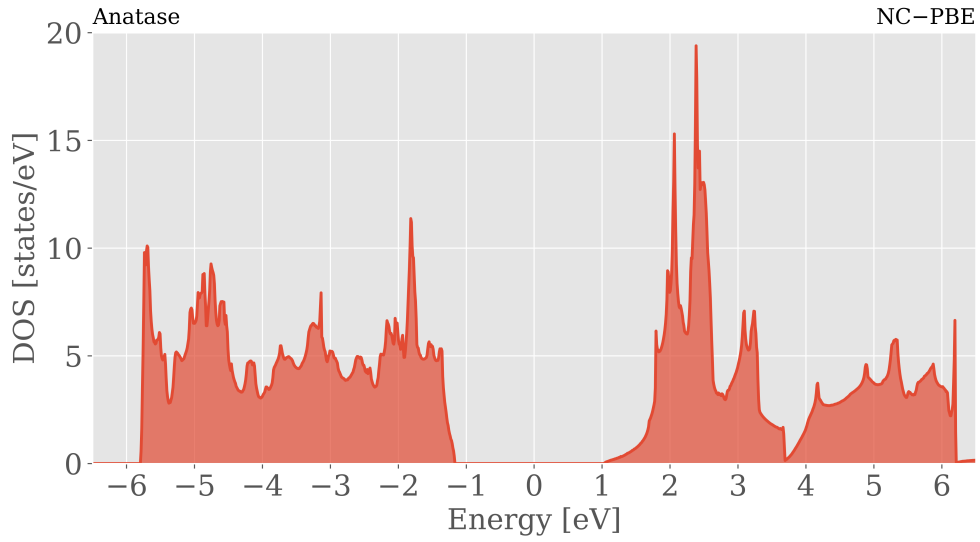

(b)

Figure 4.3: The DOS of (a) rutile and (b) anatase, computed with the NC pseudopotential and the PBE functional, with the Fermi energy set to $E = 0$ eV.

The band structure and the DOS plots are directly related. Energy levels that consist of a large number of available states within the band structure – particularly where bands are more horizontally aligned – are likely to exhibit a high DOS. Oppositely, the levels with fewer available states will display a lower DOS.

It is apparent from Fig. 4.3a that rutile has a comparatively low DOS

around the VB edge. This observation corresponds well with Fig. 4.2a, where the only available states near the VB edge exist around the Γ point. Conversely, near the CB minimum, there is a significant incline in DOS, which correlates to the flat band found between the M and Γ points and the states around the R point in the band structure.

Anatase's DOS presents an opposite behavior with a significant number of states at the VB edge and fewer states at the lower segment of the CB, as visualized in Fig. 4.3b. Once again, this characteristic is replicated in the band structure shown in Fig. 4.2b, with bands providing more states around the VB maximum than at the CB minimum.

With rutile's direct band gap and a higher DOS at the CB edge, one might predict it to be a superior conductor than anatase. This is because exciting VB electrons to the CB edge does not necessitate a momentum shift and phonon assistance, and an elevated DOS around the CB edge tends to boost conductivity, according to Eqs. (2.32) and (2.33). Nevertheless, the abundance of oxygen vacancies in anatase, which can serve as electron donors, results in anatase displaying higher conductivity than rutile, as reported in the literature [62].

4.3 Optical Properties of TiO_2 and the PHS Method

The dielectric function and absorption coefficient, calculated using the PHS method and the NC–PBE pseudopotential-functional pair, are shown in Figs. 4.4 and 4.5 for rutile and Figs. 4.6 and 4.7 for anatase. Given our primary interest in TiO_2 for photovoltaic applications, we have constrained the energy axis to 6.5 eV (= 191 nm). This limit is set because only a minuscule portion of sunlight reaching the Earth's surface exceeds this energy level [63].

Since both polymorphs have a tetragonal structure, their optical properties are anisotropic, leading to a different dielectric function and absorption coefficient along the a and c axes. This anisotropy is evident in the figures, depicting clear differences between the ordinary (a) and the extraordinary (c) axes.

The dielectric function represents the response of a medium to an electric field, where the real part ε_1 quantifies the field's ability to permeate the material and the imaginary part ε_2 measures the material's capacity to absorb or dissipate energy. Consequently, ε_2 is zero for energies below the band gap in both polymorphs and rises with the number of possible optical transitions from valence bands to conduction bands.

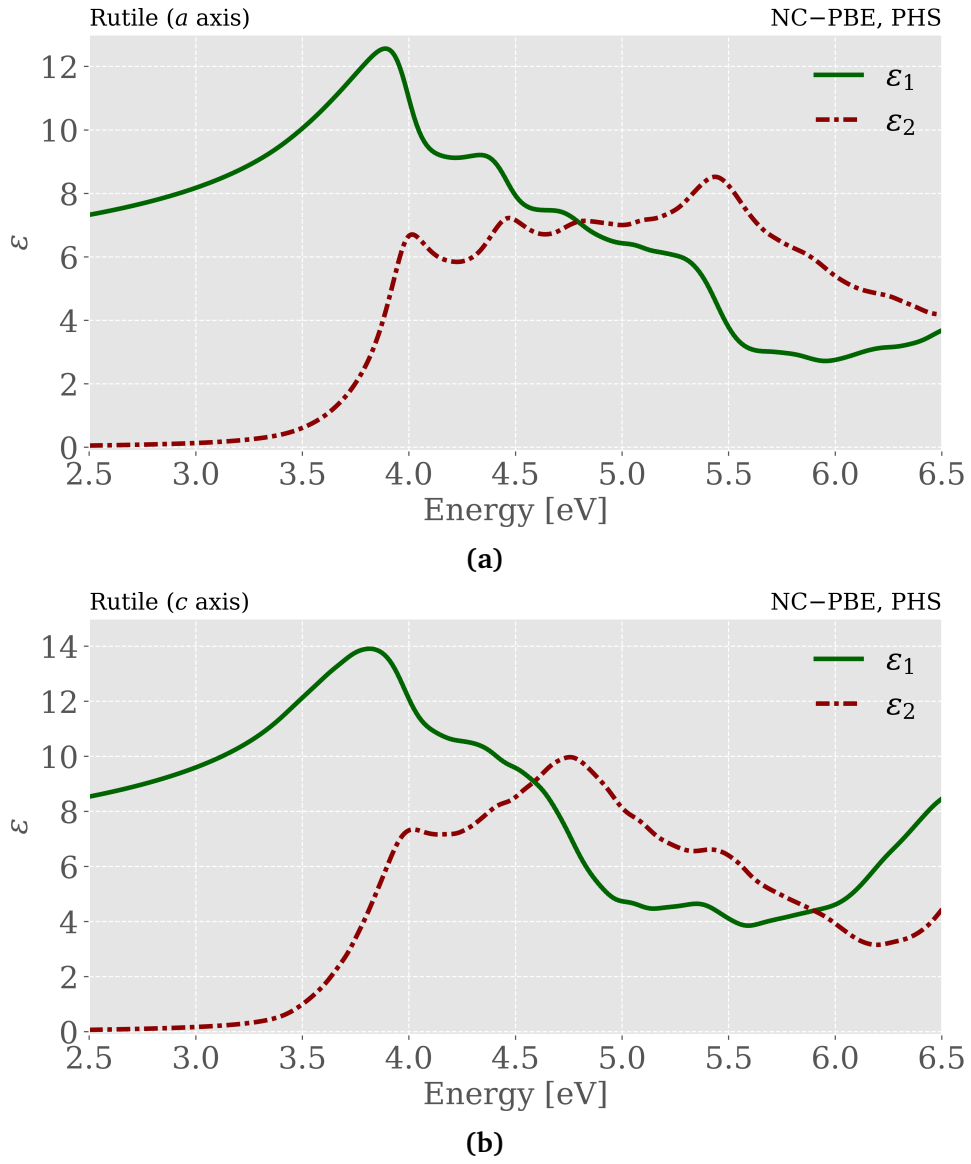

Figure 4.4: Dielectric function of rutile along the (a) ordinary and the (b) extraordinary axes. The spectra are computed according to the PHS method, with the NC pseudopotential and the PBE functional.

Before delving into the ε_2 CP analysis in Sect. 4.4, it can be useful to look at the overall trends and precision of our optical data.

Rutile is reported to have a major $\varepsilon_{2,a}$ peak at ~ 4.1 eV [64, 65], which matches well with Fig. 4.4a. A smaller structure at ~ 4.6 eV found in the literature may correspond to the local maximum at ~ 4.4 eV in Fig. 4.4a. Other smaller structures are difficult to find in the experimental data, except for the local maximum at ~ 5.5 eV which is in good agreement with

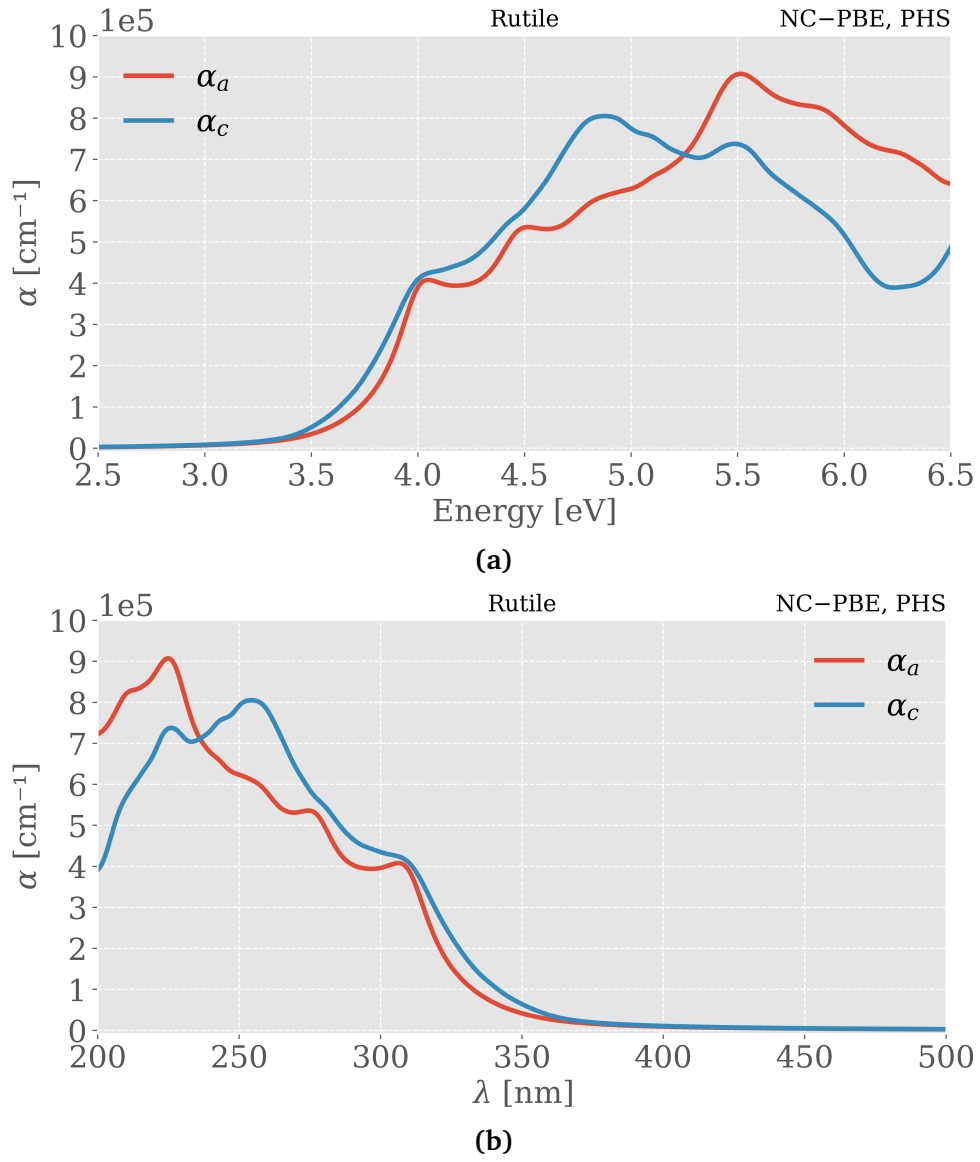

Figure 4.5: Absorption coefficient of rutile as a function of (a) photon energy and (b) photon wavelength. The spectra are computed according to the PHS method, with the NC pseudopotential and the PBE functional.

the peak at ∼ 5.5 eV of Fig. 4.4a, although the amplitudes deviate. $\varepsilon_{2,c}$ is similarly reported to have a major peak at ∼ 4.2 eV [64, 65], matching the maximum at ∼ 4.0 eV of Fig. 4.4b. Although this peak is reported markedly higher than the $\varepsilon_{2,a}$ equivalent, they are of similar magnitude in our data. None of the other structures of Fig. 4.4b are found in the ellipsometry literature.

The $\varepsilon_{1,a}$ maximum at ∼ 3.9 eV aligns well with the literature peak at

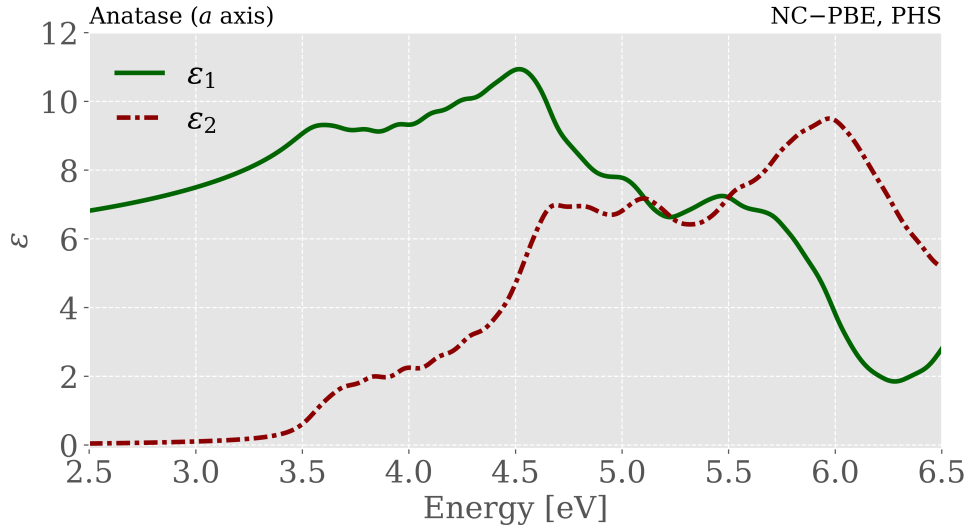

(a)

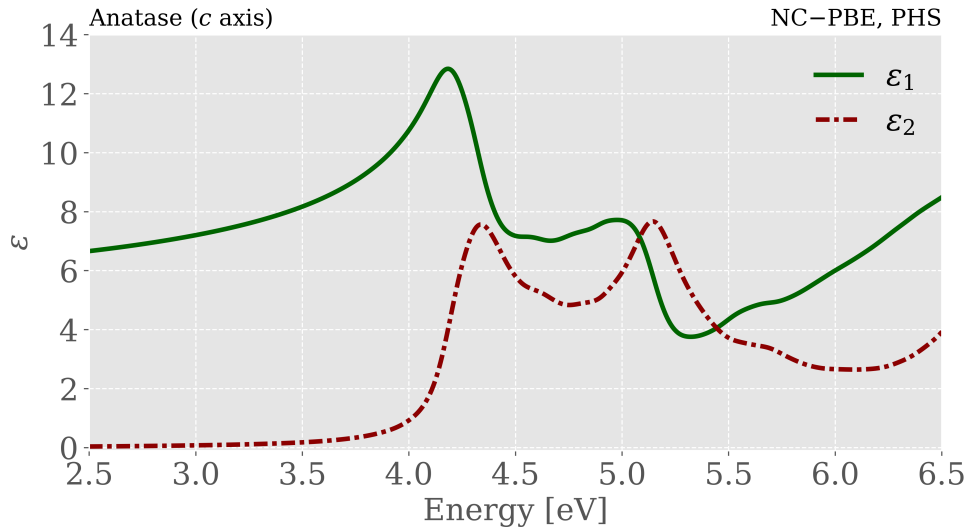

(b)

Figure 4.6: Dielectric function of anatase along the (a) ordinary and the (b) extraordinary axes. The spectra are computed according to the PHS method, with the NC pseudopotential and the PBE functional.

$\sim$ 3.8 eV. So does the $\varepsilon_{1,c}$ peak at $\sim$ 3.8 eV, which corresponds to a literature peak of $\sim$ 3.8 eV. The remaining ε_1 spectra correlate well with the general trends but show discrepancies in smaller structures and amplitudes.

As for anatase, Jellison et al. report an incline of $\varepsilon_{2,a}$ from 3.5 eV to a shoulder structure at $\sim$ 4.0 eV, before a broad peak at around 4.8 eV [65]. This pattern is partially visible in Fig. 4.6a, although Jellison et al. do not report energies above 5.6 eV. The two maxima of $\varepsilon_{2,c}$, at $\sim$ 4.3 and $\sim$ 5.1

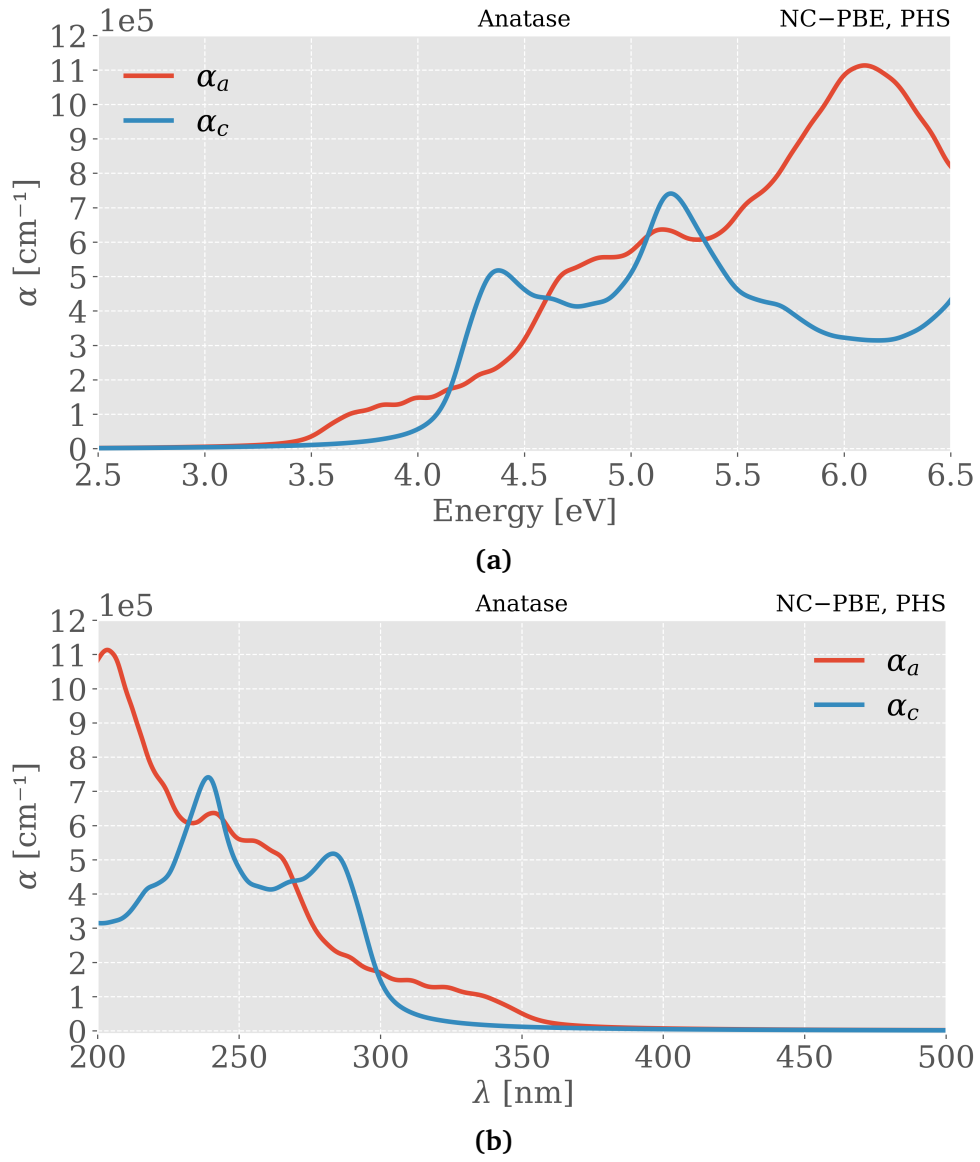

Figure 4.7: Absorption coefficient of anatase as a function of (a) photon energy and (b) photon wavelength. The spectra are computed according to the PHS method, with the NC pseudopotential and the PBE functional.

eV, are in good agreement with the ellipsometry peaks – although Jellison et al. measured the second peak to be significantly smaller than the first, which is not reflected in Fig. 4.6b.

Ellipsometry data for $\varepsilon_{1,a}$ reveal two main features, a maxima at ~ 3.8 eV and a shoulder at ~ 4.5 eV [65]. This is only partially corroborated by our data, as Fig. 4.6a depicts multiple closely spaced structures after 3.5 eV, and a highest maximum at ~ 4.5 eV. $\varepsilon_{1,c}$ displays a maximum at ~ 4.1 eV in

literature, closely matching the maximum at ~ 4.2 eV in Fig. 4.6b, before a steep decline. However, Jellison et al. do not report the local maximum at ~ 5.0 eV seen in our data.

The plots of the absorption coefficient as a function of both photon energy and wavelength, are represented in Figs. 4.5a and 4.5b for rutile, and Figs. 4.7a and 4.7b for anatase. As expected, the absorption coefficient exhibits a slow, almost negligible, increase at the band gap, specifically at 3.03 eV for rutile and 3.20 eV for anatase. This behavior is attributed to the limited number of optical transitions possible just above the band gap energy.

In examining the absorption coefficient, parallels can be drawn with the dielectric function, particularly in how the trends are linked with the DOS and band structure. This is a logical correlation as the absorption coefficient is directly calculated from the dielectric function according to Eq. (2.46). Higher values of ε_2 yield a greater α since this imaginary part is connected with energy loss, as previously discussed. There is, however, not a straightforward relation between ε_1 and α, despite $\alpha \propto n_r''$ (Eq. 2.42) and $\varepsilon_1 \propto -n_r''^2$ (Eq. 2.44). That is because both $n_r'^2$ and $n_r''^2$ of Eq. (2.44) are frequency dependent [30, p. 349].

Rutile displays superior absorption capabilities along its c axis for UVA and UVB rays, while demonstrating increased absorption along the a axis for UVC rays. Conversely, anatase's absorption coefficient is markedly higher along the a axis for UVA rays, with absorption along both axes alternating for shorter wavelengths. It is worth noting that neither polymorph displays significant absorption of visible light, attributed to their expansive band gaps. Rutile typically demonstrates a higher absorption coefficient than anatase in the long-wavelength UV range, a finding that aligns with other ab initio calculations [61, 66]. Broadly speaking, the overall trends and magnitudes of $\alpha(\lambda)$ exhibit consistency with these calculations, although local variations may deviate, akin to the dielectric function.

The PHS method has demonstrated decent ability in predicting the dielectric function and absorption coefficient of rutile and anatase. The most notable spectral structures and broad trends tend to agree well with the experimental data, although anomalies occur and detailed structures in the DFT spectra are often not confirmed by ellipsometry. The latter is a common phenomenon for optical DFT calculations [67–69], and other GGA-based calculations show strong correlation to our dielectric functions [67, 69]. Additionally, the amplitudes of our ε spectra frequently diverge from those reported in the literature, occasionally computed as low as 25%-50% of the empirical data, although at other instances they exhibit a higher degree of precision.

The necessitated choice to amend the PHS method and adjust the band gaps to the empirical values greatly limits the applicability of our approach to systems with unknown band gaps, such as doped TiO_2. Adhering to the standard PHS procedure and employing an HSE06 functional would resolve this issue and reduce the empirical nature of our approach.

4.4 Critical Point Analysis

4.4.1 Second Derivative Analysis

The second derivatives of ε_2 for both polymorphs are plotted in Figs. 4.8 and 4.10. In the approximate location of each negative local minimum is attached a label indicating the critical point, exactly determined by the roots of the first derivative (peaks) or visual determination (shoulders). For the sake of simplicity, the CPs are denoted E_1, E_2, etc., with a unique set of labels for each axis. Figs. 4.9 and 4.11 show the dielectric function spectra along with the critical points for rutile and anatase, respectively. The CPs marked in the figures are also listed in Table 4.2.

When comparing our critical points to experimental literature, perhaps the most notable discrepancy is the relatively large number of CPs we have identified. Yet, some lines can be drawn between our results and the literature.

In our energy range, rutile's CPs in the a direction have been reported to be 4.00 eV (large peak), 5.35 eV (small peak), and 6.10 eV (shoulder) by Cardona and Harbeke [70], 4.1 eV (large peak) by Jellison et al.[1] [65], and 4.0 eV (large peak), 4.6 eV (shoulder), and 5.4 eV (small peak) by Tiwald and Schubert [64]. The first CP reported by these authors matches well with $E_{1a} = 4.01$ eV, which appears as the earliest local maximum. The E_{5a} CP at 5.44 eV may also correlate to Cardona and Harbeke's at 5.35 eV and Tiwald and Schubert's at 5.4 eV, although these are relatively small peaks, while E_{5a} is a relatively large peak. Aside from the possibility of the local maximum $E_{3a} = 4.82$ eV being the equivalent of Tiwald and Schubert's shoulder at 4.6 eV, and the shoulders $E_{6a} = 5.86$ eV or $E_{7a} = 6.25$ eV matching with Cardona and Harbeke's shoulder at 6.10 eV, the other CPs are not found in the experimental literature.

In the c direction, all three references report only one CP at 4.11 eV (Cardona and Harbeke), 4.3 eV (Jellison et al.), and 4.2 eV (Tiwald and Schubert). This matches relatively well with our first CP $E_{1c} = 4.02$ eV. All other eight critical points are not documented in the mentioned literature,

[1] Jellison et al. did not report energies above 5.5 eV.

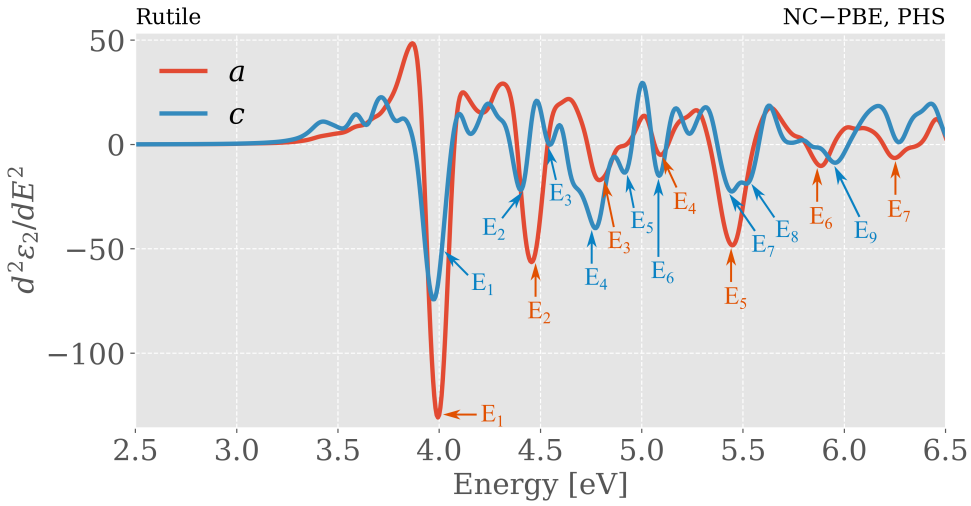

Figure 4.8: Second derivative of ε_2 for rutile.

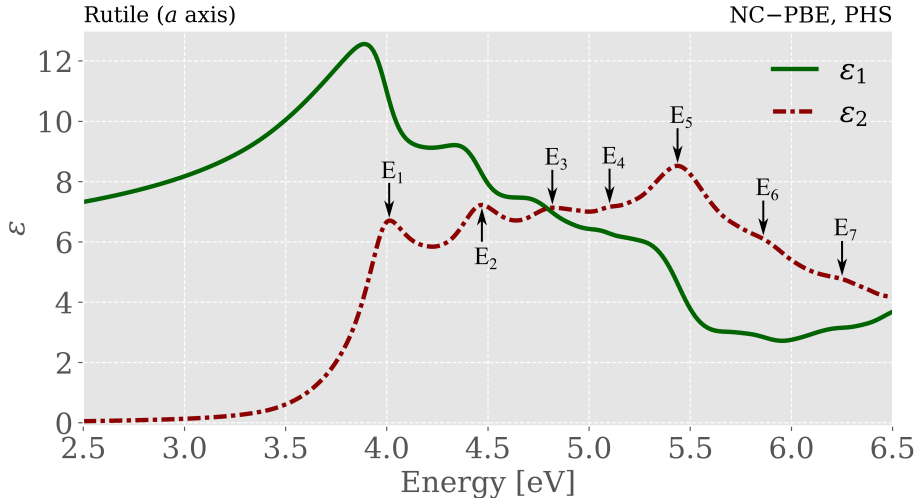

(a)

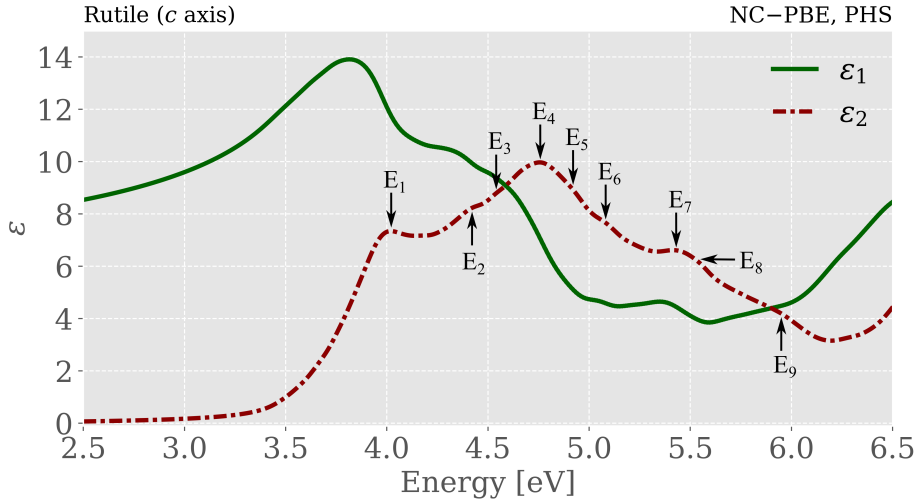

(b)

Figure 4.9: Dielectric function of rutile with critical points along the (a) ordinary and the (b) extraordinary axes. The spectra are computed according to the PHS method, with the NC pseudopotential and the PBE functional.

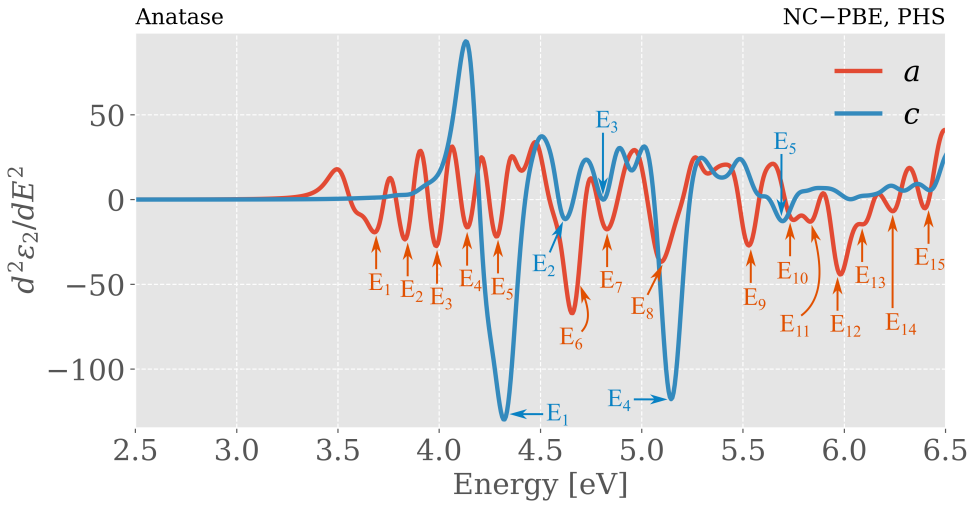

Figure 4.10: Second derivative of ε_2 for anatase.

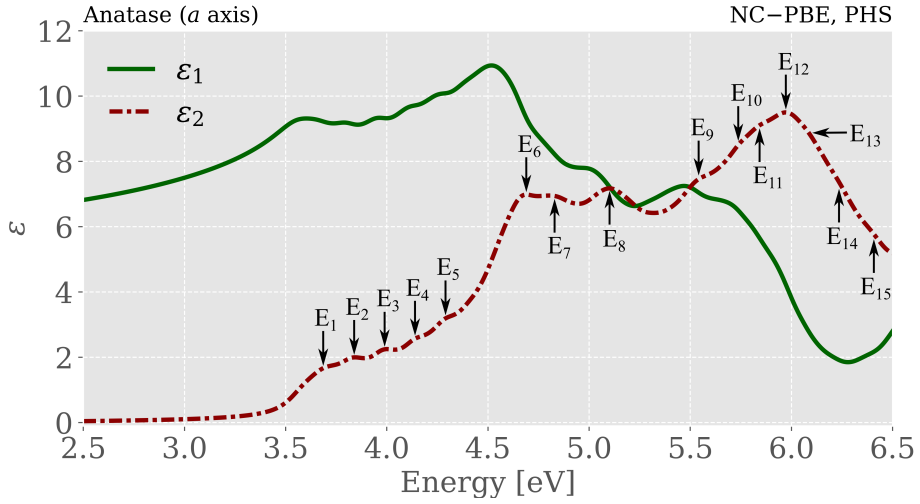

(a)

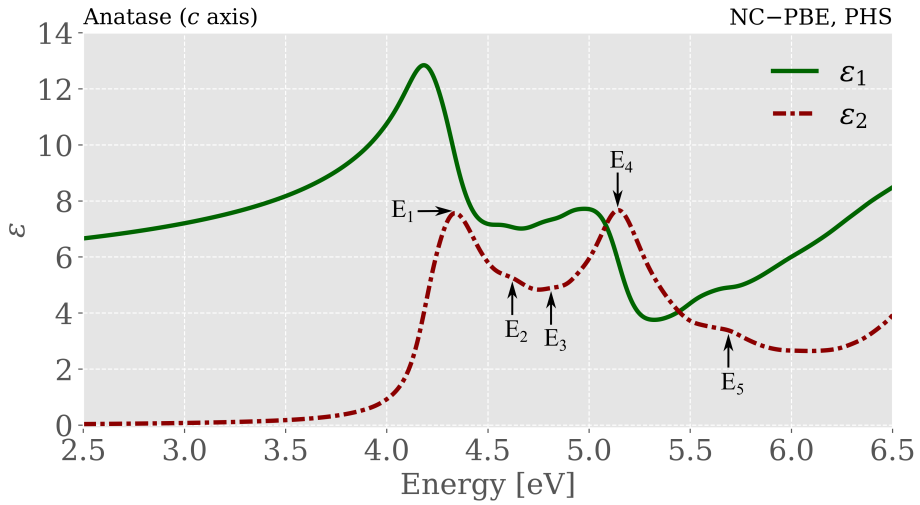

(b)

Figure 4.11: Dielectric function of anatase with critical points along the (a) ordinary and the (b) extraordinary axes. The spectra are computed according to the PHS method, with the NC pseudopotential and the PBE functional.

Table 4.2: Critical points of rutile and anatase, based on second derivative analysis of the imaginary relative dielectric function, along the direction of the ordinary (a) and the extraordinary (c) axes.

	Rutile		Anatase	
$E_{\#}$	E_a [eV]	E_c [eV]	E_a [eV]	E_c [eV]
E_1	4.01	4.02	3.69	4.34
E_2	4.47	4.42	3.84	4.62
E_3	4.82	4.54	3.99	4.81
E_4	5.10	4.76	4.14	5.14
E_5	5.44	4.92	4.29	5.69
E_6	5.86	5.08	4.69	-
E_7	6.25	5.43	4.83	-
E_8	-	5.54	5.10	-
E_9	-	5.95	5.54	-
E_{10}	-	-	5.74	-
E_{11}	-	-	5.84	-
E_{12}	-	-	5.97	-
E_{13}	-	-	6.09	-
E_{14}	-	-	6.24	-
E_{15}	-	-	6.41	-

not even the relatively large peak E_{4c} at 4.76 eV.

For anatase, CPs along the ordinary axis are reported 3.8 eV (shoulder) and 4.8 eV (large peak) by Jellison et al. and 3.8 eV (small peak), 4.7 eV (large peak), and 5.8 eV (small peak) by Hosaka et al. [71]. Not many parallels can be drawn between our 15 CPs and those documented by the literature. The structure reported at 3.8 eV may correspond to $E_{2a} = 3.84$ eV, which appears as a relatively small peak. The large peaks reported at 4.8 eV (Jellison et al.) and 4.7 eV (Hosaka et al.) may correlate to either $E_{6a} = 4.69$ eV or $E_{7a} = 4.83$ eV, or perhaps a broadened combination of the two. The latter is not unlikely, since Jellison et al.'s peak has a broad character (the energy range covered by Hosaka et al. is too expansive to judge broadness). Additionally, the global maximum $E_{12a} = 5.97$ eV, and surrounding shoulders, may correspond to the small peak at 5.8 eV of Hosaka et al.

Along the extraordinary axis, Jellison et al. report CPs at 4.3 eV (large peak) and 5.05 eV (shoulder), while Hosaka et al. at 4.4 eV (large peak) and 5.0 eV (shoulder). The first CP matches well with the peak $E_{1c} = 4.34$ eV, while the second peak, $E_{4c} = 5.14$ eV, may correspond to the documented shoulder at ~ 5 eV. The remaining shoulders are not identified by

Jellison et al. or Hosaka et al.

There are several possible causes for the notable discrepancy in the quantity of CPs between our DFT computations and empirical studies. For one, the finite k-space sampling can lead to discontinuities or irregularities in the resulting dielectric function if the grid is not sufficiently dense. We attempted to minimize this error source by performing a dense NSCF calculation using a $30 \times 30 \times 30$ k-point grid, but due to high computational cost, denser meshes were not tested. Secondly, approximations in DFT, like the use of exchange-correlation functionals and pseudopotentials, can introduce errors or anomalies compared to more exact methods.

Furthermore, experimental measurements of the dielectric function often involve some form of broadening due to various factors like instrumental resolution, temperature effects [72], and lifetime broadening [9, p. 318]. Lifetime broadening is a result of Heisenberg's uncertainty principle for energy and time [14, p. 142],

$$\Delta t \Delta E \geq \frac{\hbar}{2}.$$

Since an excited interband transition has a finite lifetime, there will necessarily be a broadening of the energy position. The combined broadening effects make experimental spectra appear smoother. In contrast, computational results do not inherently include these broadening effects, and so can appear more "spiky" unless some form of artificial broadening is applied. The *epsilon.x* program does, however, include a broadening parameter, of which an increased value might reduce the number of CPs and more closely match empirical data.

Discrepancies of the critical points from Table 4.2 compared to empirical literature may therefore be caused by limitations of experimental measurements or computational precision. Efforts to improve the accuracy of our GGA-based DFT approach could be made, for example utilizing a denser k-mesh, adjusting the interband broadening parameter, or consider hybrid functionals or many-body perturbation theory [73, p. 551].

4.4.2 Vertical Translation Analysis

The vertical translation analysis code identified 22 CPs for rutile and 39 CPs for anatase. Out of those, 8 (36%) for rutile and 11 (28%) for anatase matched with CPs from the second derivative analysis. The second derivative analysis grouped some CPs together during comparison, due to the CP match precision requirement of ±0.04 eV. As a result, 9 out of 16 (56%) of rutile's and 13 out of 20 (65%) of anatase's CPs from Table 4.2, aligned with CPs identified by our code.

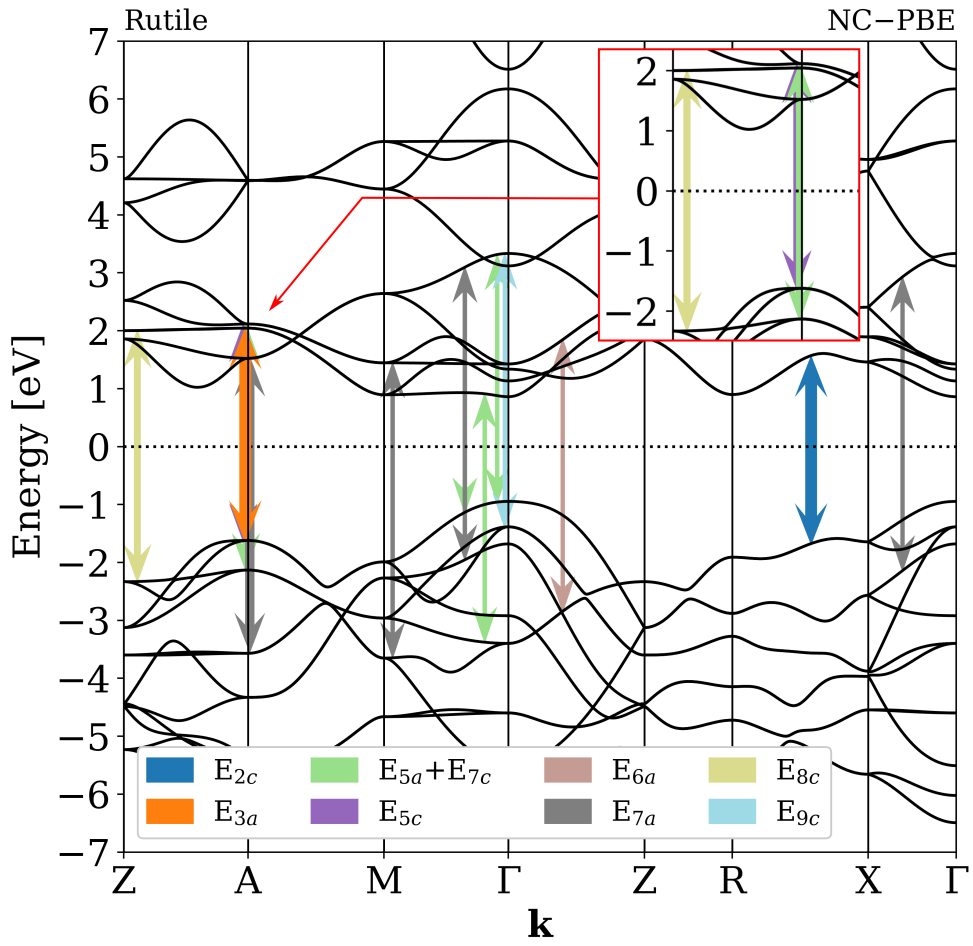

Figure 4.12: Optical transitions in k-space corresponding to rutile's CPs found by second derivative analysis, based on vertical translation analysis code. The arrows' thicknesses are proportional to the weight of their respective transitions, as explained in Sect. 3.5.2. The red outlined box more clearly shows the E_{5a}+E_{7c} and E_{5c} transitions at the A point.

A greater percentage of CPs from the second derivative analysis matched with CPs from the vertical translation analysis than vice versa. This is rather expected, since the latter method does not take the optical matrix elements into account.

Shown in Figs. 4.12 and 4.13 are the optical transitions found by the vertical translation analysis code, for the matching CPs. The arrows illustrate the interband transitions for each CP, with a thickness proportional to the weight of the transition, as discussed in Sect. 3.5.2.

Interestingly, there does not seem to be a one-to-one relation between the weight and the magnitude of ε_2 at the CPs. For instance, judging by

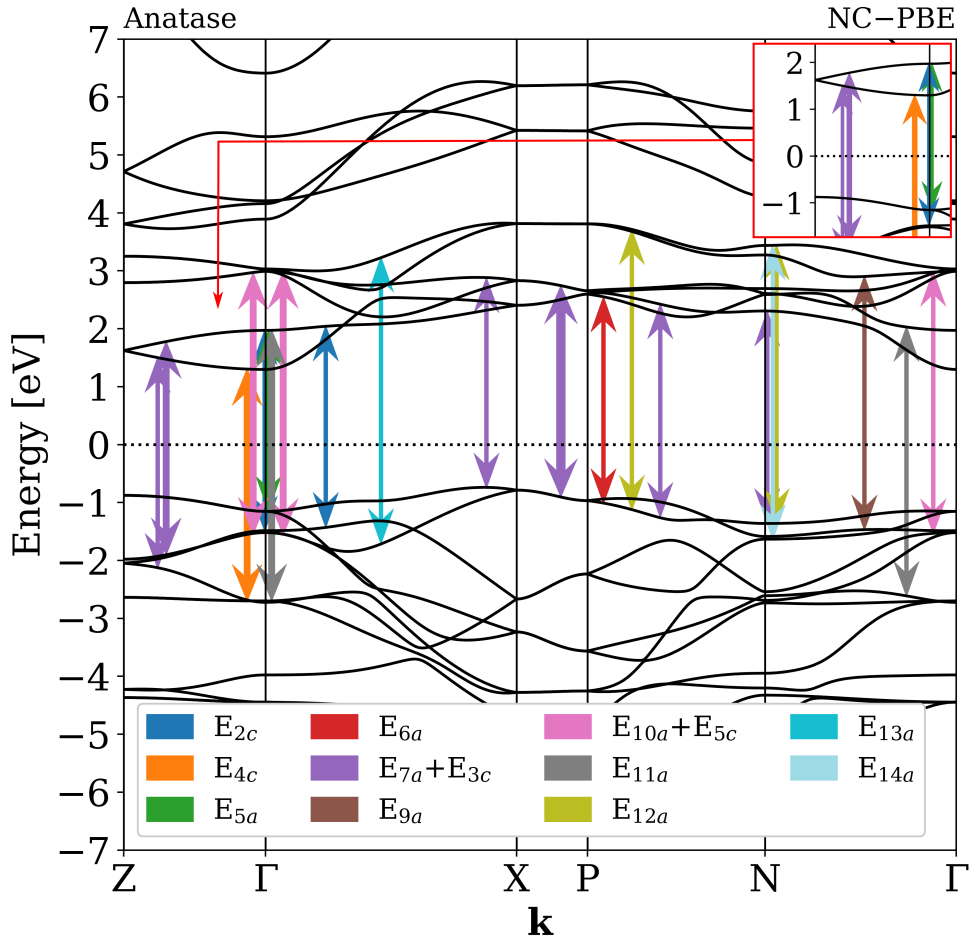

Figure 4.13: Optical transitions in *k*-space corresponding to anatase's CPs found by second derivative analysis, based on vertical translation analysis code. The arrows' thicknesses are proportional to the weight of their respective transitions, as explained in Sect. 3.5.2. The red outlined box more clearly shows the E_{2c} and E_{5a} transitions at the Γ point.

rutile's Fig. 4.12 alone, one might assume that E_{3a}, E_{5a}, E_{7a}, E_{2c}, E_{7c}, and potentially E_{8c}, would exhibit the highest amplitudes. Yet, some of the greatest maxima, such as E_{4c}, are absent. The reason behind this absence remains uncertain. It is possible that parameters *dEt* and *kinterval* were set too strictly, but our parameter testing indicated that loosening these requirements led to transitions at clearly non-parallel bands (too large *dEt*) or transitions with few state contributions (too low *kinterval*).

Rutile's E_{4c}, for example, the large amplitude may simply be a result of a large number of transitions at different points in the BZ with significant transition probabilities. To illustrate this, we have plotted all the optical

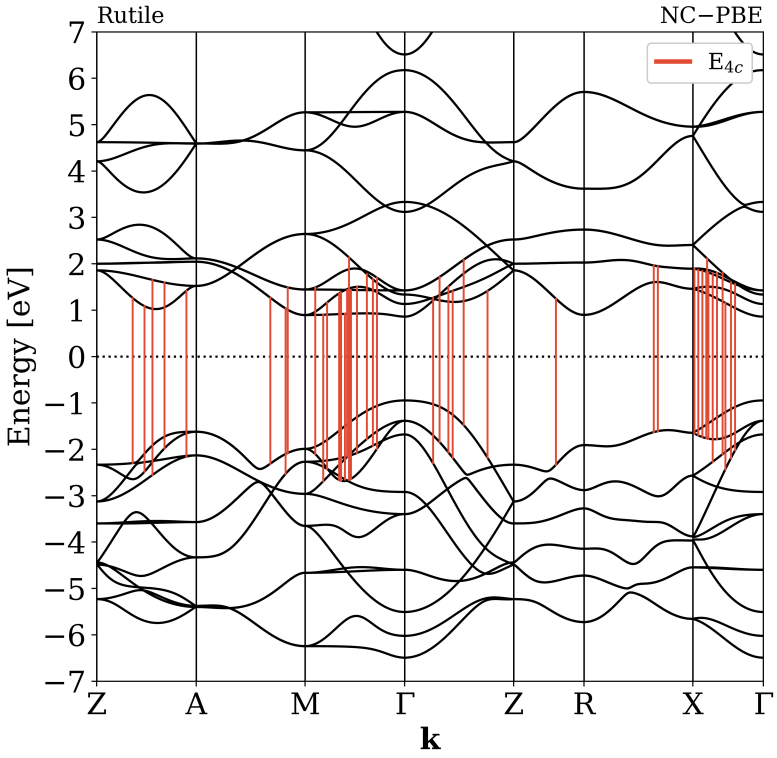

(a)

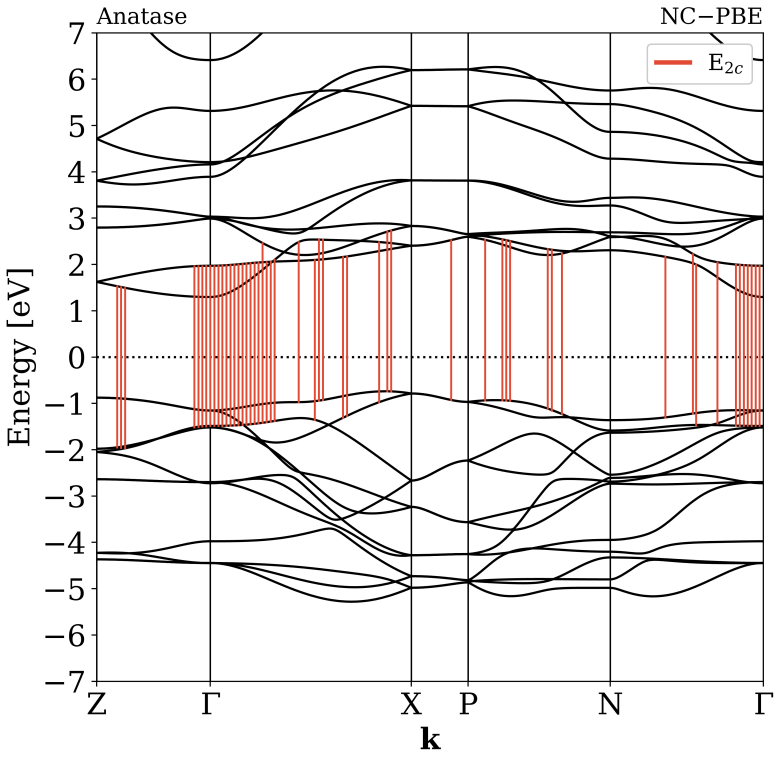

(b)

Figure 4.14: Band structures of (a) rutile and (b) anatase showing all possible optical transitions corresponding to a critical point within an interval of ±0.02 eV.

transitions in the band structure with energies equal to E_{4c}, within ±0.02 eV, in Fig. 4.14a.

Similarly, for the CPs exhibiting vertical translation, there may also be contributions to ε_2 at other points in the BZ. Fig. 4.14b illustrates that while the majority of the contributions occur at the point of vertical translation, near the Γ point, there exist other potential transitions.

It is worth noting that the vertical translation code only considers direct interband transitions. Despite indirect transitions being greatly outnumbered by direct ones, their contributions can be observed in the dielectric function at points below the direct band gap [9, p. 265]. However, they generally do not result in CPs due to their relatively small impact. Furthermore, since the *epsilon.x* program excludes indirect transitions from its calculations [74], the influence of any potential indirect transition CP can be discounted in our CP comparison.

To the best of our knowledge, no prior studies have isolated the transitions in *k*-space responsible for the critical points exhibited by rutile and anatase. Hence, the reliability of our vertical translation analysis method remains unconfirmed. The fact that our method identified a notable portion of the CPs for rutile (56%) and anatase (65%) does suggest some degree of validity. However, the remaining unidentified CPs, and more importantly, the exclusion of transition probabilities, greatly undermines the reliability of our findings. Applying our method to crystal structures with more established literature concerning interband transitions contributing to ε_2 CPs could help assess its accuracy.

4.5 DFT+U

The projected density of states is shown in Fig. 4.16 for rutile and in Fig. 4.17 for anatase. Both figures suggest that the oxygen p orbitals dominate at the valence band edge, while the titanium d orbitals dominate at the conduction band edge, for both polymorphs. Considering that the electronic configuration of oxygen is $1s^2 2s^2 2p^4$ and $1s^2 2s^2 2p^6 3s^2 3p^6 4s^2 3d^2$ for titanium [75, p. 355], we applied the Hubbard parameter to the O 2p and the Ti 3d orbitals, in order to increase the band gap. Our projected DOS results agree with the literature, in that the valence band is primarily composed of O 2p orbitals and the conduction band of Ti 3d orbitals [1, p. 68].

The band gaps as a function of the U parameter are plotted in Figs. 4.15a for rutile and 4.15b for anatase. The graphs show nearly linear response of an increased U parameter. Band gaps equal to the experimental values, with a precision of two decimal points, were achieved with $U = 4.98$ eV for rutile and $U = 3.86$ eV for anatase.

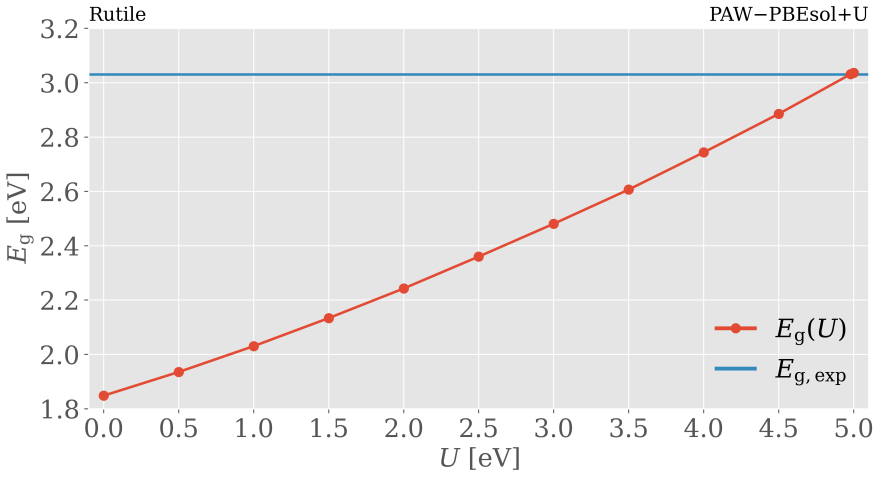

(a)

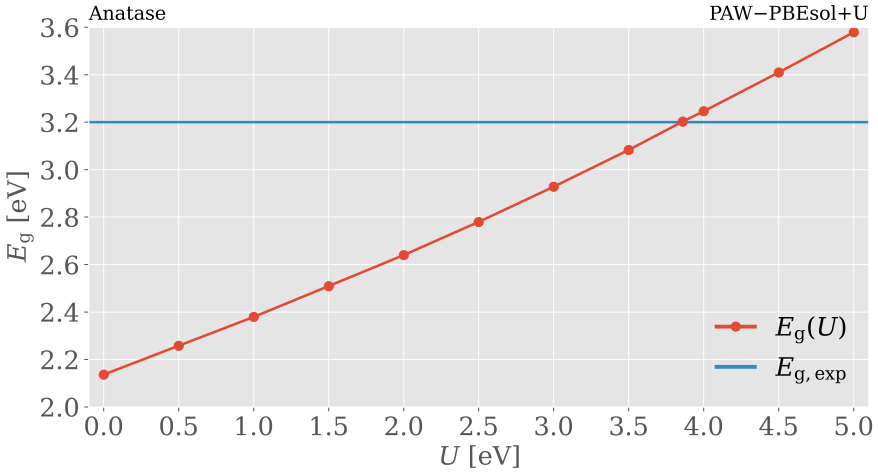

(b)

Figure 4.15: Band gaps of (a) rutile and (b) anatase as a function of the Hubbard U parameter, calculated with the PBEsol+U method and the PAW pseudopotential.

The density of states compared to a standard PBEsol calculation are shown in Fig. 4.18a for rutile and 4.18b for anatase. As designed, the band gaps of the PBEsol+U calculations are greater than the PBEsol calculations. Both the valence band edge and the conduction band edge are pushed further away from the Fermi level, but the conduction band edge more so for rutile. Interestingly, the PBEsol DOS are more spread out along the energy axis.

Although appearing at different energies, the featured structures of both methods are mostly equivalent. The main anomalies with PBEsol+U

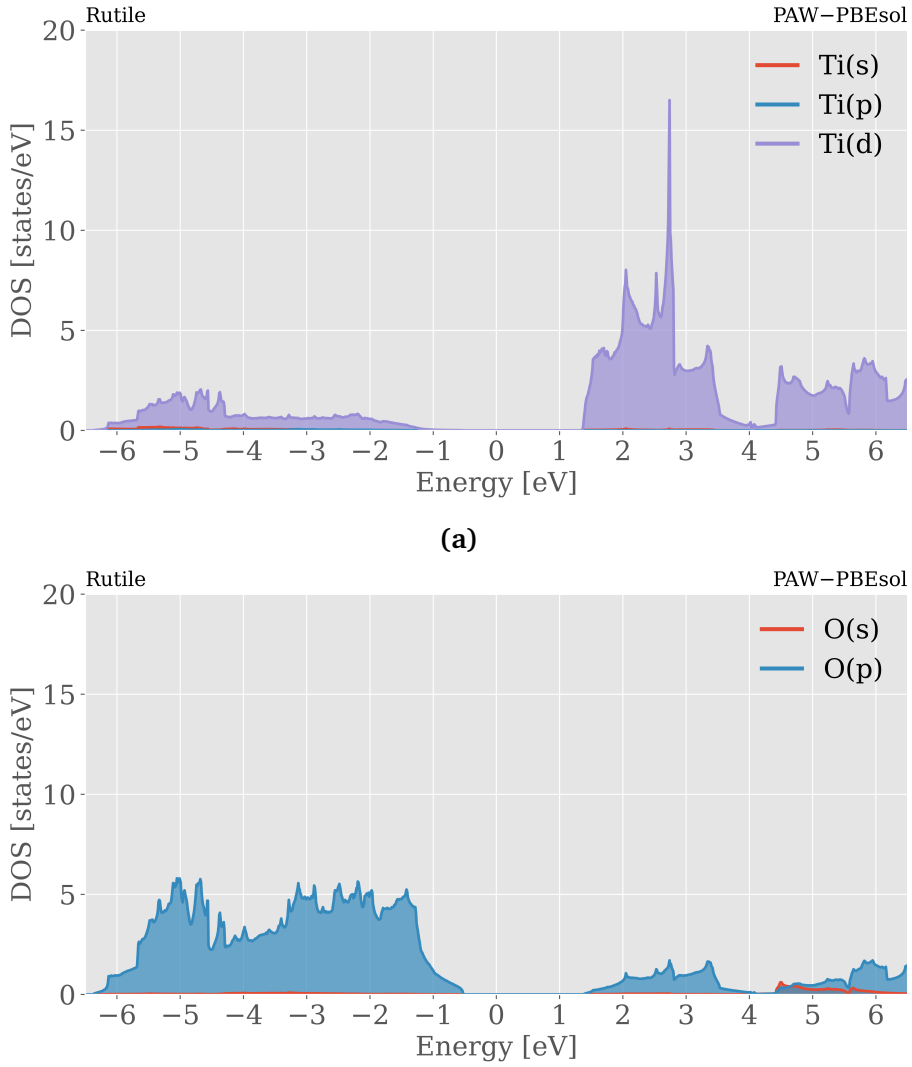

Figure 4.16: Projected DOS of rutile. The O 2p orbital dominates the VB, while the Ti 3d orbital dominates the CB.

are the occasional spikes not seen in the PBEsol spectra, such as anatase's spike at ~ -3.8 eV.

The band diagrams obtained using the PBEsol+U method, as illustrated in Figs. 4.19a and 4.19b, unsurprisingly bear a strong resemblance to the structures depicted in Figs. 4.2a and 4.2b, with the exception of an expanded band gap.

Interestingly, the direct band gap of rutile transforms into an indirect one, transitioning from the Γ to the M point. This shift is attributed to

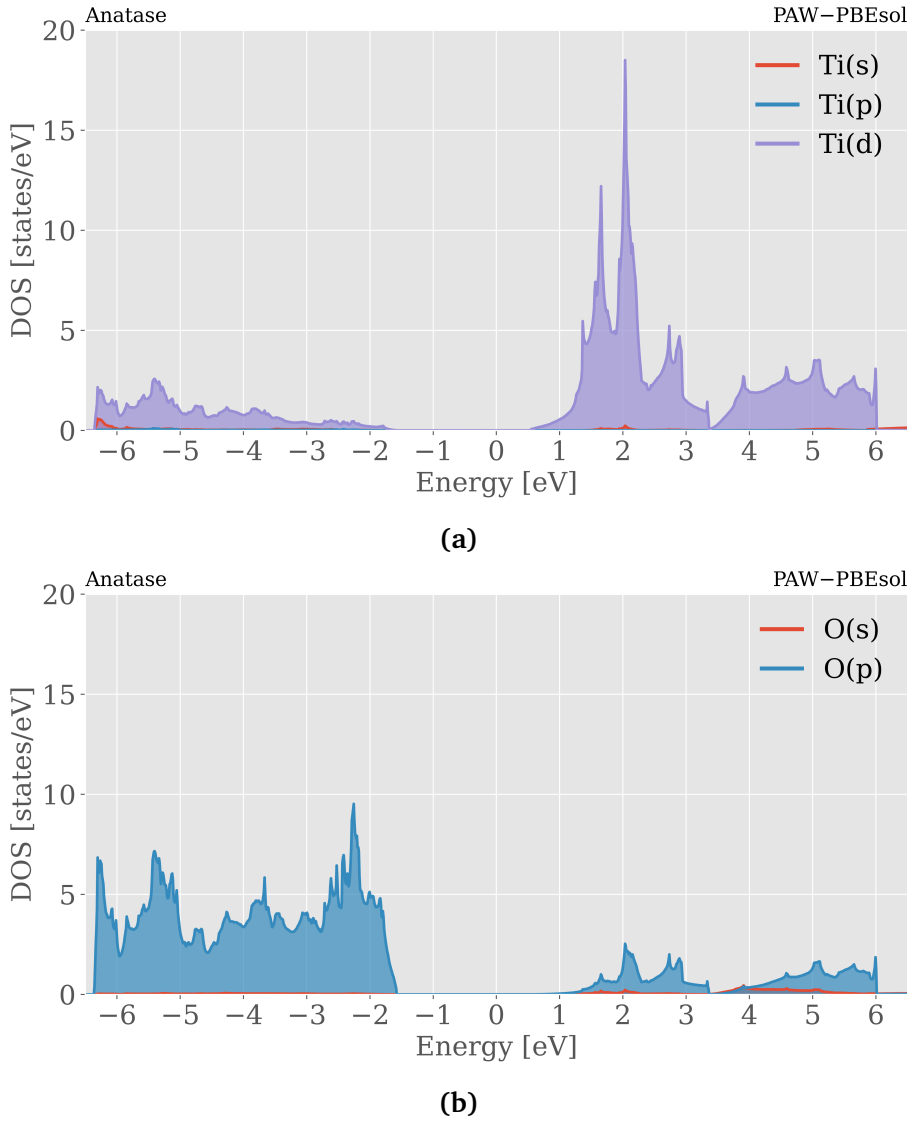

Figure 4.17: Projected density of states of anatase. The O 2p orbital dominates the valence band, while the Ti 3d orbital dominates the conduction band.

subtle modifications in the electronic structure. Minor changes in the electronic structure have caused this shift, as the conduction band minimum at the M and the Γ points are nearly identical for both methods. A band structure calculation using the PBEsol functional confirmed that it was indeed the U parameter that incited this change, and not the switch from the NC–PBE to the PAW–PBEsol file.

Comparing Fig. 4.19 to Fig. 4.2 reveals that certain bands have split at the symmetry points, for example at the A point ($E \approx -6.5$ eV) for rutile

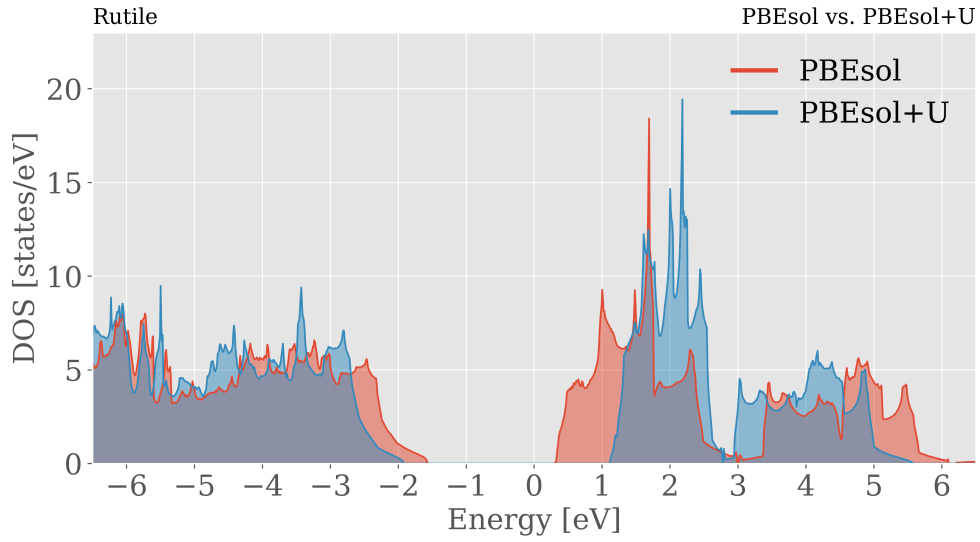

(a)

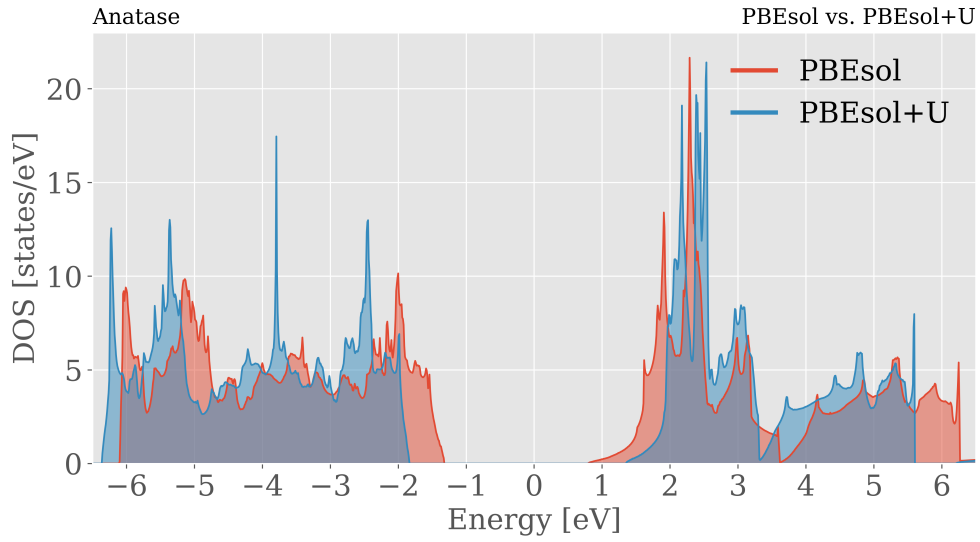

(b)

Figure 4.18: The DOS of (a) rutile and (b) anatase, computed with the PAW pseudopotential and the PBEsol functional, both with and without the DFT+U method. The Fermi energy is at $E = 0$ eV.

or the Γ point ($E \approx -2.5$ eV) for anatase. Thus, there is reason to believe that the DFT+U method has some limitations in accurately representing the band structure.

It is also important to acknowledge the semi-empirical nature of this approach. Determining Hubbard parameters that accurately replicate the experimental band gaps of rutile and anatase does not necessarily

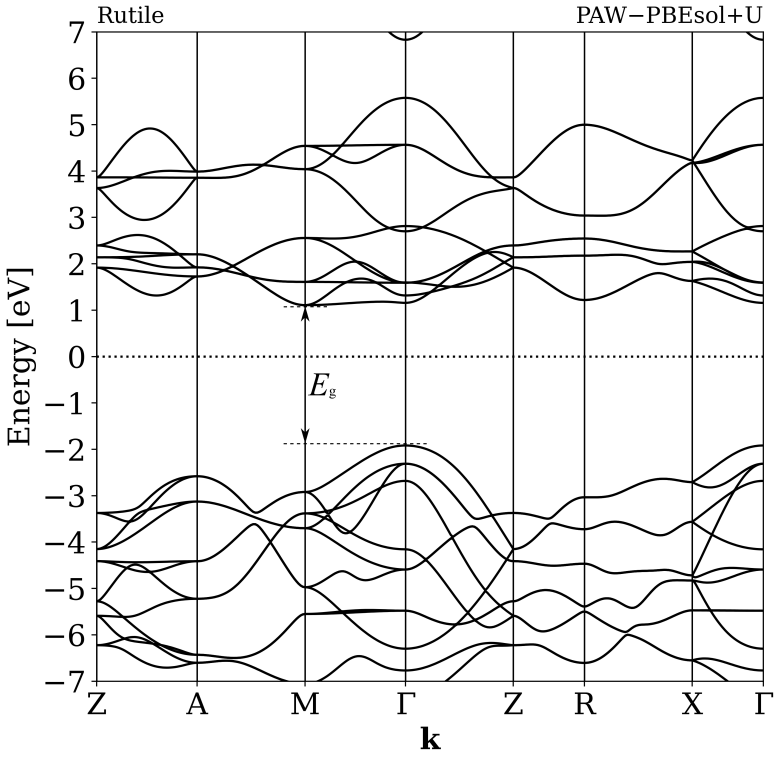

(a)

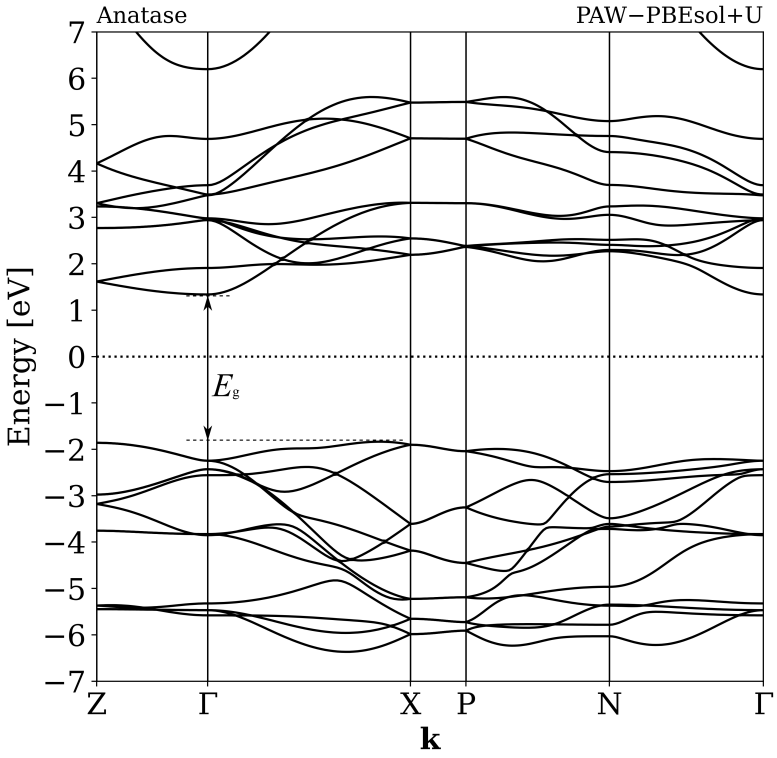

(b)

Figure 4.19: Band structure of (a) rutile and (b) anatase, computed with the NC pseudopotential and the PBEsol+U method, with the Fermi energy set to $E = 0$ eV.

guarantee their suitability for other modified versions of TiO_2. Therefore, one should be careful when applying these parameters to structures with no available empirical data.

4.6 Modified TiO_2 Configurations

Due to technical issues with the *epsilon.x* program, resulting in infinitely large ε_2 values, we were only able to compute the dielectric function for the 25% CrN doped rutile and anatase.

4.6.1 Rutile, 50% CrN

Figs. 4.20a and 4.20b suggest that 50% CrN doped rutile has metallic properties. The Fermi energy is not located in a band gap, with plenty of states below and above E_F, allowing free flow of electrons. This leaves the structure unsuited as a primary material for an IBSC, or any other solar cell.

4.6.2 Rutile, 25% CrN

The 25% CrN doped rutile, on the other hand, has its Fermi energy located inside an intermediate band between a valence and a conduction band, as illustrated in Figs. 4.21a and 4.21b. The intermediate band has a relatively large number of states, thereby providing many potential states for electrons from the VB to transition into, and for further transitions into the CB.

Considering rutile's wide band gap, it is expected that the metal chromium would be responsible for states within the gap, although nitrogen cannot be ruled out. Therefore, we calculated the projected density of states, plotted in Fig. 4.22, which suggests that the IB is mainly composed of Cr 3d orbitals. Similar to rutile, the valence band is dominated by O 2p orbitals, while the conduction band is dominated by Ti 3d orbitals, although the Cr 3d orbitals are significant at the CB edge.

The band gap of the compound is an estimated 1.17 eV, which comprises approximately 62% of the band gap computed for rutile. The IB has a width ΔE_{IB} of 0.50 eV, constituting a relatively large portion of the band gap (43%). According to Levy and Honsberg [45], as highlighted in Sect. 2.19, this IB width is well-suited for IBSCs. However, the two smaller band gaps – $E_{C,I}$ at 0.23 eV and $E_{I,V}$ at 0.45 eV – may be suboptimal as they are approximately one-third of the ideal values for achieving optimal efficiency, as proposed by Levy and Honsberg.

The dielectric function and absorption coefficient, shown in Figs. 4.23 and 4.24, illustrate the increased absorption of photons compared to pure rutile, especially for energies below rutile's band gap. The initial incline of ε_2, reaching an early peak at ~ 0.65 eV, indicates excitation of electrons from the VB to the IB and from the IB to the CB. ε_2 then experiences a decline until the energy exceeds the material's main band gap, when it again increases, as electrons can transition straight from the VB to the CB. This pattern is mirrored in the absorption spectrum, but might be more visible on a logarithmic scale. Compared to rutile (Fig. 4.5) this doped version exhibits significantly higher absorption for all energies, at least up to 6.5 eV.

4.6.3 Rutile, 12.5% CrN

Having successfully opened an intermediate band with 25% CrN-doped rutile, we wanted to investigate a further reduction in doping percentage. Figs. 4.25a and 4.25b reveal that a 12.5% configuration also produces such an electronic structure. As with the 25% CrN structure, there is a lone band within the band gap responsible for the intermediate states, as can be seen in Fig. 4.25b. Compared to Fig. 4.21b, this band structure exhibits a denser set of bands, primarily due to the larger supercell, which results in an increased number of atomic states in the unit cell.

The DOS spectrum exhibits striking similarities with the configuration doped by 25%, leading to the inference that the Cr 3d orbitals are the primary contributors to the formation of the intermediate band. This is confirmed by the projected density of states, as depicted in Fig. 4.26. The most prominent difference between the intermediate bands of the two configurations lies in the relatively reduced states in the IB of the 12.5% doped configuration, compared to the unit cell size. This is a logical result of the halved percentage of chromium which is principally accountable for the IB states.

The 12.5% CrN configuration of rutile has a band gap of 1.37 eV, which is 72% of pure rutile. The intermediate bandwidth is 0.41 eV, while the two sub-band gaps are $E_{\mathrm{C,I}} = 0.34$ eV and $E_{\mathrm{I,V}} = 0.62$ eV. Compared to 25% doped rutile, there is a slight increase in the band gap and the two sub-band gap energies, and a slight decrease in the IB width. Thus, according to Levy and Honsberg's calculations, these electronic properties may lead to a more efficient IBSC, despite $E_{\mathrm{C,I}}$ and $E_{\mathrm{I,V}}$ being only about half of the optimal sub-band gap values.

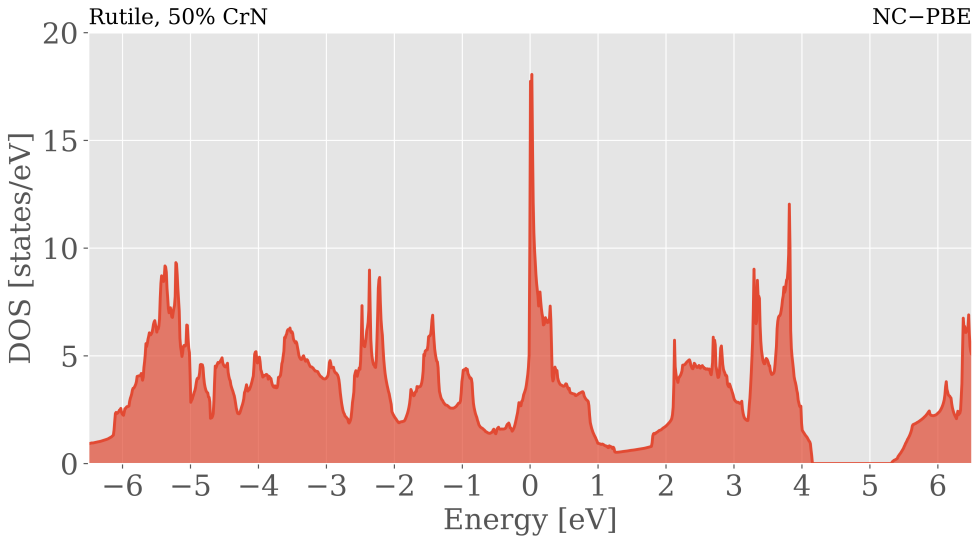

(a)

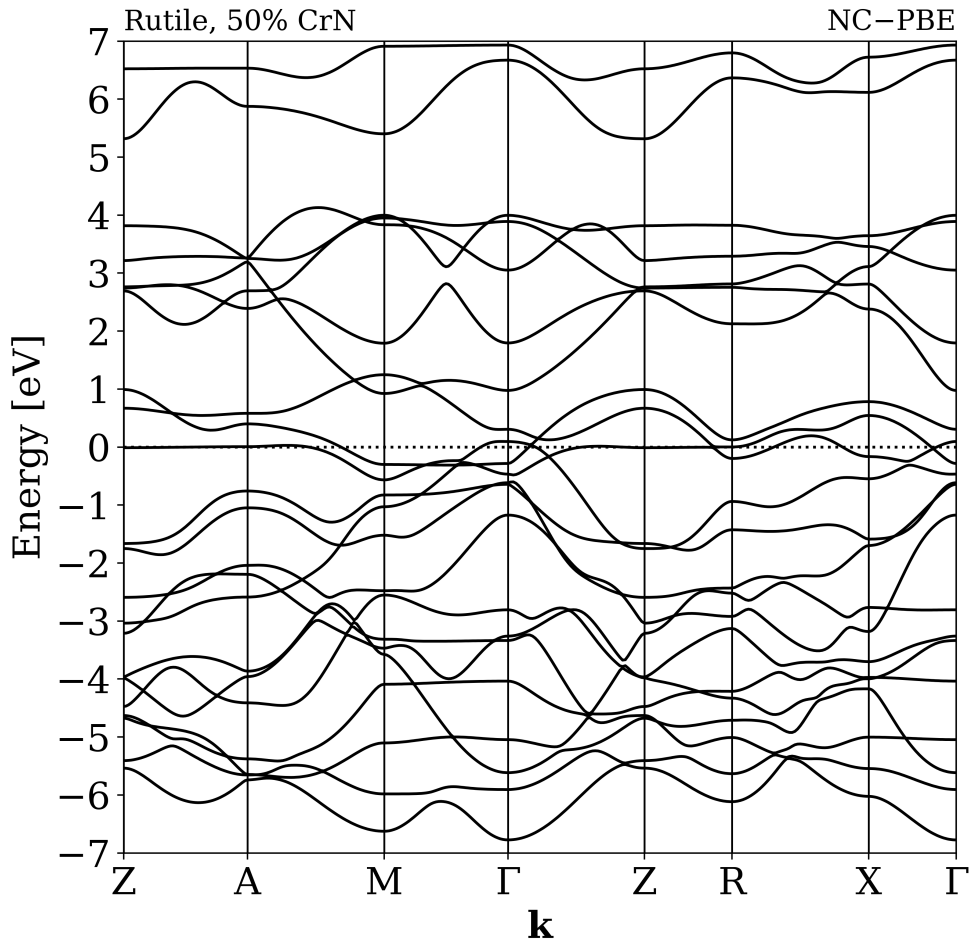

(b)

Figure 4.20: The (a) DOS and the (b) band structure of rutile doped with 50% CrN, computed with the NC pseudopotential and the PBE functional, with the Fermi energy set to $E = 0$ eV.

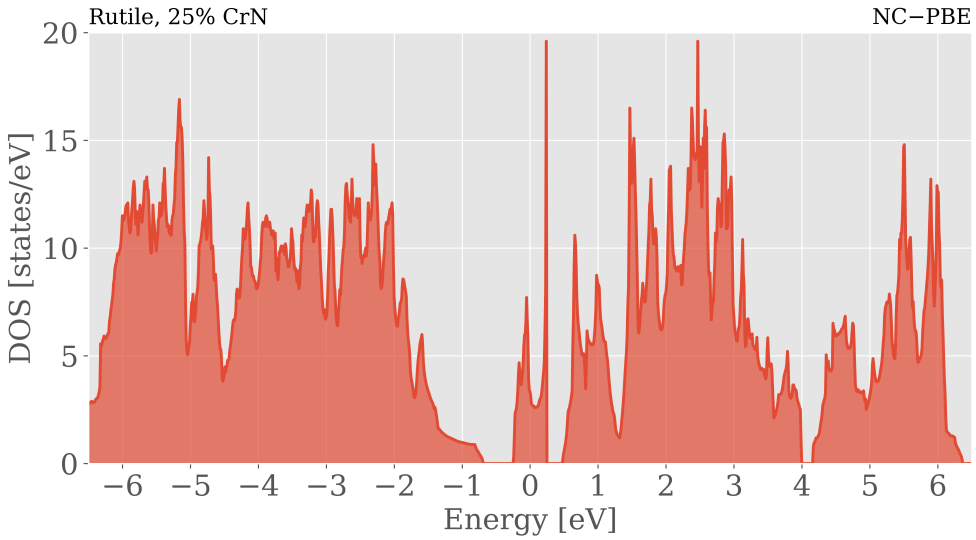

(a)

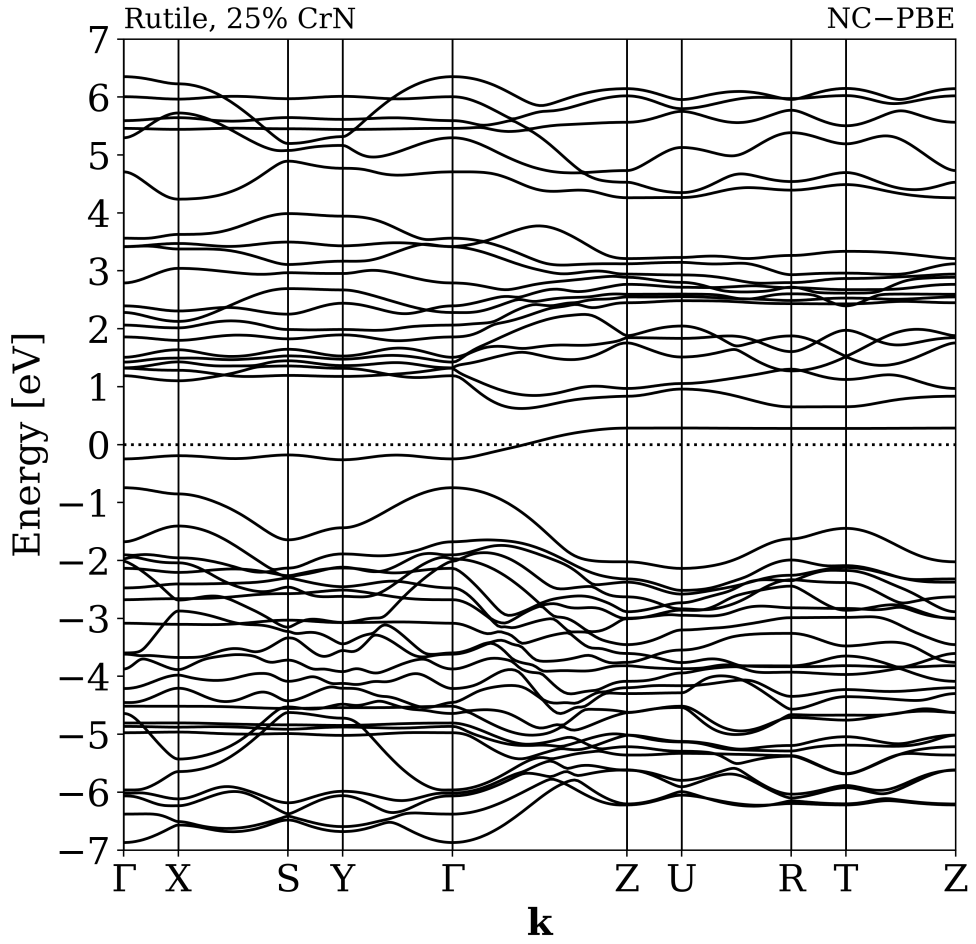

(b)

Figure 4.21: The (a) DOS and the (b) band structure of rutile doped with 25% CrN, computed with the NC pseudopotential and the PBE functional, with the Fermi energy set to $E = 0$ eV.

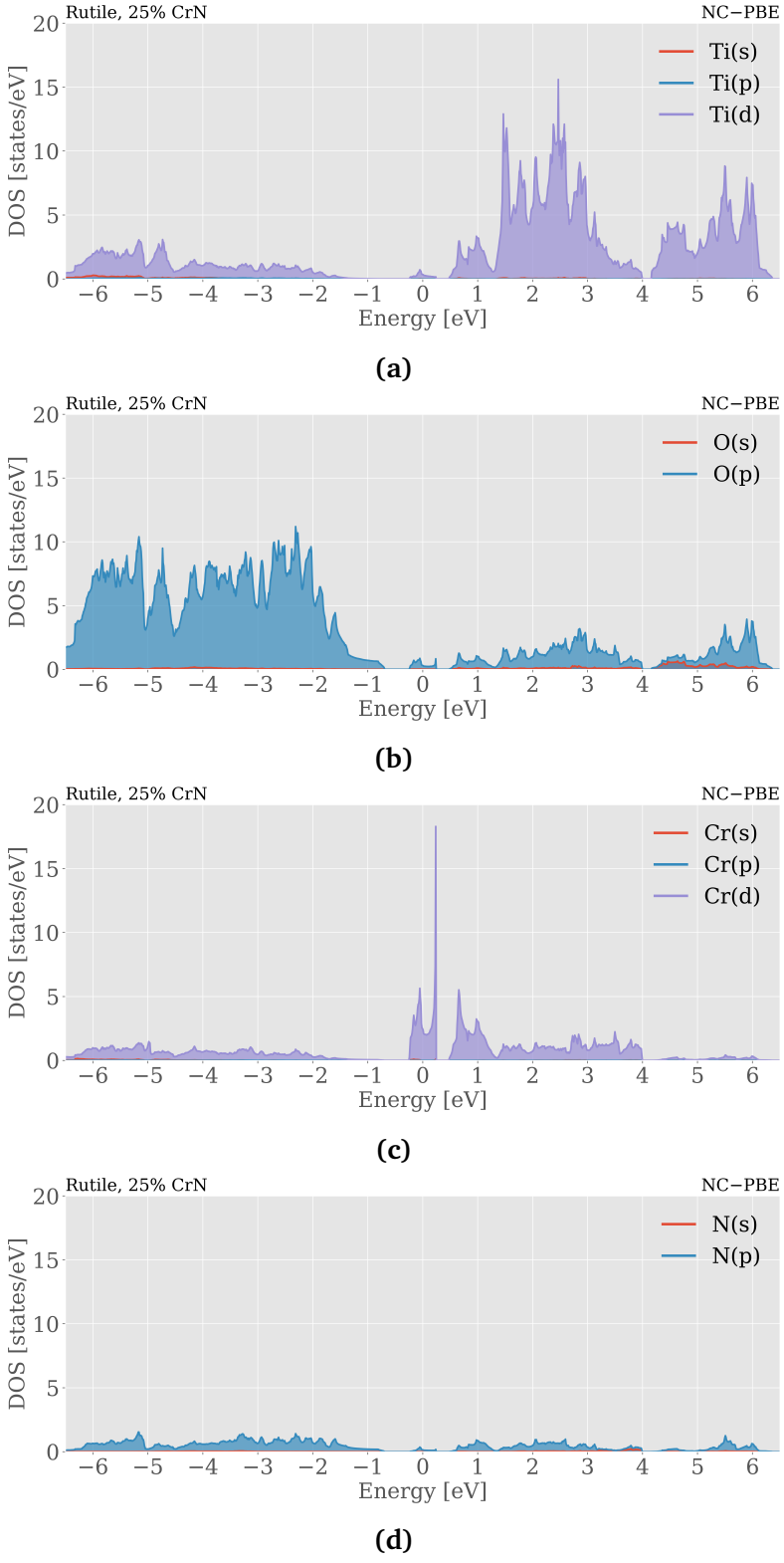

Figure 4.22: Projected DOS of rutile doped with 25% CrN. The O 2p orbital dominates the VB, the Cr 3d orbitals dominate the IB, while the Ti 3d and the Cr 3d orbitals dominate the CB.

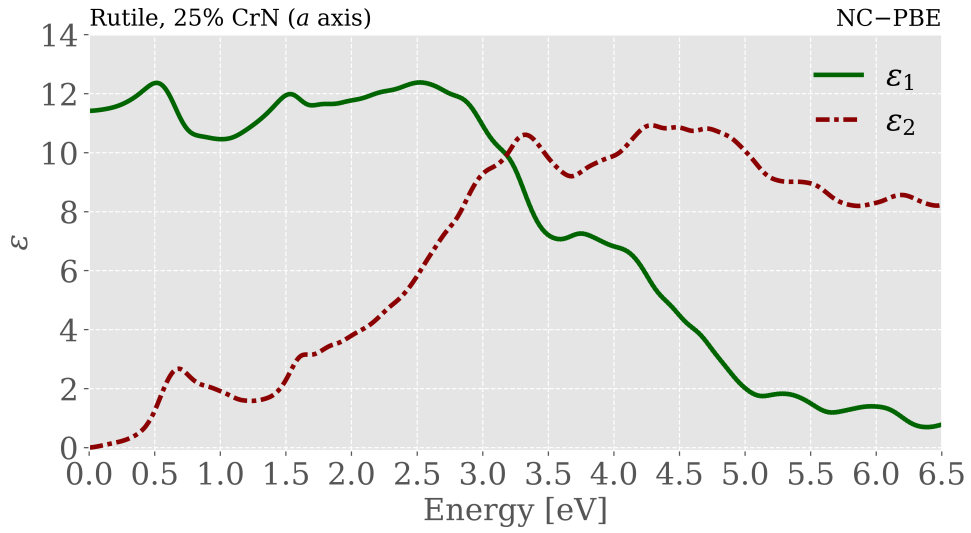

(a)

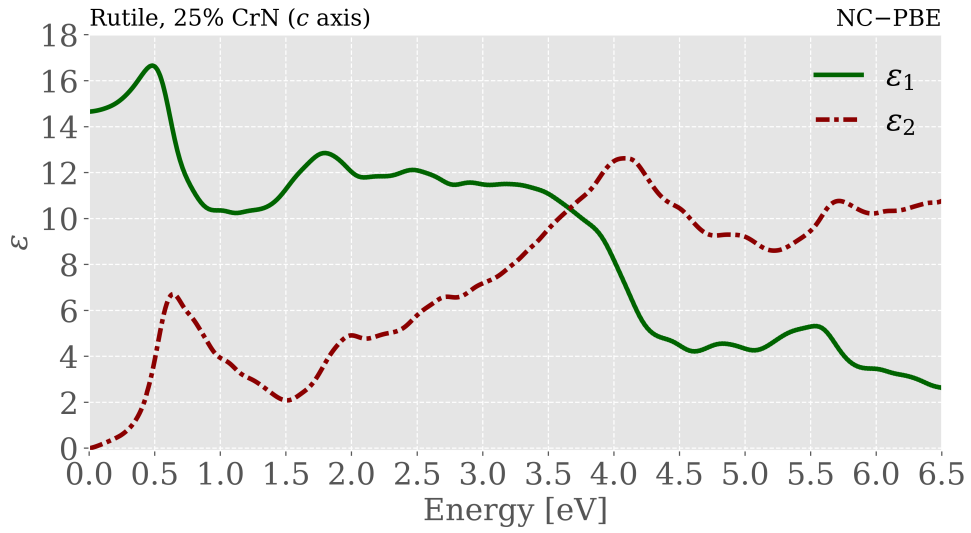

(b)

Figure 4.23: Dielectric function of rutile doped with 25% CrN, along the (a) ordinary and the (b) extraordinary axes. The spectra are computed with the NC pseudopotential and the PBE functional.

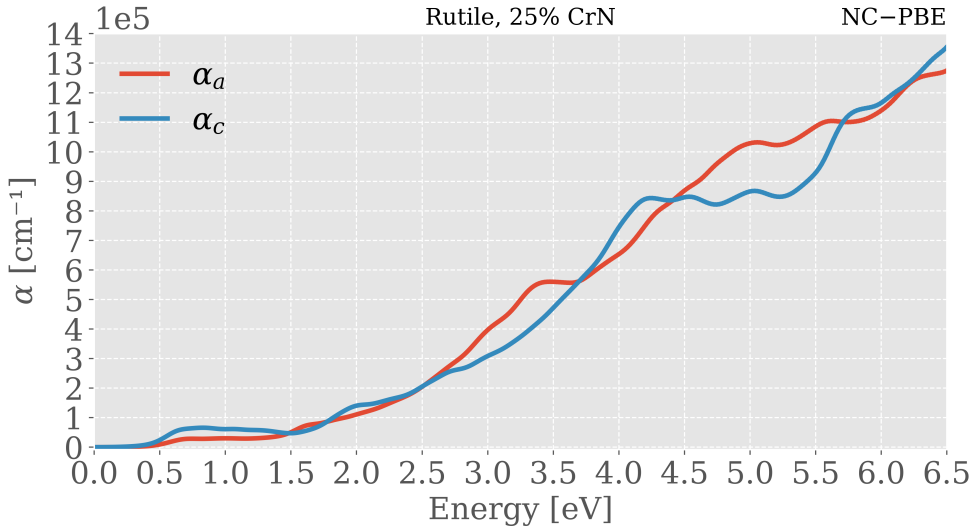

(a)

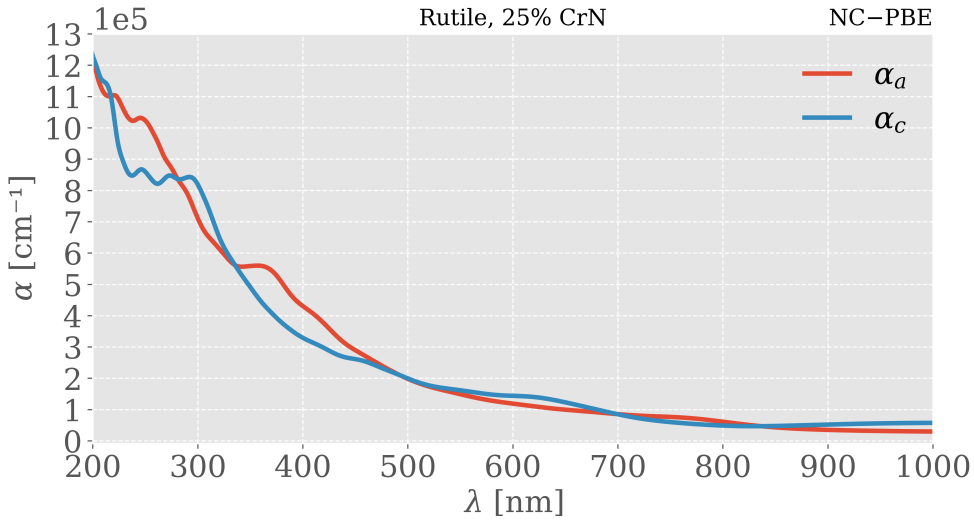

(b)

Figure 4.24: Absorption coefficient of rutile doped with 25% CrN, as a function of (a) photon energy and (b) photon wavelength. The spectra are computed with the NC pseudopotential and the PBE functional.

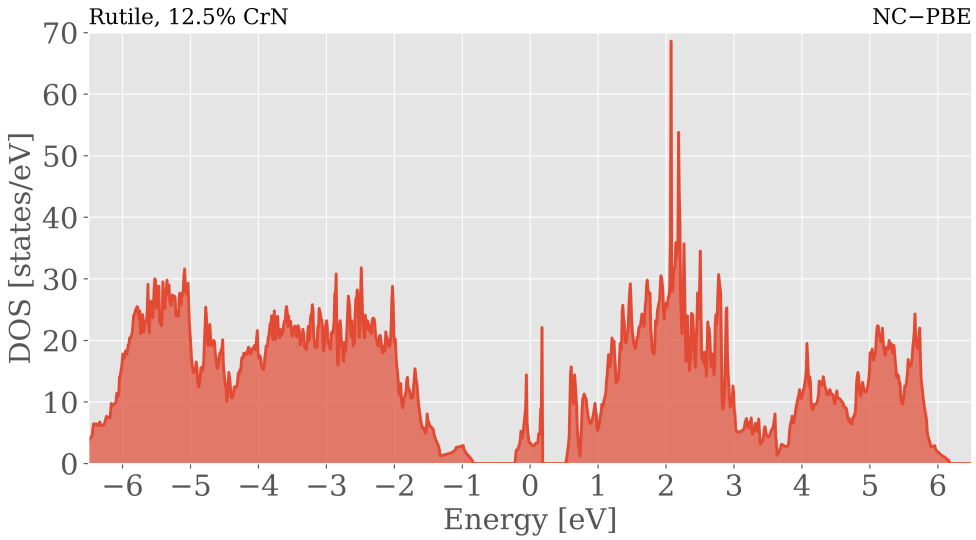

(a)

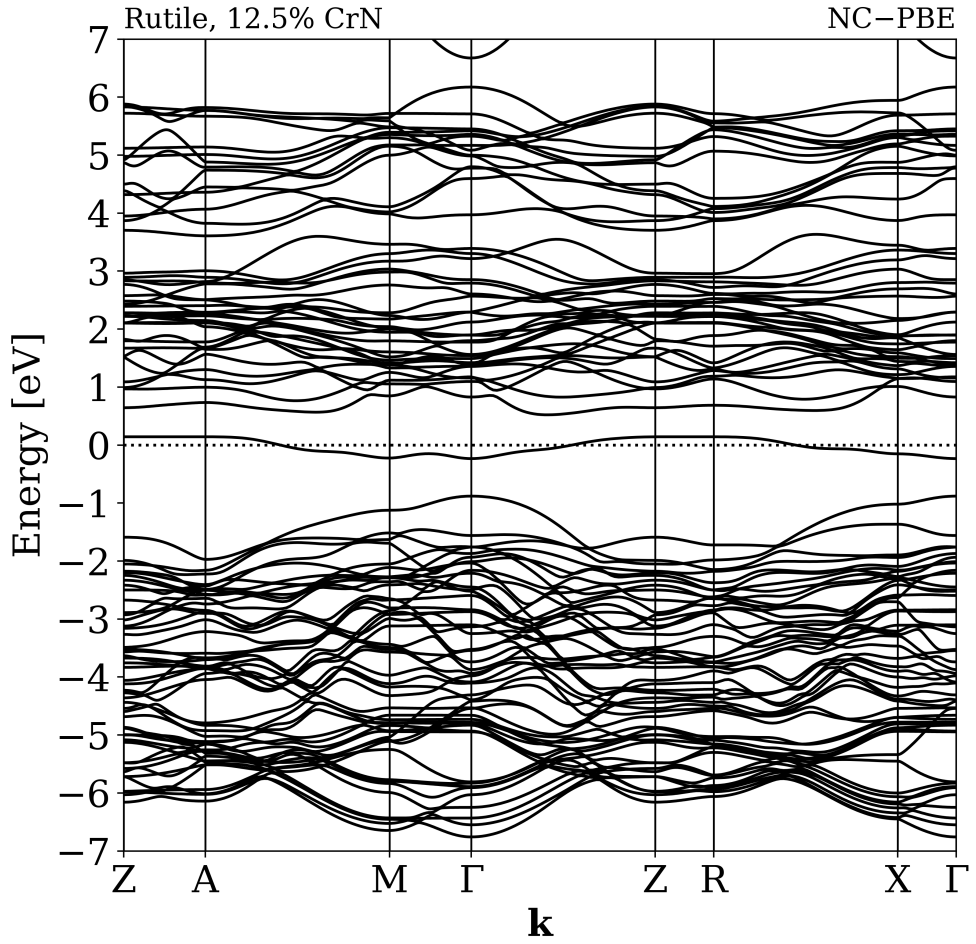

(b)

Figure 4.25: The (a) DOS and the (b) band structure of rutile doped with 12.5% CrN, computed with the NC pseudopotential and the PBE functional, with the Fermi energy set to $E = 0$ eV.

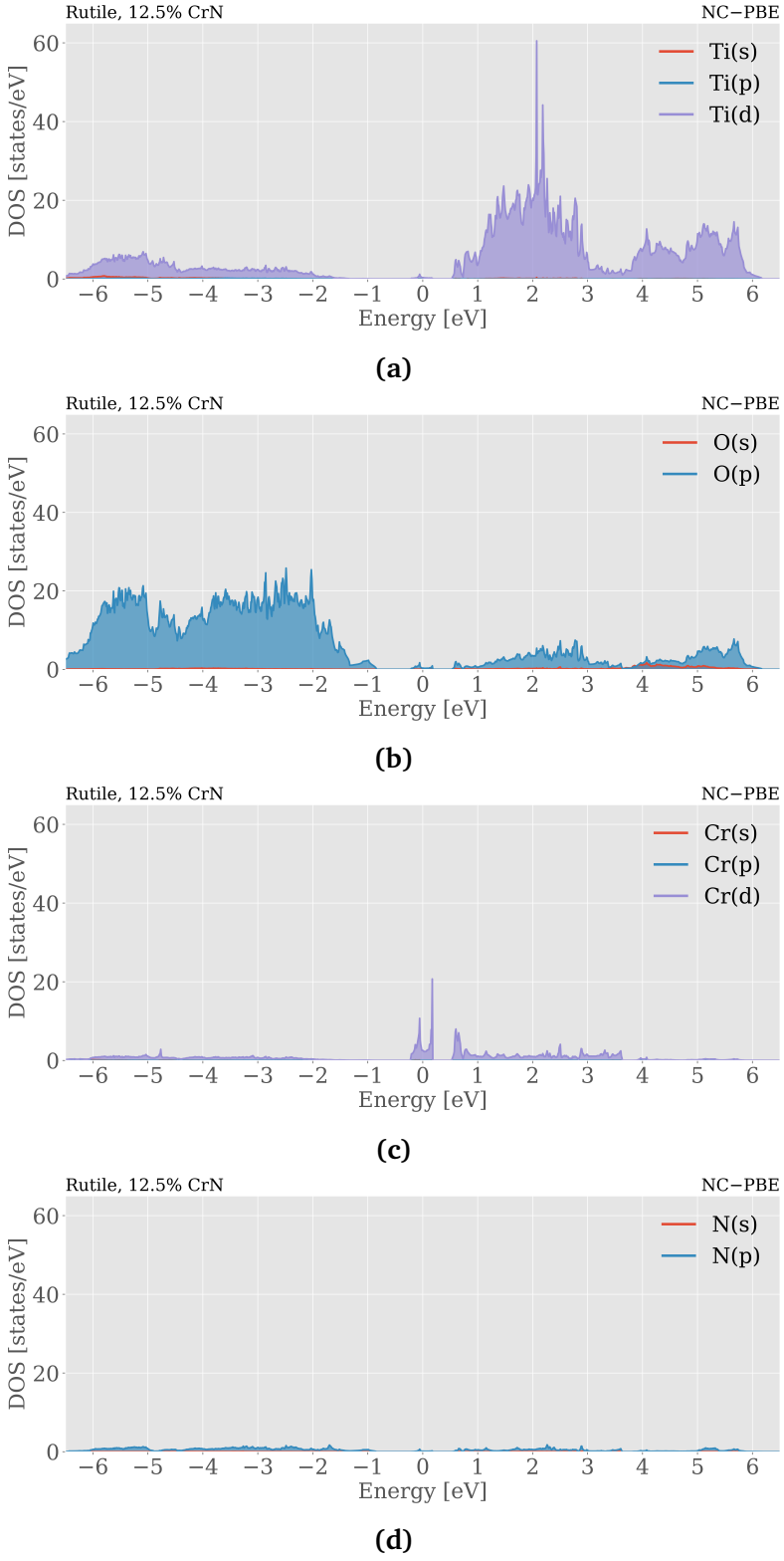

Figure 4.26: Projected DOS of rutile doped with 12.5% CrN. The O 2p orbital dominates the VB, the Cr 3d orbitals dominate the IB, while the Ti 3d and the Cr 3d orbitals dominate the CB.

4.6.4 Rutile, 25% Mo

Molybdenum was also evaluated as a potential dopant for rutile, specifically at a concentration of 25%, given the success of this proportion with co-doped rutile involving chromium and nitrogen. Figs. 4.27a and 4.27b depict the DOS and band diagram of this structure, respectively. Despite the presence of a gap approximately 1 eV below the Fermi energy and the existence of a relatively scant number of states directly beneath the Fermi energy, the structure appears metallic. For this reason, a thorough examination of lower molybdenum doping percentages could be worthwhile to determine whether an intermediate band might manifest.

4.6.5 Anatase, 50% CrN

Figs. 4.28a and 4.28b depict the Fermi level positioned within an electron band, indicating metallic properties, and thus not relevant as an IB material. The vanishing DOS at ~ 1.3 eV and the near zero DOS at ~ -0.7 eV may suggest the potential for an intermediate band opening up at lower CrN concentrations, aiming to minimize the number of states within the natural band gap of anatase.

4.6.6 Anatase, 25% CrN

Unlike in the case of rutile, a 25% CrN doping of anatase does not result in the formation of an intermediate band, as illustrated in Figs. 4.29a and 4.29b. However, one can observe from Fig. 4.29b that the Fermi energy intersects only a single detached band. It could therefore be of interest in future studies to examine even lower doping percentages to investigate whether this band further separates from the others, potentially leading to the creation of an IB.

The dielectric function and the absorption coefficient, presented respectively in Figs. 4.30 and 4.31, affirm its metallic nature, absorbing photons of all energies. Interestingly, the absorption coefficient along the extraordinary axis is up to four times greater than that along the ordinary axis for energies above 4 eV.

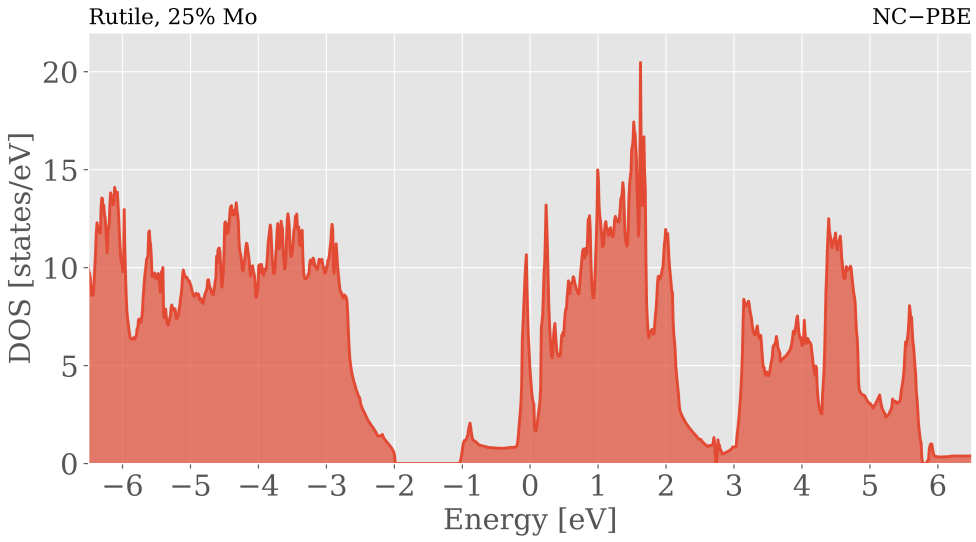

(a)

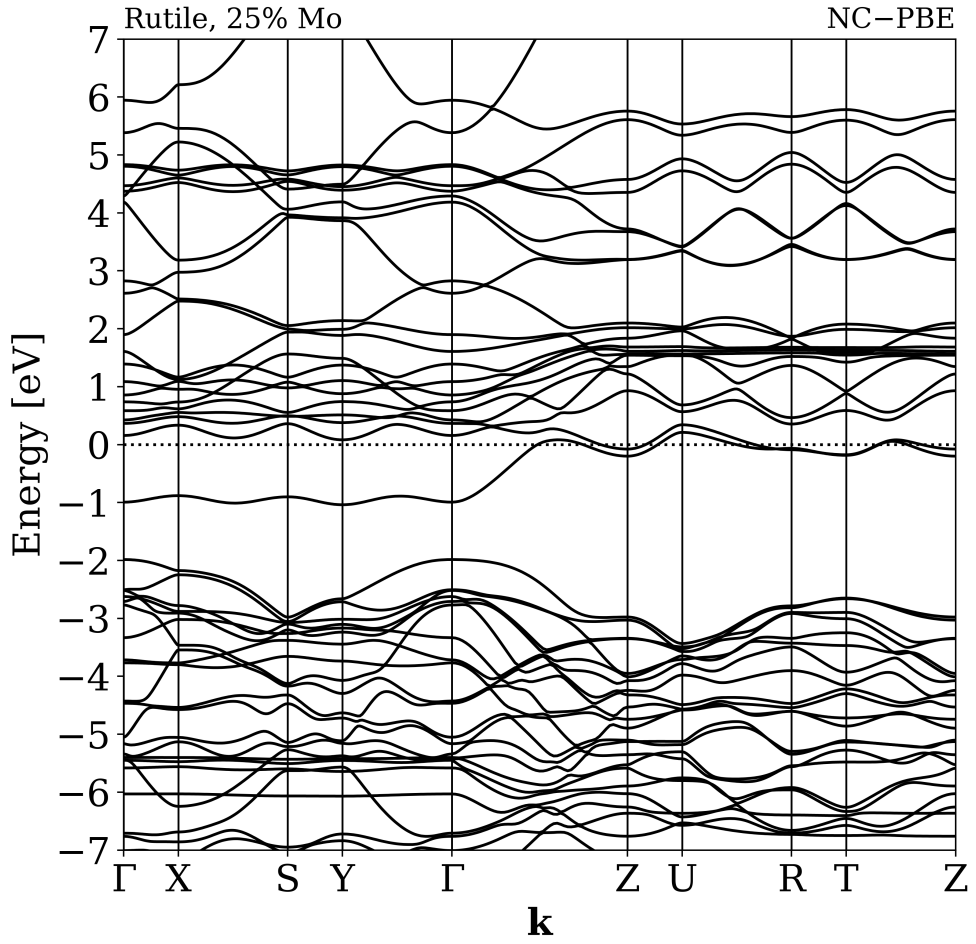

(b)

Figure 4.27: The (a) DOS and the (b) band structure of rutile doped with 25% Mo, computed with the NC pseudopotential and the PBE functional, with the Fermi energy set to $E = 0$ eV.

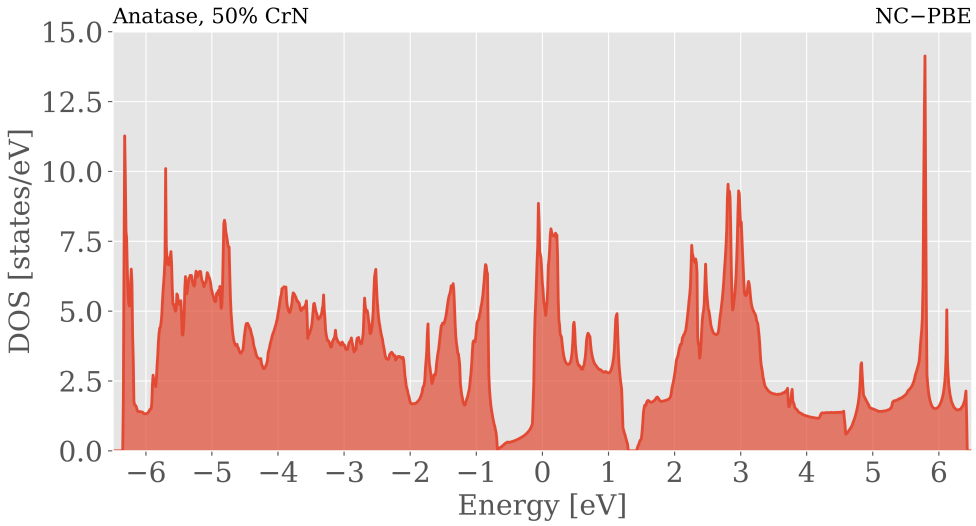

(a)

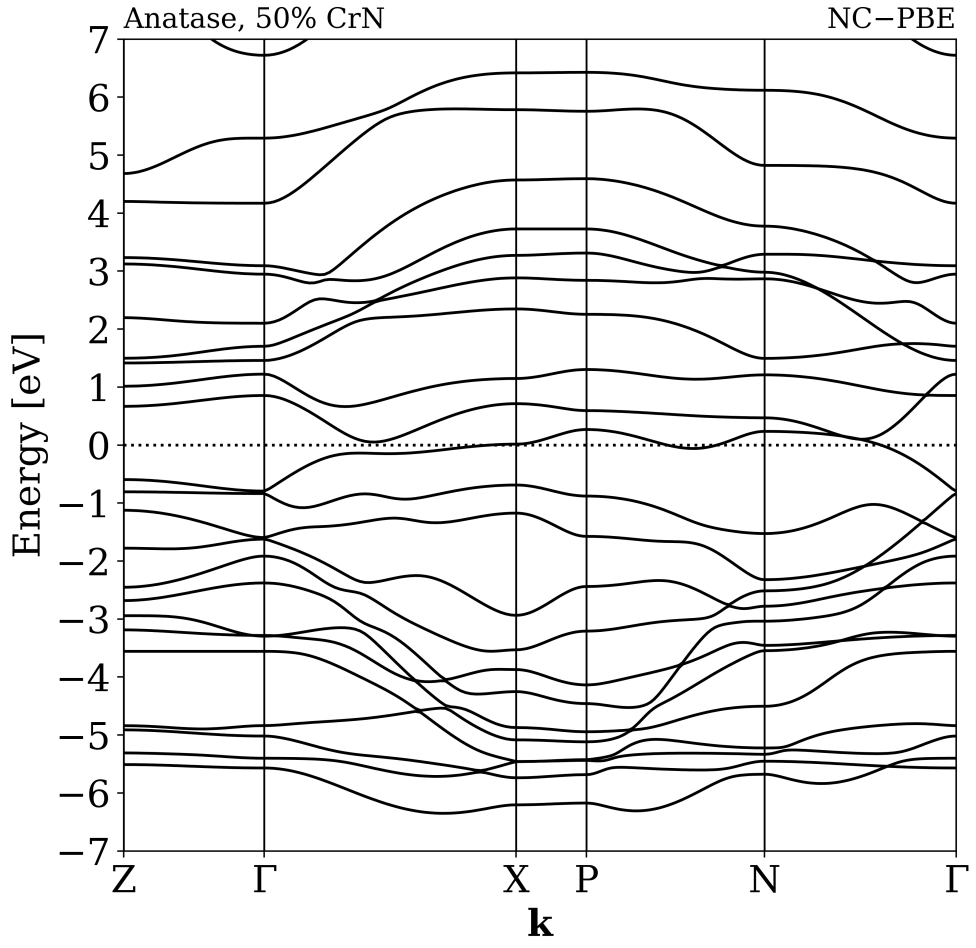

(b)

Figure 4.28: The (a) DOS and the (b) band structure of anatase doped with 50% CrN, computed with the NC pseudopotential and the PBE functional, with the Fermi energy set to $E = 0$ eV.

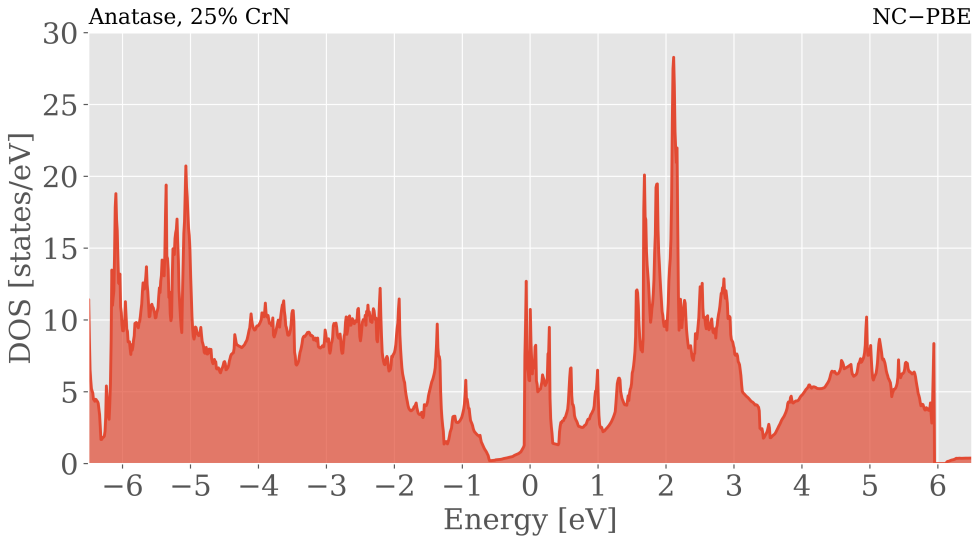

(a)

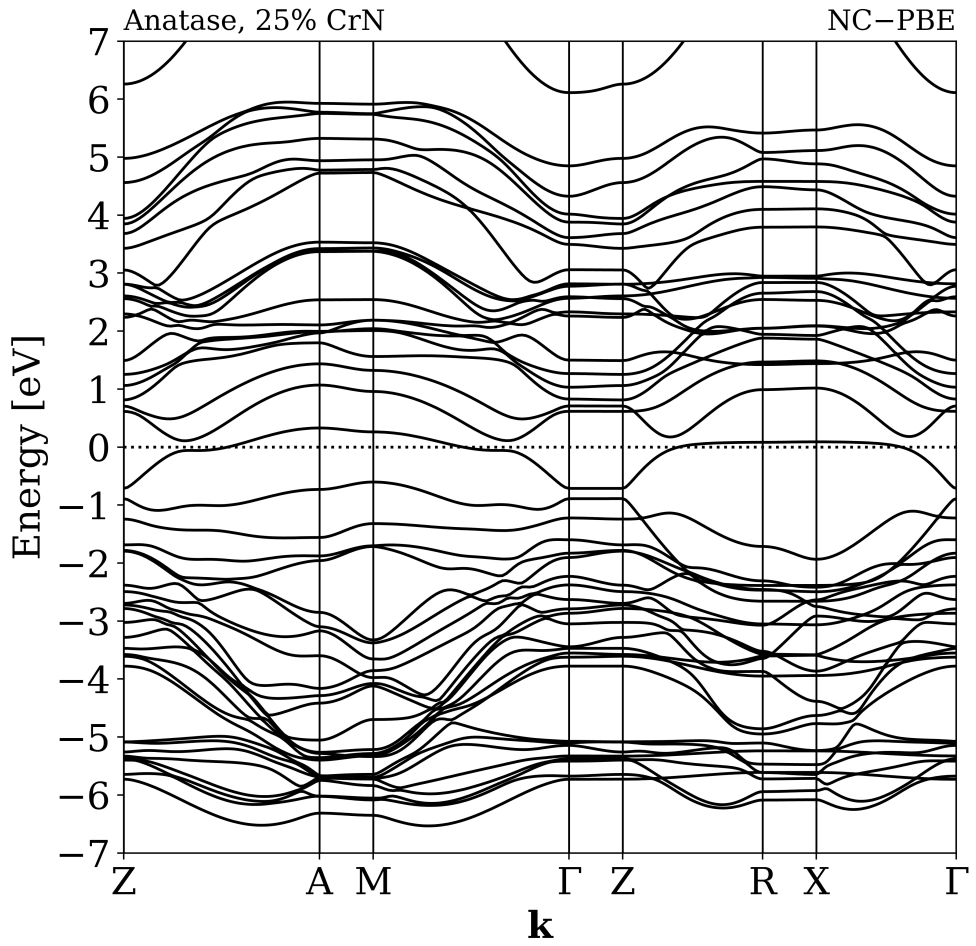

(b)

Figure 4.29: The (a) DOS and the (b) band structure of anatase doped with 25% CrN, computed with the NC pseudopotential and the PBE functional, with the Fermi energy set to $E = 0$ eV.

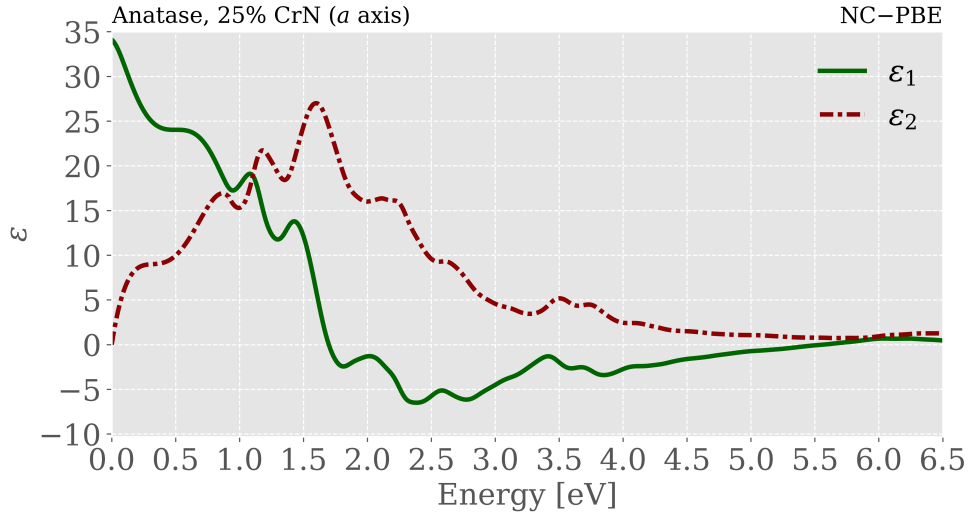

(a)

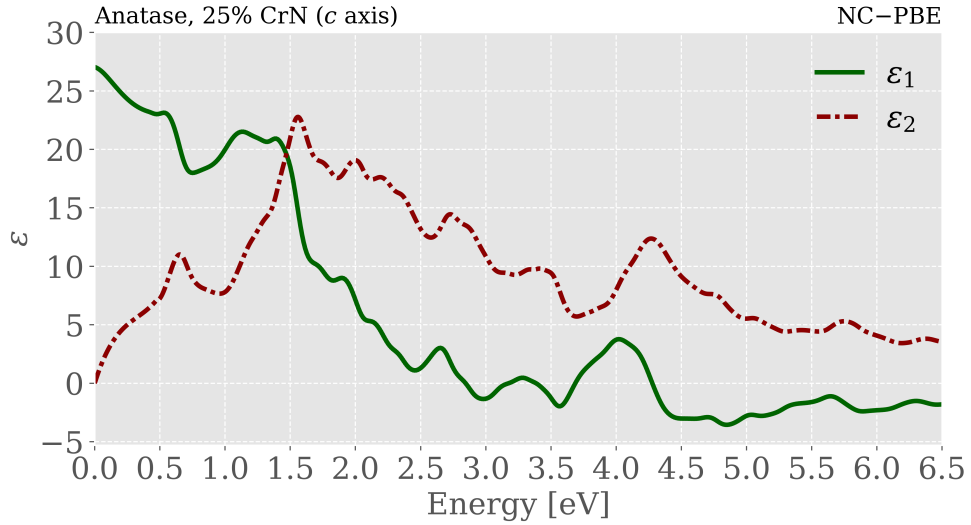

(b)

Figure 4.30: Dielectric function of anatase doped with 25% CrN, along the (a) ordinary and the (b) extraordinary axes. The spectra are computed with the NC pseudopotential and the PBE functional.

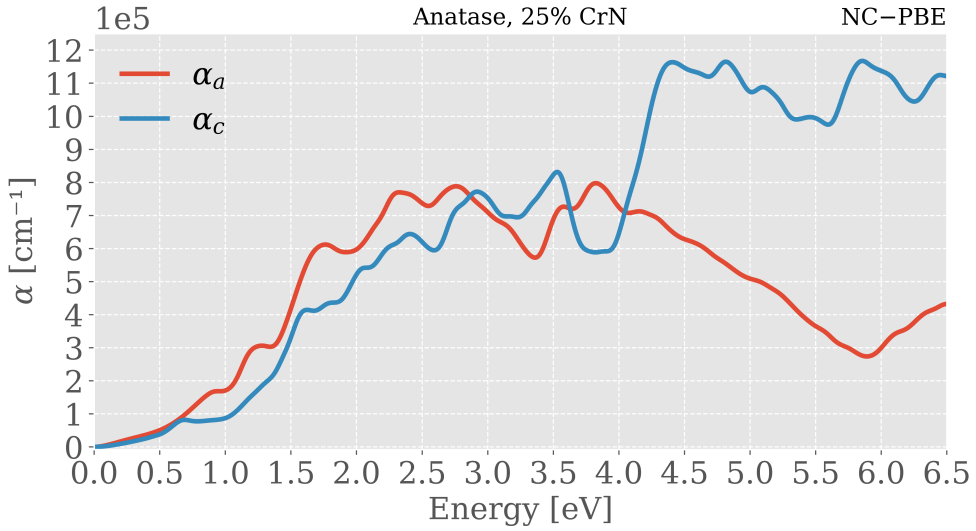

(a)

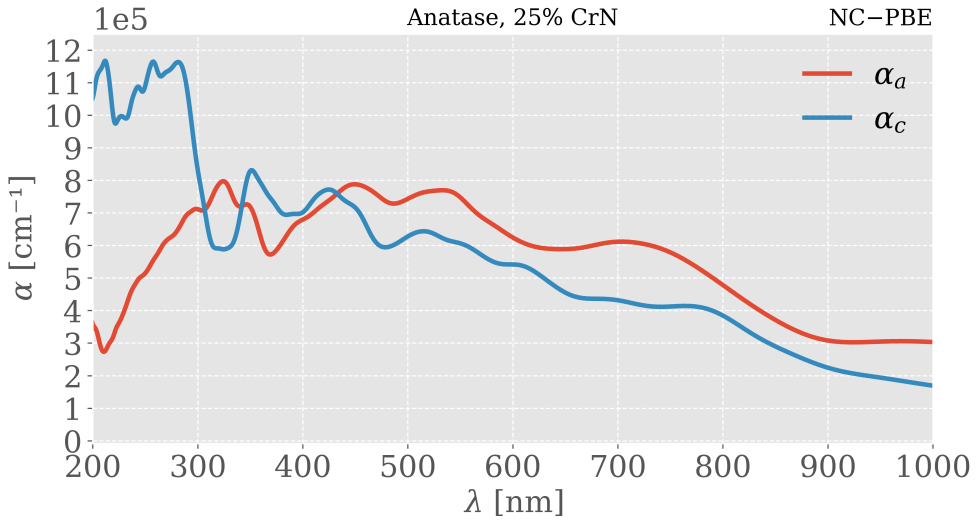

(b)

Figure 4.31: Absorption coefficient of anatase doped with 25% CrN, as a function of (a) photon energy and (b) photon wavelength. The spectra are computed with the NC pseudopotential and the PBE functional.

4.6.7 Anatase, Oxygen Vacancy

As illustrated in Fig. 4.32a, the 3.1% oxygen vacancy in anatase appears to induce a shift in the Fermi energy across the conduction band edge. The band gap below E_F is of approximately the same size as that of pure anatase, but the placement of E_F results in metallic properties. Besides this, the structures of the DOS are almost identical to those of pure anatase. The somewhat rougher curve of the plot may be due to a reduced number of *k*-points, necessitated by the high computational cost of utilizing such a large unit cell. The band structure of Fig. 4.32b corroborates the findings from Fig. 4.32a. The high band density can be attributed to the size of the unit cell, as discussed in Sect. 4.6.3.

Previous studies have reported an n-type behavior of TiO_2, caused by the two free electrons generated by each O vacancy [1, p. 19]. While our results do not strictly demonstrate an n-type character, a 3.1% defect concentration is relatively high [76]. Moreover, oxygen vacancies typically appear on the surface of TiO_2 [77], and not uniformly distributed as in our calculations.

Improving our understanding of such defects in TiO_2 could involve conducting DFT calculations on the surface effects of O vacancies rather than the bulk, and exploring lower concentrations to better represent naturally occurring defects. Along with oxygen vacancies, other point defects such as Ti vacancies and Ti interstitials, which are common in TiO_2 [1, p. 19], could also be interesting avenues for research.

4.6.8 Further Improvements

Although we have identified intermediate band formation in both 25% and 12.5% CrN-doped rutile, our conventional GGA-based calculations have their limitations. This is demonstrated by the method's significant band gap underestimation of rutile, causing reason to believe a reduced reliability of similar structures. The use of a hybrid functional, such as HSE06, may increase the accuracy, as this has proven to provide a more accurate electronic description of TiO_2 [78]. Nevertheless, our results provide an interesting avenue of further research into the prospects of doped TiO_2 as an intermediate band material.

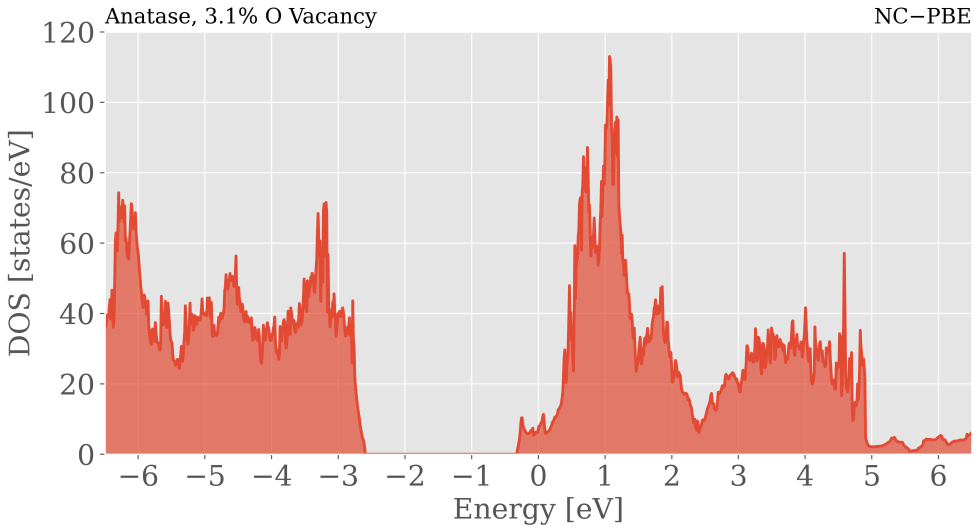

(a)

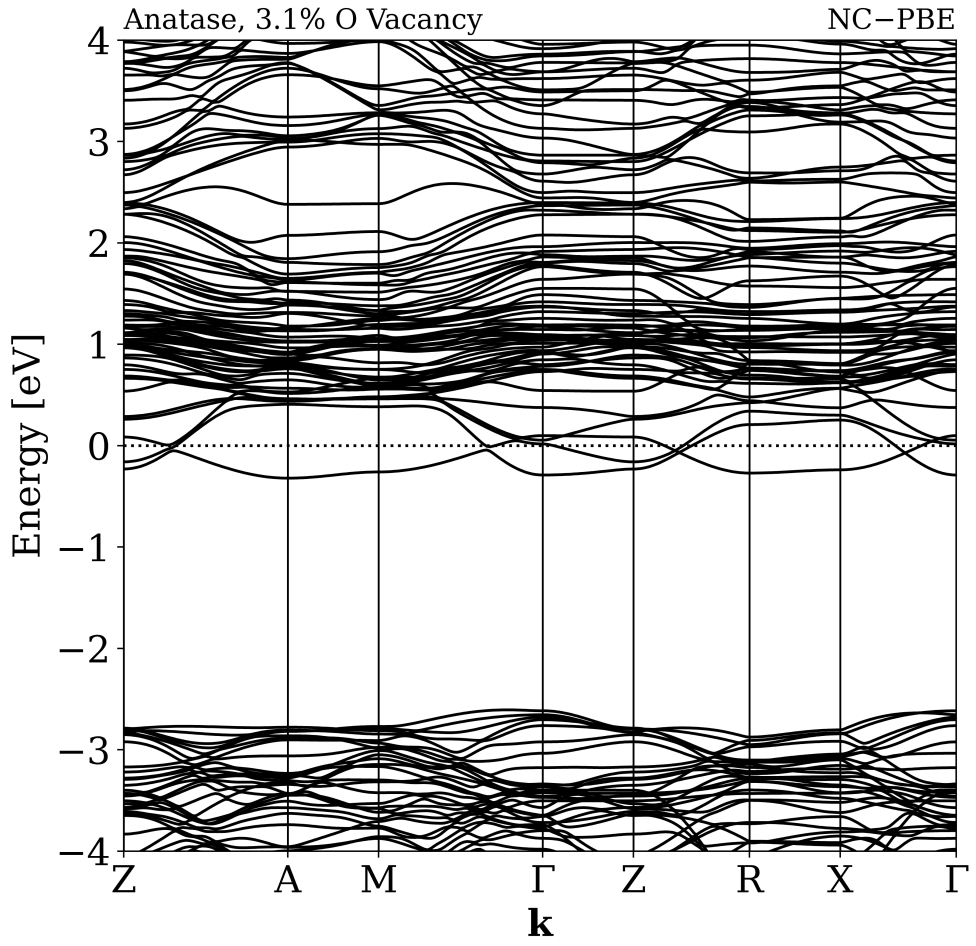

(b)

Figure 4.32: The (a) DOS and the (b) band structure of anatase with 3.1% oxygen vacancies, computed with the NC pseudopotential and the PBE functional, with the Fermi energy set to $E = 0$ eV.

Chapter 5

Conclusion

Various methods have been employed to investigate the electronic and optical properties of rutile and anatase, including standard GGA–DFT calculations, an amended version of the PHS method for optimized optical data, and DFT+U. Furthermore, the critical points of the two polymorphs were analyzed using both second derivative analysis and vertical translation analysis. Finally, GGA–DFT computations were performed on doped structures of TiO_2, in addition to an O vacancy structure, to investigate the effects on electronic and optical properties and evaluate their potential use in intermediate band solar cells.

The electronic properties of TiO_2 polymorphs were analyzed in depth, showing rutile and anatase as semiconductors. Rutile demonstrated a direct band gap, indicating its potential as a superior conductor, while anatase showcased an indirect band gap. However, anatase may have higher conductivity due to oxygen vacancies. Despite moderately successful predictions, the underestimation of the band gap by conventional DFT methods signifies the need for further refinement in these techniques. The use of more advanced calculations, such as utilizing the hybrid HSE06 functional, is suggested for improved prediction precision.

In parallel, the optical properties of rutile and anatase were studied using the PHS method, simplified by using experimental band gaps as energy axis adjustment, instead of the HSE06 functional, due to technical limitations. The results revealed their anisotropic nature and limited absorption of visible light. While the method generally agreed with existing literature, some discrepancies were noted, emphasizing the need for methodological improvement. Specifically, efforts should be made to reduce the empirical nature of our approach and increase its applicability to unknown systems, such as doped TiO_2.

Critical points in the dielectric function of rutile and anatase were examined, unveiling a larger number of CPs than previously reported. The

CPs from the second derivative analysis were compared to interband transitions found by vertical translation analysis, identifying potential optical transitions primarily responsible for a little over half of the CPs. However, unidentified CPs and limitations of these techniques, especially the exclusion of optical transition probabilities in the vertical translation analysis, introduce substantial uncertainties into the findings. Therefore, these results should be interpreted with due caution and further studies are needed to improve the precision and reliability of these methodologies.

The electronic structure of TiO_2 was also studied using DFT+U, which by adjusting the Hubbard U parameter, better replicated the band gaps of rutile and anatase. However, DFT+U showed some limitations, such as splitting of bands at symmetry points and a shift in rutile's band gap from direct to indirect, contradicting prior research. The semi-empirical nature of DFT+U introduces uncertainties when structural or elemental modifications are undertaken. Additionally, we encountered a technical error that obstructed optical calculations utilizing this method. Due to these considerations, we ultimately decided against employing DFT+U for the examination of the doped TiO_2 structures in this study.

Lastly, the study of different configurations of TiO_2 yielded promising results, particularly with the doping of rutile with CrN. Both a configuration of rutile doped with 25% and with 12.5% CrN formed an intermediate band between the valence and conduction bands, potentiating their use in intermediate band solar cells. The other doping configurations resulted in metallic properties, making the materials unsuitable for IBSCs. A point defect anatase structure, with a 3.1% oxygen vacancy, also resulted in metallic properties by shifting the Fermi energy above the conduction band edge.

The discussed constraints of GGA-based calculations introduce a degree of uncertainty in our results for doped TiO_2. Using an HSE06 functional, however, could potentially yield more accurate property predictions. Regardless, the formation of intermediate bands opens up an intriguing path for further studies, reinforcing the potential of CrN doped TiO_2 as a viable candidate for an intermediate band material.

Bibliography

[1] F. Parrino and L. Palmisano, *Titanium Dioxide (TiO2) and Its Applications*, 1st ed. Elsevier Inc., 2020.

[2] S. Pan, X. Lui, M. Guo, S. F. Yu, H. Huang, H. Fan, and G. Li, "Engineering the intermediate band states in amorphous ti3+-doped tio2 for hybrid dye-sensitized solar cell applications," *Journal of Materials Chemistry A*, pp. 11 437–11 443, 3 2015.

[3] Z. Tong, T. Peng, W. Sun, W. Liu, S. Guo, and X. Zhao, "Introducing an intermediate band into dye-sensitized solar cells by w6+ doping into tio2 nanocrystalline photoanodes," *The Journal of Physical Chemistry C*, vol. 118, pp. 16 892–16 895, 30 2014.

[4] A. Dashora, N. Patel, D. C. Kothari, B. L. Ahuja, and A. Miotello, "Formation of an intermediate band in the energy gap of tio2 by cu–n-codoping: First principles study and experimental evidence," *Solar Energy Materials and Solar Cells*, vol. 125, pp. 120–126, 2014.

[5] F. Wu, H. Lan, Z. Zhang, and P. Cui, "Quantum efficiency of intermediate-band solar cells based on non-compensated n-p codoped TiO2," *The Journal of Chemical Physics*, vol. 137, no. 10, p. 104 702, 2012.

[6] J. Barnhart, "Occurrences, uses, and properties of chromium," *Regulatory Toxicology and Pharmacology*, vol. 26, no. 1, S3–S7, 1997.

[7] J. Tallkvist and A. Oskarsson, "Molybdenum," in *Handbook on the Toxicology of Metals (Fourth Edition)*, G. F. Nordberg, B. A. Fowler, and M. Nordberg, Eds., Fourth Edition, Academic Press, 2015, pp. 1077–1089.

[8] M. Nishiwaki and H. Fujiwara, "Highly accurate prediction of material optical properties based on density functional theory," *Computational Materials Science*, vol. 172, p. 109 315, 2020.

[9] M. Cardona and P. Y. Yu, *Fundamentals of Semiconductors*, 4th ed. Springer, 2010.

[10] L. P. Xu *et al.*, "Interband electronic transitions and phase transformation of multiferroic Bi1xLaxFe1yTiyO3 ceramics revealed by temperature-dependent spectroscopic ellipsometry," *Journal of Applied Physics*, vol. 114, no. 23, p. 233 509, 2013.

[11] R. O. Jones, "Density functional theory: Its origins, rise to prominence, and future," *Reviews of Modern Physics*, vol. 87, no. 3, pp. 897–923, 2015.

[12] D. S. Sholl and J. A. Steckel, *Density Functional Theory - A Practical Introduction*. John Wiley & Sons, Inc., 2009.

[13] M. Born and R. Oppenheimer, "Zur quantentheorie der molekeln," *Annalen der Physik*, vol. 389, no. 20, pp. 457–484, 1927.

[14] D. J. Griffiths and D. F. Schroeter, *Introduction to Quantum Mechanics*, 3rd ed. Cambridge University Press, 2018.

[15] W. Pauli, "Über den zusammenhang des abschlusses der elektronengruppen im atom mit der komplexstruktur der spektren," *Zeitschrift für Physik*, vol. 31, pp. 765–783, 1925.

[16] P. Hohenberg and W. Kohn, "Inhomogeneous electron gas," *Physical Review*, vol. 136, no. 3B, B864–B871, 1964.

[17] W. Kohn and L. J. Sham, "Self-consistent equations including exchange and correlation effects," *Physical Review*, vol. 140, no. 4A, A1133–A1138, 1965.

[18] J. P. Perdew, K. Burke, and M. Ernzerhof, "Generalized gradient approximation made simple," *Physical Review Letters*, vol. 77, no. 18, pp. 3865–3868, 1996.

[19] J. P. Perdew, A. Ruzsinszky, G. I. Csonka, O. A. Vydrov, G. E. Scuseria, L. A. Constantin, X. Zhou, and K. Burke, "Restoring the density-gradient expansion for exchange in solids and surfaces," *Physical Review Letters*, vol. 100, no. 13, 2008.

[20] G. Zhang, A. M. Reilly, A. Tkatchenko, and M. Scheffler, "Performance of various density-functional approximations for cohesive properties of 64 bulk solids," *New Journal of Physics*, vol. 20, no. 6, 2018.

[21] M.-Y. Zhang, Z.-H. Cui, Y.-C. Wang, and H. Jiang, "Hybrid functionals with system-dependent parameters: Conceptual foundations and methodological developments," *WIREs Computational Molecular Science*, vol. 10, no. 6, 2020.

[22] J. Heyd, G. E. Scuseria, and M. Ernzerhof, "Hybrid functionals based on a screened coulomb potential," *The Journal of Chemical Physics*, vol. 118, no. 18, pp. 8207–8215, 2003.

[23] J. Heyd, G. E. Scuseria, and M. Ernzerhof, "Erratum: "hybrid functionals based on a screened coulomb potential" [j. chem. phys. 118, 8207 (2003)]," *The Journal of Chemical Physics*, vol. 124, no. 21, 2006.

[24] C. Kittel, *Introduction to Solid State Physics*, 8th ed. John Wiley & Sons, Inc., 2018, Global ed.

[25] K. Momma and F. Izumi, "Vesta3 for three-dimensional visualization of crystal, volumetric and morphology data," *Journal of Applied Crystallography*, vol. 44, pp. 1272–1276, 2011.

[26] A. Suresh and N. Soundararajan, "The conventional cell and the primitive cell electronic structure of anatase titanium dioxide crystal," *Materials Research Express*, vol. 4, no. 3, 2017.

[27] H. J. Monkhorst and P. J. D., "Special points for brillouin-zone integrations," *Physical Review B*, vol. 13, no. 12, pp. 5188–5192, 1976.

[28] S. A. Tolba, K. M. Gameel, B. A. Ali, H. A. Almossalami, and N. K. Allam, "The dft+u: Approaches, accuracy, and applications," in *Density Functional Calculations*, IntechOpen, 2018.

[29] S. Ryee and M. J. Han, "The effect of double counting, spin density, and hund interaction in the different dft+u functionals," *Scientific Reports*, vol. 8, no. 9559, 2018.

[30] J. Singh, *Electronic and Optoelectronic Properties of Semiconductor Structures*. Cambridge University Press, 2003.

[31] B. G. Streetman and S. K. Banerjee, *Solid State Electronic Devices*, 7th ed. Pearson Education, Inc., 2015.

[32] S. Botti, F. Sottile, N. Vast, V. Olevano, L. Reining, H.-C. Weissker, A. Rubio, G. Onida, R. Del Sole, and R. W. Godby, "Long-range contribution to the exchange-correlation kernel of time-dependent density functional theory," *Physical Review B*, vol. 69, p. 155 112, 15 2004.

[33] J. Paier, M. Marsman, and G. Kresse, "Dielectric properties and excitons for extended systems from hybrid functionals," *Physical Review B*, vol. 78, p. 121 201, 12 2008.

[34] H. Fujiwara, M. Kato, M. Tamakoshi, T. Miyadera, and M. Chikamatsu, "Optical characteristics and operational principles of hybrid perovskite solar cells," *physica status solidi (a)*, vol. 215, no. 12, p. 1 700 730, 2018.

[35] P. Borlido, J. Schmidt, A. W. Huran, F. Tran, M. A. L. Marques, and S. Botti, "Exchange-correlation functionals for band gaps of solids: Benchmark, reparametrization and machine learning," *npj Computational Materials*, vol. 6, no. 96, 2020.

[36] M. P. Marder, *Condensed Matter Physics*. John Wiley & Sons, Inc., 2010.

[37] W. Shockley and H. J. Queisser, "Detailed balance limit of efficiency of p-n junction solar cells," *Journal of Applied Physics*, vol. 32, no. 3, pp. 510–519, 1961.

[38] G. L. Araújo and A. Martí, "Absolute limiting efficiencies for photovoltaic energy conversion," *Solar Energy Materials and Solar Cells*, vol. 33, no. 2, pp. 213–240, 1994.

[39] A. Luque and A. Martí, "Ultra-high efficiency solar cells: The path for mass penetration of solar electricity," *Electronics Letters*, vol. 44, pp. 943–945, 2008.

[40] A. Luque and A. Martí, *Next Generation Photovoltaics: High Efficiency through Full Spectrum Utilization*, 1st ed. CRC Press, 2003, ch. Nonconventional photovoltaic technology: A need to reach goals.

[41] M. A. Green, "Third generation photovoltaics: Ultra-high conversion efficiency at low cost," *Progress in Photovoltaics: Research and Applications*, vol. 9, no. 2, pp. 123–135, 2001.

[42] N. S. Lewis, G. Crabtree, A. J. Nozik, *et al.*, "Basic research needs for solar energy utilization. report of the basic energy sciences workshop on solar energy utilization," Apr. 2005.

[43] A. Luque and A. Martí, "Increasing the efficiency of ideal solar cells by photon induced transitions at intermediate levels," *Physical Review Letters*, vol. 78, pp. 5014–5017, 1997.

[44] E. Antolin, A. Martí, and A. Luque, "Intermediate band solar cells," in *Intermediate Band Solar Cells*, Elsevier Inc., 2012.

[45] M. Y. Levy and C. Honsberg, "Solar cell with an intermediate band of finite width," *Physical Review B*, vol. 78, p. 165 122, 16 2008.

[46] P. Giannozzi *et al.*, "Quantum espresso: A modular and open-source software project for quantum simulations of materials," *Journal of Physics: Condensed Matter*, vol. 21, no. 39, 2009.

[47] M. Själander, M. Jahre, G. Tufte, and N. Reissmann, "EPIC: An energy-efficient, high-performance GPGPU computing research infrastructure," 2019. arXiv: 1912.05848 [cs.DC].

[48] A. Kokalj, "Xcrysden—a new program for displaying crystalline structures and electron densities," *Journal of Molecular Graphics and Modelling*, vol. 17, no. 3–4, pp. 176–179, 1999.

[49] P. E. Blöchl, O. Jepsen, and O. K. Andersen, "Improved tetrahedron method for brillouin-zone integrations," *Physical Review B*, vol. 49, pp. 16 223–16 233, 23 1994.

[50] J. P. Perdew and A. Zunger, "Self-interaction correction to density-functional approximations for many-electron systems," *Physical Review B*, vol. 23, pp. 5048–5079, 10 1981.

[51] D. O. Scanlon, C. W. Dunnill, J. Buckeridge, *et al.*, "Band alignment of rutile and anatase tio2," *Nature Materials*, vol. 12, pp. 798–801, 2013.

[52] G. Strang, *Calculus*. Wellesley-Cambridge Press, 1991.

[53] A. Savitzky and M. J. E. Golay, "Smoothing and differentiation of data by simplified least squares procedures," *Analytical Chemistry*, vol. 36, pp. 1627–1639, 8 1964.

[54] F. Labat, P. Baranek, C. Domain, C. Minot, and C. Adamo, "Density functional theory analysis of the structural and electronic properties of tio2 rutile and anatase polytypes: Performances of different exchange-correlation functionals," *The Journal of Chemical Physics*, vol. 126, no. 15, p. 154 703, 2007.

[55] S.-D. Mo and W. Y. Ching, "Electronic and optical properties of three phases of titanium dioxide: Rutile, anatase, and brookite," *Physical Review B*, vol. 51, pp. 13 023–13 032, 19 1995.

[56] C. Di Valentin, G. Pacchioni, and A. Selloni, "Reduced and n-type doped tio2: Nature of ti3+ species," *The Journal of Physical Chemistry C*, vol. 113, pp. 20 543–20 552, 48 2009.

[57] T. Luttrell, S. Halpegamage, J. Tao, A. Kramer, E. Sutter, and M. Batzill, "Why is anatase a better photocatalyst than rutile? - model studies on epitaxial tio2 films," *Scientific Reports*, vol. 4, no. 4043, 2014.

[58] L. Thulin and J. Guerra, "Calculations of strain-modified anatase tio2 band structures," *Physical Review B*, vol. 77, p. 195 112, 19 2008.

[59] F. Bai, W. Li, and Z. H., "Theoretical studies of titanium dioxide for dye-sensitized solar cell and photocatalytic reaction," in *Titanium Dioxide*, IntechOpen, 2017.

[60] M. Calatayud, P. Mori-Sánchez, A. Beltrán, A. Martın Pendás, E. Francisco, J. Andrés, and J. M. Recio, "Quantum-mechanical analysis of the equation of state of anatase tio2," *Physical Review B*, vol. 64, p. 184 113, 18 2001.

[61] M. H. Samat, A. M. M. Ali, M. F. M. Taib, O. H. Hassan, and M. Z. A. Yahya, "Structural and electronic properties of tio2 polymorphs with effective on-site coulomb repulsion term: Dft+u approaches," *Materials Today: Proceedings*, vol. 17, pp. 472–483, 2019.

[62] P. Mazzolini, P. Gondoni, V. Russo, D. Chrastina, C. S. Casari, and A. Li Bassi, "Tuning of electrical and optical properties of highly conducting and transparent ta-doped tio2 polycrystalline films," *The Journal of Physical Chemistry*, vol. 119, pp. 6988–6997, 2015.

[63] D. M. Gates, "Spectral distribution of solar radiation at the earth's surface," *Science*, vol. 151, no. 3710, pp. 523–529, 1966.

[64] T. Tiwald and M. Schubert, "Measurement of rutile tio2 dielectric tensor from 0.148 to 33 um using generalized ellipsometry," *Proceedings of SPIE - The International Society for Optical Engineering*, vol. 4103, pp. 19–29, 2000.

[65] J. Jellison G. E., L. A. Boatner, J. D. Budai, B.-S. Jeong, and D. P. Norton, "Spectroscopic ellipsometry of thin film and bulk anatase (TiO2)," *Journal of Applied Physics*, vol. 93, no. 12, pp. 9537–9541, 2003.

[66] D. Reyes-Coronado *et al.*, "Phase-pure tio2 nanoparticles: Anatase, brookite and rutile," *Nanotechnology*, vol. 19, no. 14, 2008.

[67] A. Soussi, A. Ait Hssi, M. Boujnah, K. Abouabassi, A. Asbayou, L. Boulkaddat, M. Rachid, E. Abdeslam, A. Ihlal, and K. Bouabid, "Electronic and optical properties of tio2 thin films: Combined experimental and theoretical study," *Journal of Electronic Materials*, 2021.

[68] K. M. Glassford and J. R. Chelikowsky, "Optical properties of titanium dioxide in the rutile structure," *Physical Review B*, vol. 45, no. 7, 1992.

[69] F. Hedhili *et al.*, "Structural, electronic and optical dft investigation of ruthenium doped anatase tio2 for photocatalytic applications," *Physica Scripta*, vol. 97, no. 6, p. 065 818, 2022.

[70] M. Cardona and G. Harbeke, "Optical properties and band structure of wurtzite-type crystals and rutile," *Physical Review*, vol. 137, no. 5A, A1467–A1476, 1965.

[71] N. Hosaka, T. Sekiya, C. Satoko, and S. Kurita, "Optical properties of single-crystal anatase tio2," *Journal of the Physical Society of Japan*, vol. 66, no. 3, pp. 877–880, 1997.

[72] S. Zollner, M. Garriga, J. Kircher, J. Humlicek, M. Cardona, and G. Neuhold, "Temperature dependence of the dielectric function and the interband critical-point parameters of gap," *Physical Review B*, vol. 48, pp. 7915–7929, 11 1993.

[73] L. Piela, *Ideas of Quantum Chemistry*. Elsevier, 2007.

[74] A. Benassi, A. Ferretti, and C. Cavazzoni, "Pwscf's epsilon.x user's manual,"

[75] R. H. Petrucci, F. G. Herring, J. D. Madura, and C. Bissonnette, *General Chemistry: Principles and Modern Applications*, 11th ed. Pearson Canada Inc., 2017.

[76] E. Yagi and R. R. Hasiguti, "Electronic conduction above 4 k of slightly reduced oxygen-deficient rutile," *Physical Review B*, vol. 54, pp. 7945–7956, 11 1996.

[77] M. V. Ganduglia-Pirovano, A. Hofmann, and J. Sauer, "Oxygen vacancies in transition metal and rare earth oxides: Current state of understanding and remaining challenges," *Surface Science Reports*, vol. 62, no. 6, pp. 219–270, 2007.

[78] G. Pacchioni, "Modeling doped and defective oxides in catalysis with density functional theory methods: Room for improvements," *The Journal of Chemical Physics*, vol. 128, 18 2008.

Appendix

Code listing 1: Core Python functions for vertical translation analysis

```
def main(polymorph):
    filename, fermi, kinterval, dEt = getInputData(polymorph)

    # Get valence and conduction bands from file
    vbands, cbands = readBands(filename, fermi)

    # Find critical points based on parallel bands
    critPoints = calcCritPoints(vbands, cbands, kinterval, dEt)

    # Compare to CPs from second derivative analysis,
    # and plot corresponding CPs as interband transitions.

# Read band stucture from file
def readBands(filename, fermi):
    with open(filename, 'r') as f:
        lines = f.readlines()

    bands = [] # List of all bands
    band  = [ [], [] ] # [ [k values], [E values] ]
    for line in lines:
        # An empty line separates bands in the file
        if line.isspace():
            bands.append(band)
            band = [ [], [] ]
        else:
            k, E = map(float, line.split())
            band[0].append(k)
            band[1].append(E - fermi)   # Adjust E axis by Fermi energy

    # Add last band (usually no whitespace after last one)
    bands.append(band) if any(band) else None

    # Separate bands into valence bands and conduction bands
    vbands = [band for band in bands if band[1][0] < 0]
    cbands = [band for band in bands if band[1][0] > 0]

    return vbands, cbands

def calcCritPoints(vbands, cbands, kinterval, dEt):
    critPoints = []  # [ [k-pos, vb energy, cb energy, dE, weight], ... ]
    for vb in vbands:
        for cb in cbands:
            i = 0
```

```
            # While i + 1 is not out of scope of the k-axis
            while i + 1 < len(vb[0]):
                dk, j = 0, i + 1
                groupEt = [ cb[1][i] - vb[1][i] ] # Current group's list of Et=Ec-Ev

                # Exits loop if Et is not within +/- dEt of all of the group's Et
                while sameEt(vb, cb, j, dEt, groupEt):
                    dk += vb[0][j] - vb[0][j-1]

                    # Critical point registered if all Et are +/- dEt
                    # of each other for a length of kinterval
                    if dk >= kinterval:
                        critPoints = insertCritPoint(critPoints, vb, cb, i, j, dEt)

                        # Increase i so next iteration doesn't recount the same points
                        # (important for correct weighting,
                        #  since not all k[i+1]-k[i] are equal)
                        i += j-2
                        break

                    j += 1

                i += 1

    return critPoints

def sameEt(vb, cb, j, dEt, groupEt):
    # Check if j out of scope
    if j >= len(vb[0]):
        return False

    for Et in groupEt:
        # if group's Et=Ec-Ev is not within dEt of the new Et
        if abs(Et - cb[1][j] + vb[1][j]) > dEt:
            return False
    return True

# Checks whether critical point is already in critPoints and edits accordingly
def insertCritPoint(critPoints, vb, cb, i, j, dEt):
    cp = getCritPointEntry(vb, cb, i, j)

    duplicate = False

    for n in range(len(critPoints)):
        if isDuplicate(cp, critPoints, n, dEt):
            # If duplicate, redefine critPoints values to become the new
            # average of all the duplicates, and increase the weight

            critPoints[n][0] = (1/(critPoints[n][-1]+1)) * \
                               (critPoints[n][0]*critPoints[n][-1] + cp[0]) # k-pos.
            critPoints[n][1] = (1/(critPoints[n][-1]+1)) * \
                               (critPoints[n][1]*critPoints[n][-1] + cp[1]) # Ev
            critPoints[n][2] = (1/(critPoints[n][-1]+1)) * \
                               (critPoints[n][2]*critPoints[n][-1] + cp[2]) # Ec
            critPoints[n][3] = (1/(critPoints[n][-1]+1)) * \
                               (critPoints[n][3]*critPoints[n][-1] + cp[3]) # Et
            critPoints[n][-1] += 1 # Weight

            duplicate = True
            break
```

```
    # If not duplicate, add critical point as its own entry
    if not duplicate:
        critPoints.append(cp)

    return critPoints

# Returns critical point entry, where each data point is the
# average value between (and including) indexes i and j.
def getCritPointEntry(vb, cb, i, j):
    length = j + 1 - i
    cp = [
        sum(vb[0][n] for n in range(i, j+1)) / length,     # k-pos. average
        sum(vb[1][n] for n in range(i, j+1)) / length,     # VB energy average
        sum(cb[1][n] for n in range(i, j+1)) / length,     # CB energy average
        sum(cb[1][n] - vb[1][n] for n in range(i, j+1)) / length,  # Et average
        1  # Weight
    ]

    return cp

# Checks if duplicate critical point
def isDuplicate(cp, critPoints, n, dEt):
    k  = abs(cp[0] - critPoints[n][0]) <= 0.2 # k-pos. difference
    Ev = abs(cp[1] - critPoints[n][1]) <= 0.1 # Ev difference
    Ec = abs(cp[2] - critPoints[n][2]) <= 0.1 # Ec difference
    Et = abs(cp[3] - critPoints[n][3]) <= dEt # Et difference

    return k and Ev and Ec and Et
```

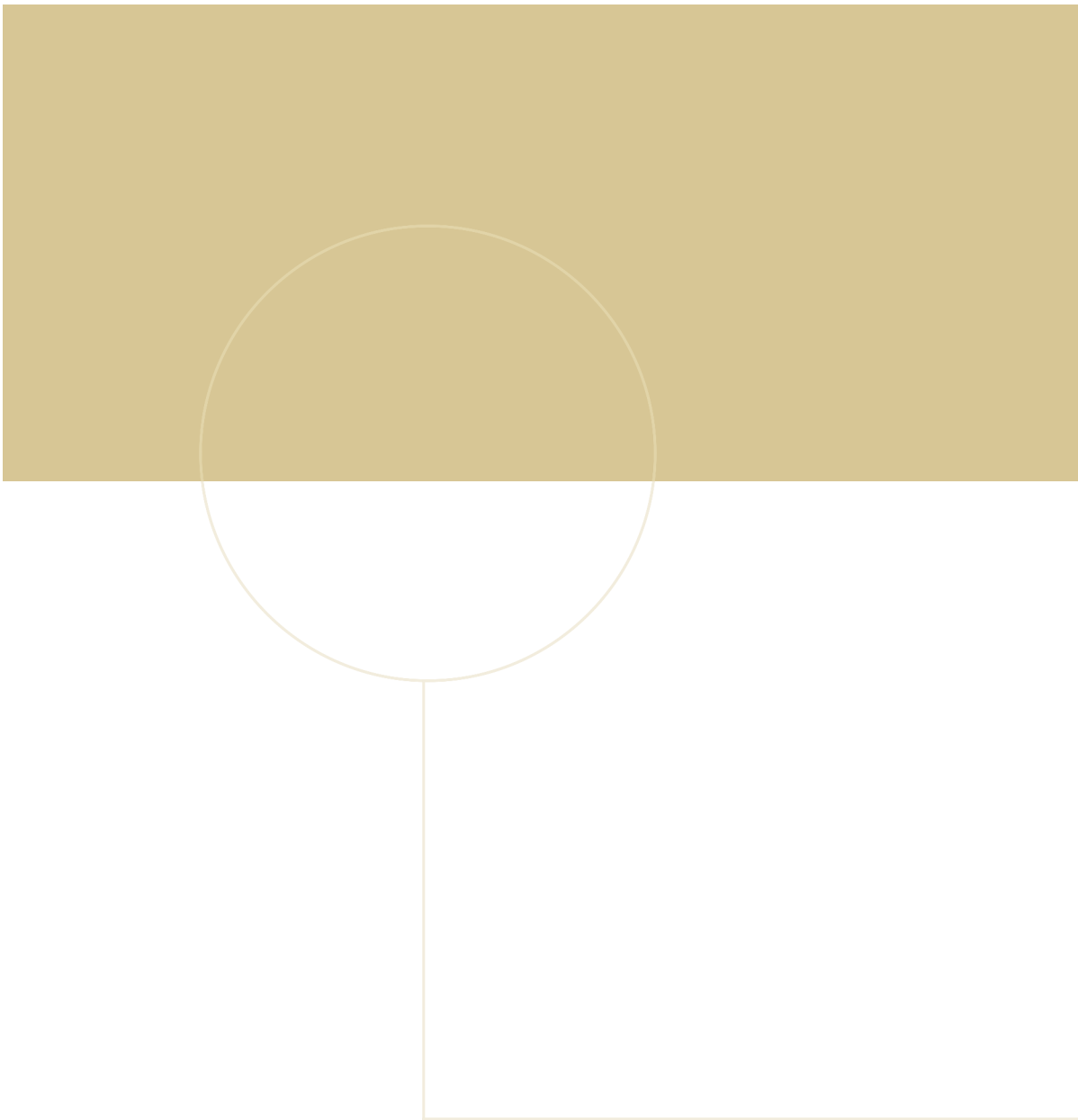

NTNU

Norwegian University of
Science and Technology